

Optical, Electrical and Thermal Responses of Near-Field Thermophotovoltaic Cells for Thermal Energy Conversion

Japheth Lau Zi Jun

Faculty of Engineering, Computing and Science
Swinburne University of Technology Sarawak Campus
Kuching, Sarawak, Malaysia

Submitted for the degree of Doctor of Philosophy

2018

Acknowledgement

I would first like to thank God for allowing all this to happen and for his providence throughout my time as a PhD student during which I have learned a lot. I would also like to thank my coordinating supervisor, Associate Professor Basil T. Wong for his invaluable guidance throughout my studies from the planning phase all the way to the completion of this thesis. Completing this PhD project would be near impossible without his advice, suggestions and patience. I would like to extend my gratitude to Professor Baohua Jia for agreeing to be my associate supervisor.

Furthermore, I would also like to thank my fellow PhD students, Victor N.-S. Bong, Stefan L.-W. Kho and Lai Jia Jiun for their friendship and help. Whenever I had questions, I was free to approach them. I even collaborated with Victor N.-S. Bong on a research paper along with Assoc. Prof. Basil T. Wong.

Next, I would like to thank the Ministry of Science, Technology and Innovation (MOSTi) of the government of Malaysia for sponsoring my research under the Science Fund (Project No. 06-02-14-SF0016). I am also grateful to Swinburne University of Technology (Sarawak Campus) for awarding me the SUTS postgraduate research studentship (SPRS).

Finally, I would like to thank my family for their support and encouragement all these years.

Abstract

A nano-gap thermophotovoltaic (TPV) system is a relatively new breed of energy converters capable of converting heat into electricity. The gap size between the radiator and the TPV cell is nanometres in length, hence the name. In this PhD thesis, the goal is to offer more theoretical insight into the optical, electrical and thermal responses of nano-gap TPV systems at the micro/nano-scale regime with respect to different parameters and configurations in order to enable engineers to make more informed design decisions.

A parametric investigation was first conducted, studying the effects of different parameters on the performance of nano-gap TPV devices. The choice of materials, cell thickness and doping concentration have heavy bearing on the near-field thermal radiation spectrum and electrical performance of the system. It is also shown that the temperature gradients in insulated gallium arsenide films exposed to near-field heating are negligibly small using the detailed phonon Monte Carlo simulation. An indium tin oxide (ITO)-based selective radiator is then proposed as a means of improving the performance of a nano-gap TPV device. The most desirable type of substrate material for the thin-film ITO layer is determined and it is also shown that converting that substrate into another thin-film layer has some interesting effects on the heat flux spectrum. Furthermore, the ability to tune the properties of the ITO layer leads to greater conversion efficiencies and power output.

Next, a nano-gap TPV device composed of a thin-film radiator and a thin-film TPV cell is studied. It is found that maintaining the TPV cell at temperatures above 300 K has some benefits though results may differ based on different cell materials. The benefits of a thin-film tungsten radiator are discussed and the effect of cell thickness is explored further. It is discovered that cell thickness could be used as a means of altering the spatial absorption profile in the cell and that a thinner cell actually experiences greater volumetric heat flux absorption. The efficiency of the nano-gap TPV device inclusive of the cooling requirement is also discussed. A phonon Monte Carlo simulation is used to study the temperature profile within the thin-film TPV cell which is exposed to convective cooling. It is shown that the temperature gradient under normal conditions remains too low to be significant. Thus, the temperature of the cell could be represented by a single temperature value.

Finally, the near-field radiative heat transfer between a radiator and a receiver in the presence of a third body in close proximity is studied. It is shown how the receiver thickness, gap sizes and the thickness of the third body affect the heat flux absorption spectrum of the receiver.

Declaration

I hereby declare that, to the best of my knowledge, this PhD thesis contains no material that has been submitted previously, in whole or in part, for the award of any other academic degree or diploma. Moreover, any other material taken from other people's work included in this thesis, published or otherwise, are fully acknowledged in accordance with standard referencing practices.



Japheth Lau Zi Jun

2018

Table of Contents

Acknowledgement	i
Abstract	ii
List of Tables	ix
List of Figures	x
Nomenclature	xiii
Chapter 1 Introduction	1
1.1 Near-field Radiative Heat Transfer	1
1.2 Near-field Thermophotovoltaics	2
1.3 Problem Statement	4
1.4 Outline of the Thesis	5
Chapter 2 Literature Review	7
2.1 Theoretical Models.....	7
2.1.1 Near-field Thermal Radiation.....	7
2.1.2 Near-field TPV	9
2.2 Experimental Results.....	11
2.2.1 Near-Field Thermal Radiation.....	11
2.2.2 Near-Field TPV	13
2.3 Selective Radiator/Emitter	14
2.4 Concluding Remarks	15
Chapter 3 Theory of Near-Field Thermophotovoltaic Systems.....	17
3.1 Near-Field Thermal Radiation	17
3.1.1 Total Internal Reflection.....	17
3.1.2 Surface Polaritons.....	20
3.1.3 Solution to the Stochastic Maxwell Equations	21
3.2 PV Cell	24

3.2.1 The <i>p-n</i> Junction	24
3.2.2 Recombination of Electron-Hole Pairs	25
3.2.3 PV Cell Characterization	26
3.3 Concluding Remarks	27
Chapter 4 Modelling and Simulation	28
4.1 Near-Field Thermal Radiation	28
4.1.1 Film Radiator	28
4.1.2 Bulk Radiator	32
4.1.3 Analytical Expression in terms of Reflection and Transmission Coefficients	32
4.2 Photovoltaic Cell Model	34
4.3 Heat Transport Model	38
4.3.1 Fourier's Law	38
4.3.2 Phonon Monte Carlo Simulation	39
4.3.3 Heat Generation	40
4.4 Concluding Remarks	41
Chapter 5 Parametric Investigation of Nano-Gap Thermo-photovoltaic Energy Conversion	42
5.1 System Configuration and Simulation Parameters	43
5.2 Radiator Materials	45
5.3 Cell Materials	47
5.4 Cell Thickness	51
5.5 Assessment of Temperature Profiles in GaAs Thin Films	53
5.6 Doping Dependence	58
5.6.1 System Configuration and Simulation Parameters	59
5.6.2 Performance	61
5.6.3 Optical Response	64
5.6.4 Electrical Response	66
5.6.5 Varying N_a	66

5.6.6 Varying N_d	69
5.6.7 Dark Current	70
5.7 Concluding Remarks	71
Chapter 6 Indium Tin Oxide-Based Selective Radiator for Nano-Gap Thermophotovoltaic Applications	72
6.1 Surface Polaritons	73
6.2 System Configuration and Simulation Parameters	74
6.3 Indium Tin Oxide	75
6.3.1 Bulk ITO	76
6.3.2 Film ITO	79
6.4 Optical Response of the Nano-Gap TPV System	79
6.4.1 Substrate-ITO Radiators	79
6.4.2 Thickness Effects	83
6.5 Performance of Nano-Gap TPV Systems with ITO-Based Radiators	90
6.6 Concluding Remarks	93
Chapter 7 Application of Thin Films to Nano-Gap Thermophotovoltaics	94
7.1 System Configuration and Simulation Parameters	96
7.2 Material Properties	97
7.2.1 Optical	97
7.2.2. Electrical	97
7.2.3 Thermal	98
7.3 Responses and Performance as a Function of Cell Temperature	98
7.3.1 Alumina Substrate	98
7.3.2 Vacuum Substrate	102
7.4 Comparing a Thin-Film W with a Bulk W Radiator	103
7.5 Responses and Performance as a Function of Cell Thickness	105
7.5.1 Optical Response and Performance	105

7.5.2 Thermal Response	107
7.5.3 Efficiency Inclusive of the Cooling Requirement	110
7.6 Heat Transport Models.....	111
7.6.1 Consistency Test.....	111
7.6.2 MC Simulation in Thin Films.....	112
7.6.3 Uniform Cell Temperature Approximation.....	115
7.7 Concluding Remarks	116
Chapter 8 The Presence of a Third Body in Near-Field Radiative Heat Exchange.....	117
8.1 System Configuration and Simulation Parameters.....	117
8.2 Results and Discussions	118
8.3 Concluding Remarks	123
Chapter 9 Conclusions and Future Work.....	124
9.1 Summary and Remarks	124
9.2 Further Recommendations	128
Appendix A.....	129
References.....	131
Vita.....	138

List of Tables

Table 5.1 GE values at $\lambda = 0.8 \mu\text{m}$	47
Table 5.2 Electrical properties at 300 K	51
Table 5.3 Parameters for modelling SiC.....	60
Table 5.4 Diffusion coefficient, lifetime and effective diffusion length of minority electrons at different acceptor concentrations.	69
Table 5.5 Diffusion coefficient, lifetime and effective diffusion length of minority holes at different donor concentrations.	70
Table 6.1 Drude model parameters for two types of ITO materials.	76
Table 6.2 Conversion efficiencies of six nano-gap TPV systems ($d_{gap} = 10 \text{ nm}$) along with their input and output power.	92
Table 6.3 Conversion efficiencies of two nano-gap TPV systems ($d_{gap} = 100 \text{ nm}$) along with their input and output power.	93
Table 7.1 Performance of the nano-gap TPV device at different T_{cell} values.	100
Table 7.2 Performance of the device using a vacuum substrate at different T_{cell} values.	103
Table 7.3 Performance of nano-gap TPV devices with different radiators with $T_{cell} = 300 \text{ K}$	103
Table 7.4 Performance of the nano-gap TPV device for two different TPV cell thicknesses both with $T_{cell} = 300 \text{ K}$	107
Table 7.5 $T_{cell,avg}$ and the maximum temperature gradient at different h_{conv} values for the two different cell thicknesses.....	110
Table 7.6 Temperature gradients generated using Fourier's law at different thermal conductivity values. $h_{conv} = 5 \times 10^2 \text{ Wm}^{-2}\text{K}^{-1}$	115

List of Figures

Fig. 1.1 Schematic of a TPV device.	2
Fig. 3.1 Interaction of a wave with an interface at critical angle of incidence [59].	18
Fig. 3.2 Schematic representation of a surface polariton propagating along the interface.	20
Fig. 4.1 Schematic diagram of a one-dimensional multi-layered system. Forward (A and B) and backward (C and D) wave amplitudes are depicted in each layer.	29
Fig. 4.2 Schematic diagram of the radiator and receiver layers.	33
Fig. 4.3 Discretization of the TPV cell.	35
Fig. 4.4 Flow chart of the MC simulation for phonon transport [85].	39
Fig. 5.1 Schematic representation of a nano-gap TPV device.	44
Fig. 5.2 Monochromatic radiative heat flux on the surface of the TPV cell for four radiator materials.	45
Fig. 5.3 (a) Monochromatic radiative heat flux on the surface of the TPV cell for three radiator-receiver combinations. (b) Monochromatic photocurrents for three radiator-receiver combinations. (c) Internal quantum efficiency for three radiator-receiver combinations.	49
Fig. 5.4 Absorption coefficient for three TPV cell materials.	49
Fig. 5.5 Monochromatic radiative heat flux penetration into a Si cell at wavelengths, (a) $\lambda = 0.4 \mu\text{m}$ and (b) $\lambda = 0.8 \mu\text{m}$	50
Fig. 5.6 Internal quantum efficiencies for varying n -type region thicknesses.	52
Fig. 5.7 Internal quantum efficiencies for varying p -type region thicknesses.	52
Fig. 5.8 Monochromatic radiative heat flux as a function of depth for varying n -region thicknesses.	53
Fig. 5.9 Temperature profile in GaAs thin-film layer at radiator temperature of 1000 K, for layer thickness of (a) $1 \mu\text{m}$, (b) $3 \mu\text{m}$ and (c) $5 \mu\text{m}$	56
Fig. 5.10 Temperature profile in GaAs thin-film layer at radiator temperature of 2000 K, for layer thickness of (a) $1 \mu\text{m}$, (b) $3 \mu\text{m}$ and (c) $5 \mu\text{m}$	57
Fig. 5.11 Schematic diagram of a nano-gap TPV device.	60
Fig. 5.12 Conversion efficiencies at different doping concentrations. (Note that only symbols represent actual data points. This is true for all figures with symbols).	61
Fig. 5.13 (a) Total absorbed radiative heat flux and (b) maximum output power at different doping concentrations.	62
Fig. 5.14 (a) Short-circuit current, (b) open-circuit voltage and (c) fill factor at different doping concentrations.	64

Fig. 5.15 Monochromatic radiative heat flux on the surface of the TPV cell as a function of angular frequency when (a) N_d is fixed at 10^{21} m^{-3} and for (b) different combinations of N_a and N_d	66
Fig. 5.16 Photocurrents, (a) J_e, J_{dp} and (b) J_h at different doping concentrations.....	67
Fig. 5.17 Excess minority carrier concentration as a function of distance into cell when (a) N_d is fixed at 10^{21} m^{-3} and (b) N_a is fixed at 10^{24} m^{-3}	68
Fig. 5.18 Dark current as a function of applied voltage at different doping concentrations. N_a is fixed at 10^{24} m^{-3}	70
Fig. 6.1 Schematic diagram of a nano-gap TPV device.	75
Fig. 6.2 Dielectric function of BK7 glass and sol-gel ITO.....	76
Fig. 6.3 Dispersion relation curve of SPPs (a) at an ITO/vacuum interface and (b) within an ITO film in vacuum.	77
Fig. 6.4 Monochromatic radiative heat flux of bulk and film ITO radiators (1000 K) on the surface of the TPV cell (300 K) for both BK7 glass and sol-gel methods.	78
Fig. 6.5 Mean energy of a Planck oscillator as a function of frequency.....	78
Fig. 6.6 Monochromatic radiative heat flux of various radiator configurations at 1000 K on the surface of the TPV cell.	80
Fig. 6.7 (a) Refractive indices and (b) extinction coefficients of various materials.....	81
Fig. 6.8 Monochromatic radiative heat flux contributions from the (a) artificial substrate material (each represented by a different constant dielectric function), (b) ITO film and (c) the sum of both contributions.	83
Fig. 6.9 Schematic diagram of a 2-film radiator nano-gap TPV system.	84
Fig. 6.10 Monochromatic radiative heat flux contributions from (a) Ag, (b) ITO and (c) the total sum of both contributions at various Ag thicknesses.	86
Fig. 6.11 Monochromatic radiative heat flux contributions from (a) W, (b) ITO and (c) the total sum of both contributions at various W thicknesses.....	88
Fig. 6.12 Monochromatic radiative heat flux contributions from (a) SiC, (b) ITO and (c) the total sum of both contributions at various SiC thicknesses.	89
Fig. 6.13 Monochromatic radiative heat flux of various radiator configurations on the surface of the TPV cell at (a) $d_{gap} = 10 \text{ nm}$ and (b) $d_{gap} = 100 \text{ nm}$. Do note that SG stands for sol gel.	91
Fig. 7.1 Schematic diagram of a nano-gap TPV device.	96
Fig. 7.2 Monochromatic radiative heat flux on the surface of the TPV cell when T_{cell} is 300 K, 400 K and 500 K.....	99

Fig. 7.3 Absorption coefficient of Si at different temperatures.	99
Fig. 7.4 Dark current as a function of forward bias when T_{cell} is 300 K, 400 K and 500 K. .	101
Fig. 7.5 Current-voltage curve and output power as a function of forward bias at different T_{cell} values.	102
Fig. 7.6 Monochromatic radiative heat flux on the surface of the TPV cell from different radiators.....	104
Fig. 7.7 Monochromatic radiative heat flux on the surface of the TPV cell at different cell thicknesses. $T_{cell} = 300$ K.	106
Fig. 7.8 Performance of a nano-gap TPV device as a function of cell thickness. Do note that only the symbols indicate actual data points.....	106
Fig. 7.9 Volumetric heat generation within the TPV cell at two different thicknesses. $T_{cell} = 300$ K.....	108
Fig. 7.10 The local radiative heat source and thermalization within the TPV cell at two different thicknesses. $T_{cell} = 300$ K.	108
Fig. 7.11 Above-band-gap heat flux absorbed by each control volume (node) within the TPV cell. $T_{cell} = 300$ K. (Normalized node 0 and 1 represent the top and bottom surfaces respectively).	109
Fig. 7.12 Temperature profiles in a 5- μ m Si film from two different heat transport models.	112
Fig. 7.13 Temperature profiles in a 1- μ m Si film exposed to enhanced volumetric heat generation and convective cooling at a simulation time of 2×10^{-8} s.....	114
Fig. 7.14 Temperature gradients (the difference between the top and bottom surface temperatures) within Si thin films at different volumetric heat generation. The open symbols represent actual data points.	114
Fig. 8.1 Schematic of a radiator-receiver system in the presence of a third body (receiver 2) in close proximity.....	117
Fig. 8.2 Monochromatic radiative heat flux absorbed by Rec1 for two Rec1 thicknesses. $d_{gap 1} = d_{gap 2} = t_{Rec 2} = 50$ nm.	119
Fig. 8.3 Monochromatic radiative heat flux absorbed by Rec1 for $d_{gap 2}$ thicknesses of (a) 20 to 100 nm and (b) 100 nm to 10 μ m. $d_{gap 1} = t_{Rec 1} = t_{Rec 2} = 50$ nm.....	120
Fig. 8.4 Monochromatic radiative heat flux absorbed by Rec1 for Rec2 thicknesses of (a) 20 to 100 nm and (b) 200 nm to bulk. $d_{gap 1} = t_{Rec 1} = d_{gap 2} = 50$ nm.	122
Fig. 8.5 Monochromatic radiative heat flux absorbed by Rec1 for different Rec2 (Au) thicknesses.	123

Nomenclature

A, B, C, D	field amplitudes
\mathbf{A}	magnetic vector potential [Wb m ⁻³]
\mathbf{B}	magnetic induction [Wb m ⁻³]
c_v	speed of light in vacuum (=2.998×10 ⁸ m s ⁻¹)
$D_{(e,h)}$	diffusion coefficient of electron / hole [m ² s ⁻¹]
\mathbf{D}	electric displacement field [C m ⁻²]
e	electron charge (= 1.6022×10 ⁻¹⁹ J eV ⁻¹)
E_g	band-gap energy [eV]
\mathbf{E}	electric field vector [V m ⁻¹]
f	distribution function
FF	fill factor
\mathbf{g}	generation rate of electron-hole pairs [m ⁻³ s ⁻¹]
$\mathbf{g}^E, \mathbf{g}^H$ = $\mathbf{g}^E = \mathbf{g}^H$	electric/magnetic Weyl component of the dyadic Green's function [m]
\mathbf{G}, \mathbf{G}	electric/magnetic dyadic Green's function [m ⁻¹]
h_{conv}	convective heat transfer coefficient [W m ⁻² K ⁻¹]
\hbar	reduced Planck's constant (= 1.0546×10 ⁻³⁴ J s)
\mathbf{H}	magnetic field vector [A m ⁻¹]
i	imaginary unit
\mathbf{I}	unit dyad
Im	imaginary part of a complex number
J	effective photocurrent [A m ⁻²]
J_0	dark current [A m ⁻²]
J_{ph}	photocurrent generated [A m ⁻²]
J_{Pm}	photocurrent at maximum power output [A m ⁻²]
J_{sc}	short-circuit current [A m ⁻²]
\mathbf{J}	current density vector [A m ⁻²]
\mathbf{J}^r	stochastic current density vector [A m ⁻²]
k	wavevector [rad m ⁻¹]
k_b	Boltzmann constant (= 1.3807×10 ⁻²³ J K ⁻¹)
k_{cond}	thermal conductivity [W m ⁻¹ K ⁻¹]
k_v	wavevector in vacuum [rad m ⁻¹]
k_z	wavevector in the z-direction [rad m ⁻¹]
k_ρ	parallel wavevector [rad m ⁻¹]
L_{dp}	thickness of depletion region [m]
m_0	electron rest mass [kg]
$m_{e,h}^*$	effective electron/hole mass [kg]
n	complex index of refraction
n_i	intrinsic carrier concentration [m ⁻³]
$n_{(e,h)}$	electron / hole concentration [m ⁻³]
$n_{(e,h)0}$	electron / hole equilibrium concentration [m ⁻³]
N_a	acceptor concentration [m ⁻³]
N_c	effective density of states in the conduction band [m ⁻³]
N_d	donor concentration [m ⁻³]
N_n	number of spatial nodes in n-type region
N_p	number of spatial nodes in p-type region

N_V	effective density of states in the valence band [m^{-3}]
P_m	maximum electrical output power [W m^{-2}]
Q_{gen}	Heat energy [J]
q	radiative heat flux [W m^{-2}]
Q	power density [W m^{-3}]
r_{ij}	Fresnel's reflection coefficient at interface ij
\mathbf{r}	position vector [m]
R_j	reflection coefficient of layer j
Re	real part of a complex number
S_{ij}	scattering matrix elements
$S_{(e,h)}$	surface recombination velocity of electron/hole [m s^{-1}]
$S^{+,-}$	amplitude of source propagating in the forward/backward direction
\mathbf{S}	Poynting vector [W m^{-2}]
t	time [s]
t_j	thickness of layer j [m]
t_{ij}	Fresnel's transmission coefficient at interface ij
T	temperature [K]
T_j	transmission coefficient of layer j
T_∞	temperature of cooling fluid [K]
V	volume [m^{-3}]
V_0	built-in voltage [V]
V_f	forward bias [V]
V_{Pm}	voltage at maximum power output [V]
$\eta_{q,\omega}$	internal quantum efficiency
α	absorption coefficient [m^{-1}]
δ	Dirac function
ε	complex electric permittivity [$\text{C}^2\text{N}^{-1}\text{m}^{-2}$]
ε_∞	high frequency dielectric constant
$\hat{\varepsilon}$	electric permittivity [$\text{C}^2\text{N}^{-1}\text{m}^{-2}$]
ε_r	dielectric function ($=\varepsilon_r' + i\varepsilon_r''$)
Θ	mean energy of a Planck oscillator [J]
λ	wavelength [m]
μ	magnetic permeability [NA^{-2}]
ρ_e	electric charge density [Cm^{-3}]
σ	electric conductivity [$\text{C}^2\text{N}^{-1}\text{m}^{-1}\text{s}^{-1}$]
$\tau_{(e,h)}$	electron / hole lifetime [s]
Φ_e	electric scalar potential [V]
ω	angular frequency [rad s^{-1}]
ω_g	band-gap frequency [rad s^{-1}]

Subscripts and superscripts

abs	absorbed
avg	average
dp	depletion region
e	electron
$evan$	evanescent
gen	generation
h	hole
l	lth layer

<i>n</i>	n-type region
<i>p</i>	p-type region
<i>ph</i>	phonon
<i>pl</i>	polarization
<i>prop</i>	propagating
<i>rad</i>	radiator
<i>ref</i>	reference
<i>tot</i>	total
ρ, θ, z	polar coordinate system

Chapter 1 Introduction

1.1 Near-field Radiative Heat Transfer

Radiative heat transfer can basically be categorised into two regimes: the far-field regime and the near-field regime. The far-field regime occurs when the separation distance between two bodies involved in radiative heat transfer is much greater than the dominant wavelength of the thermal radiation which can be calculated using the Wien law, $\lambda_w = 2897.8/T \mu\text{m}$ where T is the temperature of the emitting blackbody in kelvins. The dominant wavelength refers to the wavelength where the maximum spectral emission occurs as depicted in the Planck blackbody spectrum. In the far-field regime, the Stefan-Boltzmann law which is derived from Planck's law can be used to find the radiative heat flux emitted by a radiator as a function of temperature provided that the emissivity is known. In addition to that, methods such as the radiative transfer equation (RTE) and geometrical optics (ray optics) can be used to model light propagation. However, these methods can only be used provided that the dimensions of structures are much greater than the wavelength of the propagating light which is treated as particle-like. Because of this, they are unsuitable for describing near-field radiation where the wave nature of light is of foremost importance [1,2].

When the separation distance becomes comparable to the dominant wavelength, interesting phenomena which are referred to as near-field effects start to manifest themselves. The study of near-field radiation has its roots in the effort to overcome the diffraction limit [3] where near-field effects were exploited to increase the resolution of imaging systems. However, it has to be noted that the study of near-field effects is not restricted to the field of optics, but has seen coverage in the study of Van der Waals attraction, guided electromagnetic (EM) waves on the surface of metals and so on [3]. It was Polder and Van Hove [4] who provided the first accurate description of near-field radiative heat transfer between two bodies in close proximity.

The near-field regime is characterised by the existence of evanescent waves which are surface waves that decay exponentially away from the interface. Due to that exponential decay, evanescent waves have no effect on radiative heat transfer when the separation distance is great. However, when two bodies are brought really close to each other in the near-field regime,

evanescent waves on both bodies would couple and produce another channel of heat transfer called photon tunnelling or radiation tunnelling. The radiative heat flux generated by photon tunnelling can be orders of magnitude greater than the heat flux calculated within the blackbody limit. Evanescent waves can be generated by total internal reflection (TIR), surface plasmon-polaritons (SPP) or surface phonon-polaritons (SPhP). These will be discussed in detail in Chapter 3. There are other theoretically known types of surface polaritons [5-7] which exist in specially-designed magnetic materials. However, we will only be dealing with non-magnetic materials (as required by the fluctuation dissipation theorem detailed in Section 3.1.3), thus these special surface polaritons are beyond the scope of this thesis. Near-field radiative transfer sees potential applications in a variety of areas such as in scanning thermal microscopy [8,9], in nano-fabrication [10,11] and in near-field cooling [12]. In this thesis, we will be focusing on a specific application of near-field thermal radiation in the form of energy generators called near-field thermophotovoltaic (TPV) systems.

1.2 Near-field Thermophotovoltaics

A thermophotovoltaic device is an energy converter that converts heat into electricity. As shown in Fig. 1.1, it consists of two main components: the radiator which emits thermal radiation and the photovoltaic (PV) cell or receiver which produces electricity.

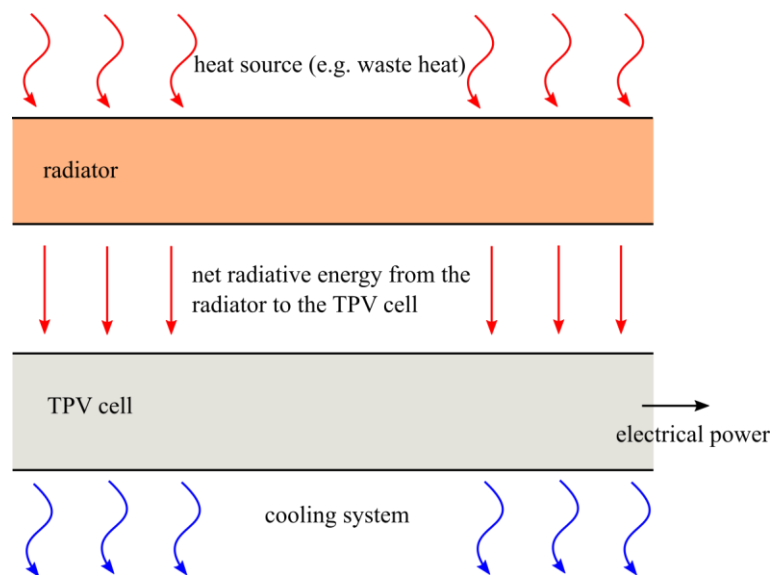


Fig. 1.1 Schematic of a TPV device.

In this thesis, the PV cell used in TPV systems will be called a TPV cell to differentiate it from its solar-dependent counterpart. TPV devices are more versatile than conventional PV cells in that they can be powered by a variety of energy sources such as the sun, fuel and waste heat. The operation of a TPV device is rather straightforward. The radiator is heated up by an energy source, elevating its temperature above the temperature of the receiver. This generates a net radiative heat flux that is transferred to the receiver which absorbs the incoming radiation. If the energy of the radiation is above the band-gap energy of the receiver or TPV cell, photogenerated current is produced. When a load is connected to the TPV cell with the necessary bias (applied voltage), a net current would flow, generating power.

The concept of the TPV device first appeared around the late 50s and early 60s. Pierre Aigrain, Henry H. Kolm and John J. Werth are often cited as pioneers of this technology [13,14]. The United States army and industrial players such as General Motors were interested in the prospect of turning heat into electricity using a portable, low-noise device and so were actively involved in the early years of TPV development [13]. However, despite their versatility, TPV devices suffer from low power throughput and conversion efficiencies [15]. To remedy this setback, researchers have developed selective radiators, filters and back reflectors to tune the thermal emission and to reflect or filter the unusable part of the spectrum [14].

Another way to increase power throughput and efficiency would be to take advantage of the near-field regime. This is achieved by reducing the gap between the radiator and receiver to distances comparable to the dominant wavelength. Such devices are called near-field TPVs as most of the radiative heat transfer is caused by near-field effects namely, photon tunnelling. The greater radiative heat flux allows for more electrical power to be generated and by exploiting the spectral coherence of resonant surface waves, the radiation can be tuned to improve the conversion efficiency of the device. The first numerical predictions of near-field TPVs showed that this particular breed of energy converters outperforms traditional TPV devices in terms of their electrical throughput with marginal improvements in efficiency [16,17].

One exciting avenue for the implementation of this technology is in waste heat recovery. Power plants and industries such as steel-making and glass-making produce a lot of heat as a by-product. Unfortunately, this potential source of energy often ends up getting released to the environment and is thus wasted. Near-field TPV technology could dramatically change the

current situation by harnessing industrial thermal emissions to generate clean electrical energy. This would not only help in meeting electricity demands but also benefit the environment.

1.3 Problem Statement

Near-field TPV is still a relatively new kind of technology with much to discover. In order to design a highly optimized near-field TPV system, more understanding is required with regards to the influence of the different parameters involved and the configuration of the system. The parameters may include material choice, material combinations, layer thicknesses and so on. It is important that we understand how these factors influence the optical, electrical and thermal responses of the system. With regards to thickness, we know that as a medium goes from bulk to thin film, its properties and responses would undergo changes. It would be interesting to observe how such changes affect the overall performance of a near-field TPV device. Furthermore, near-field TPV systems that utilise bare bulk radiators are limited in terms of their conversion efficiencies due to the broadband nature of the radiation. It is crucial that researchers find methods to improve upon the efficiency of the system in order to make it viable and practical. These are all important issues that will be addressed as best as we can in this thesis. The main goal is to offer more theoretical insight into the optical, electrical and thermal responses of near-field TPV systems during operation with respect to the different parameters and configurations of such systems in order to enable engineers to make more informed design decisions. We will be dealing specifically with nano-gap TPV systems where the separation distance between the radiator and the TPV cell is nanometres in length. The objectives of this work can be summarized as follows:

- i. To simultaneously model near-field radiative exchange and electrical-thermal responses of nano-gap TPV systems,
- ii. To study the effects of different parameters such as radiator material, TPV cell material, cell thickness and doping concentration on the responses and performance of the system,
- iii. To propose a tuneable selective radiator for improving the performance of a nano-gap TPV system,
- iv. To explore the advantages and disadvantages of using thin films in nano-gap TPV systems

- v. To explore the behaviour of a radiator-receiver system in close proximity to a third body.

1.4 Outline of the Thesis

In this section, we present the outline of this thesis. A survey of the literature concerning near-field radiative heat transfer and near-field thermophotovoltaics is presented in Chapter 2. The chapter reviews published work on theoretical models, experimental work and selective radiators for nano-gap TPV applications.

The fundamentals of near-field radiation and the photovoltaic effect are explored in Chapter 3. With regards to near-field radiation, phenomena such as evanescent waves and surface waves are explained followed by the derivation of the time-averaged Poynting vector through solving the stochastic Maxwell equations based on the fluctuational electrodynamics formalism. In the second part of Chapter 3, a discussion on the formation, operation and characterization of a PV cell is presented.

In Chapter 4, the mathematical models and simulation method to be used in subsequent chapters are detailed. The numerical simulation can be broken down into three main parts, namely, optical, electrical and thermal. The optical component attempts to simulate near-field radiative heat exchange between the radiator and the receiver. The electrical component models the operation of a TPV cell and the thermal component models heat generation and heat transport in the cell.

In Chapter 5, several parameters that influence the responses and performance of nano-gap TPV devices are analysed. The parameters include the radiator material, TPV cell (receiver) material, cell thickness and doping concentration. The focus is on how these parameters alter the optical, electrical and thermal responses of nano-gap TPV devices.

In Chapter 6, a selective radiator based on indium tin oxide (ITO) is proposed as a means of improving the performance of nano-gap TPV devices. Two types of ITO processing techniques are introduced. The effects of the substrate material's (upon which the ITO layer is deposited) dielectric function and thickness on the near-field radiative heat transfer are also discussed.

Finally, the enhancement of nano-gap TPV performance through tuning the properties of ITO is demonstrated.

An analysis of a thin-film nano-gap TPV device is presented in Chapter 7. By thin-film, it is meant that both the radiator and the receiver have thicknesses of 1 μm and below. The effect of cell temperature and cell thickness on the responses and performance of the device is discussed. A qualitative discussion on the conversion efficiency inclusive of the cooling requirement is also presented. Furthermore, a detailed heat transport analysis is conducted on Si thin films with particular emphasis on the temperature gradient in the films.

In Chapter 8, we analyse the radiative exchange between a radiator and a receiver in the presence of a third body in close proximity to the receiver. The effects of medium thickness and the vacuum gap size between the receiver and the third body on the heat flux absorption spectrum of the receiver are observed and discussed.

The results of this thesis are summarized in Chapter 9 and future recommendations for research work are also provided.

Chapter 2 Literature Review

In this chapter, we go through the literature on theoretical models and experimental results concerning near-field thermal radiation and near-field TPV systems followed by a survey of selective radiator designs proposed for near-field TPV applications. We will be building upon the work of these researchers in an attempt to accomplish the objectives laid out in Section 1.3.

2.1 Theoretical Models

2.1.1 Near-field Thermal Radiation

Cravalho et al. [18] were one of the first to present a quantitative analysis of near-field thermal radiation transfer between two solids. In their work, they introduced two phenomena that influence near-field radiative heat transfer, which are wave interference and radiation tunnelling. They derived a solution through the use of electromagnetic wave theory and proceeded to calculate the near-field radiative heat flux exchanged between two dielectrics separated by a vacuum gap. Their solution involved determining the transmissivity of the geometry in question. In a related paper, Beohm and Tien [19] predicted the radiative transfer between two closely-spaced metals separated by a non-conducting dielectric. Once again, electromagnetic wave theory is used to derive a solution to the transmitted energy. It has to be noted that both studies only considered total internal reflection as the source for evanescent waves without taking into account other possible modes.

The first accurate heat flux calculation was done by Polder and Van Hove [4]. They used the fluctuational electrodynamics (FE) formalism pioneered by Rytov [20] and the fluctuation-dissipation theorem (FDT) to describe the source of emission. They calculated the radiative transfer between two metals across a diminishing gap and found that their predictions are in qualitative agreement with experimental results. Mulet et al. [21] demonstrated that surface phonon-polaritons that can be generated in certain materials produce quasi-monochromatic radiative heat transfer between two objects.

Narayanaswamy and Chen [22] studied near-field thermal radiation in one-dimensional layered media and developed a general formulation to describe it. They used a combination of the

Maxwell equations (ME) and the FDT to compute the thermal emission directly from the emitting structure. Lee et al. [23,24] introduced a way to visualize the Poynting vector which is used to calculate the near-field radiative heat flux.

Francoeur et al. [25,26] discussed the fundamentals of near-field heat transfer and came up with a procedure to solve a near-field heat transfer problem in one-dimension. The electromagnetic wave emanating from the radiator was described using ME. However, ME do not include a description of the source of the radiation. To solve this, a randomly fluctuating current source was introduced from which the radiation emanates. This yields stochastic ME whose solution accounts for the near-field phenomena of wave interference and radiation tunnelling. The numerical solution was solved using dyadic Green's functions and the scattering matrix method. The modified version of the T-matrix approach, called the scattering matrix (S-matrix) method, was proposed by Auslender and Hava [27]. The procedure was then used to predict the near-field radiative heat transfer involving cubic boron nitride separated by a vacuum gap.

As evidenced by this survey, most of the models used by researchers are based on the work done by Polder and Van Hove [4] which assumes locality of the dielectric functions. Due to the fact that non-local effects are not taken into account, the theory predicts a radiative heat flux value that diverges as the separation gap between the radiator and the receiver approaches zero [28] which is inconsistent with experimental results. Wang et al. [29] developed a more fundamental theory that incorporates non-local effects and also describes non-equilibrium steady states. The new theory uses the non-equilibrium Green's function (NEGF) formalism to derive an expression for the radiative heat flux. In their paper, they dealt exclusively with radiative heat transfer between metal plates. In order to model the interaction between electrons and electromagnetic fields, they couple a tight-binding model of the electrons with the radiative field in a quantized form. It has to be noted that their model does not include evanescent modes. They compared the results of their calculations with that using Polder and Van Hoves' theory and discovered that they are relatively consistent except for really small separation gaps. Their model correctly predicts that the radiative heat flux saturates as the gap size becomes comparable to atomic lattice constants.

2.1.2 Near-field TPV

Whale [16] investigated the phenomenon of near-field thermal radiation and provided an analysis of the performance of a microgap-TPV device. He proposed a way to incorporate FE into the analysis. To provide a deeper understanding of the FE approach, Whale introduced the proximity function which describes the frequency-dependence of the spacing effect. In short, it details the wave interference and radiation tunnelling effects. Whale also developed a model of a microgap-TPV device by deriving equations that describe the behaviour and properties of the device. He then presented an FE formulation that incorporates the microgap-TPV operating conditions under investigation. He first explained why the equilibrium FDT can be applied to a TPV system. Even though a TPV device is not strictly in thermodynamic equilibrium, it can be taken to be in local thermodynamic equilibrium owing to the fact that the electron-phonon interactions are rapid enough to return the system to an equilibrium state after being energized by photons. In his analysis, Whale used a linear form of FDT to relate the source current and the electric field. An FE formulation that accounts for a large temperature difference between two surfaces was then presented. Whale modelled the TPV cell as an indium gallium arsenide (InGaAs) and mercury cadmium telluride (HgCdTe) p - n junction. The radiator was modelled as a low-conductivity material by using the Drude model.

Narayanaswamy and Chen [30] analysed a near-field TPV system that utilises a cubic boron nitride (cBN) radiator (maintained at 1000 K) supporting SPhPs. They used a combination of the Green's functions and the FDT to solve for the magnitude of the Poynting vector in the z direction which was subsequently used to determine the thermal radiative heat flux absorbed by the TPV cell. To be more precise, the absorbed heat flux value was found by calculating the difference between the Poynting vector magnitudes at the top and bottom surfaces of the cell. The TPV cell (maintained at 300 K) was modelled as a direct band-gap semiconductor using a fictitious dielectric function. Furthermore, they also calculated the photon overexcitation efficiency which they define as the portion of absorbed radiative energy that is usable. Using these methods, they showed that their proposed near-field TPV system supplied more power to the cell compared to absorption by solar irradiation. Moreover, with SPhPs excited, they achieved a photon overexcitation efficiency of 0.86 compared to 0.445 for a blackbody radiator.

Laroche et al. [31] studied a theoretical nano-gap TPV system which consisted of a bulk radiator (maintained at 2000 K) paired with a bulk gallium antimonide (GaSb) TPV cell

(maintained at 300 K). Furthermore, two types of radiators were used, namely, a tungsten (W) radiator and a quasi-monochromatic source described by the Drude model. They used the electromagnetic approach pioneered by Rytov [32] and established by Polder and Van Hove [4] to derive the spectral radiative heat flux between the radiator and the TPV cell. Quantities such as the photogenerated current, open-circuit voltage, electrical power and fill factor were all calculated analytically. Furthermore, they performed theoretical calculations to study the effect of near-field thermal radiation on the electron-hole pair lifetime using the analytical equation for the normalized recombination rate in GaSb. They discovered that the near-field thermal radiation has no effect on the lifetime.

Park et al. [33] developed a model of a nano-gap TPV device which utilises a tungsten radiator at 2000 K emitting a dominant wavelength of 1.5 μm and an $\text{In}_{0.18}\text{Ga}_{0.82}\text{Sb}$ TPV cell with a band gap of 0.56 eV. The device was represented as a multi-layered structure and its radiative heat flux was solved using the dyadic Green's functions as part of the FE formalism. They highlighted the effects of near-field thermal radiation on photon penetration depth. Moreover, the absorption of the radiative heat flux by the TPV cell received considerable attention in this work. The current generation was calculated based on the photo-generation capability of the TPV cell and also recombination processes that happened as a result.

Francoeur et al. [34] came up with a more comprehensive model to describe a nano-gap TPV device. The radiative heat transfer through a nanoscale vacuum gap was described using a combination of ME and the FDT based, once again, on the FE formalism. Building upon the work by Park et al. [33], they included the thermal effects in their analysis of nano-gap TPV cells. A model of coupled near-field thermal radiation, charge and thermal transport in a nano-gap TPV cell was developed. This model simulates the behaviour of near-field thermal radiation, minority carrier movement and the transport of heat within the cell. Francoeur et al. evaluated the performance of a nano-gap TPV device using the model they developed by solving for photocurrents and efficiencies. The output power was obtained from the J - V characteristic of the cell. They provided detailed descriptions of the optical, electrical and thermophysical properties of the TPV cell. The dielectric functions of the radiator and the TPV cell were modelled along with other TPV cell properties which are necessary for simulations. They included the intrinsic carrier concentration, depletion region thickness, diffusion coefficients, minority carrier lifetimes and the thermal conductivity.

2.2 Experimental Results

2.2.1 Near-Field Thermal Radiation

Experiments have been conducted to measure the near-field radiative transfer between closely-spaced bodies. Domoto et al. [35] were one of the first to do this when they successfully measured the radiative transfer between two parallel copper disks with gaps as small as 10 μm . They observed heat flux enhancements when the regime was in the near-field. However, the measured heat flux amounted to only a small portion of the energy transfer between blackbodies. Hargreaves [36,37] measured the radiative transfer between chromium plates with the smallest gap width measuring 1.5 μm where significant near-field enhancement was observed as compared to far-field measurements. Xu et al. [38] were able to achieve gaps smaller than 1 μm between an indium needle and gold plates. However, their measured heat transfer rate is smaller than what is predicted using Polder and Van Hoves' theory.

Kittel et al. [8] measured the near-field heat transfer between the tip of a thermal profiler and a plate made of either gold or gallium nitride. They were able to achieve vacuum gaps as small as 1 nm. They discovered that for gap sizes above 10 nm, the measured results matched well with theoretical predictions made using FE. However, at smaller gaps, their experimental results started to deviate from predicted values. They attributed this discrepancy to the non-local effects of the dielectric function which when added to theoretical calculations yielded predictions which were consistent with their experimental results.

Hu et al. [39] measured the near-field radiative transfer between two glass plates separated by a vacuum gap which they set to be 1- μm thick through the use of polystyrene microspheres. However, their experimental results only matched the theoretical predictions using a 1.6- μm gap, leading them to suggest that the polystyrene particles may have deviations in their diameters. The measured heat flux exceeded blackbody radiation predictions by 35 % due to contributions from SPhPs. Narayanaswamy et al. [40] used a bi-material atomic force microscope cantilever to measure the near-field radiative heat transfer between a silica sphere and a silica substrate. They achieved gaps as small as 0.1 μm and measured conductance values which exceeded predictions using the blackbody radiation theory.

Ottens et al. [41] measured the radiative heat transfer between two sapphire plates. They used a stepper motor to adjust the tilt, tip and spacing of the plates. Gap sizes between 2 to 100 μm were used and they achieved a temperature difference of 19 K between the hot and cold plates. They reported consistency between experimental and theoretical results. Kralik et al. [42] on the other hand measured the near-field radiative heat transfer between parallel surfaces of tungsten with gap sizes between 1 and 100 μm . The greatest temperature difference achieved in their near-field measurements was around 55 K. Once again, there is good consistency between the experimental and theoretical results. Another experiment conducted by Ijiro and Yamada [43] saw excellent agreement between experimental and theoretical predictions. They measured the radiative heat transfer between plates of silicon oxide, SiO_2 with gap sizes of 1 to 50 μm and temperature differences of up to 19.5 K. Furthermore, they discovered that microcavities on the plate surfaces significantly enhanced near-field radiative heat transfer.

Ito et al. [44] used micromachined spacers to achieve gap sizes as small as 500 nm between two quartz substrates. They reported that measured heat flux values were not more than twice the theoretical predictions owing to suppressed parasitic heat conduction. Watjen et al. [45] measured the near-field thermal radiation between parallel plates of doped silicon, Si. Vacuum gaps as small as 200 nm were achieved using SiO_2 spacers. They found good agreement between experimental results and theoretical predictions using FE albeit with a certain percentage of uncertainty. This effectively proves the FE formalism for parallel plates with vacuum gaps of a few hundred nanometres.

St-Gelais et al. [46] were able to reduce the gap between parallel nanobeams down to 54 nm using high precision micro-electromechanical displacement control. Using the FE formalism, theoretical predictions were obtained which matched the experimental results rather well. However, at gaps greater than 150 nm, experimental values slightly exceeded theoretical values. It was suggested that the cause of this discrepancy could be due to the difference between the actual material absorption coefficient and the simulated one.

Song et al. [47] conducted experiments to study the dependence of near-field thermal radiation on film thickness. SiO_2 films of varying thicknesses were coated onto a receiver platform which was exposed to near-field thermal radiation from a SiO_2 spherical radiator. A gap as small as 20 nm between the radiator and the receiver was achieved using a specially designed calorimetric platform. They discovered that the thickness effects of the film come into play

when the gap size is comparable to the film thickness. They were able to theoretically explain their experimental results and attributed the film-thickness dependence of the near-field thermal radiation to SPhPs present on the surface of SiO₂.

Kloppstech et al. [48] managed to measure the near-field thermal radiative heat flux at gaps of 0.2 to 7 nm by pairing a gold-coated near-field scanning thermal microscope and a planar gold sample. They reported extremely high heat-flux enhancement four orders of magnitude larger than values predicted using FE. They proceeded to search for other accepted heat-transfer models that could explain this phenomenon. They found that non-local effects do increase the heat flux but the predicted enhancements were much smaller than their experimental results. They then considered phonon tunnelling as a possible explanation but found that this too was unsatisfactory. It was concluded that further theoretical exploration in the regime where both radiative and conductive effects are present was needed. Cui et al. [49] performed a similar experiment using a gold-coated probe and a gold substrate. They were able to achieve gap sizes of 5 nm down to a few Å. They discovered that theoretical predictions using FE were largely consistent with measured values even for such small gap sizes. However, for gaps below 1 nm, they admit that it is difficult to make definitive conclusions due to noise in their experimental measurements.

2.2.2 Near-Field TPV

Dimatteo et al. [50] developed an experimental micron-gap TPV (MTPV) device to verify theoretical predictions of significant enhancements in performance over traditional TPV devices. Their experimental set-up uses a Si heater chip as the radiator and an indium gallium arsenide, InGaAs TPV cell. Specially designed tubular SiO₂ spacers are used to maintain micrometric vacuum gaps as small as 0.12 μm between the radiator and the TPV cell. These special spacers are able to reduce parasitic heat conduction by more than 10 times compared with previous spacers used. They managed to confirm enhancements to both the short-circuit current, J_{sc} and the open-circuit voltage, V_{oc} . Dimatteo and his team also presented new TPV cell designs for their MTPV device which allows for greater output power enhancements.

Hanamura and Mori [51] constructed a nano-gap TPV system composed of a W radiator and a GaSb TPV cell. They discovered that for vacuum gaps less than 10 μm, the near-field radiative

exchange greatly increased due to photon tunnelling. Moreover, as the gap decreases, they were able to obtain increasing current densities and output power.

2.3 Selective Radiator/Emitter

Chang et al. [52] proposed a theoretical selective radiator which consists of a doped Si radiating layer containing nano-hole arrays and a layer of graphene which is overlaid on the receiver. They were able to achieve strong SPP coupling between the radiating Si layer and the graphene layer which are separated by a 20-nm gap. They discovered that changing the doping concentration of the radiating Si layer affects the resonant mode at the radiator-vacuum interface and changing the chemical potential of graphene alters the resonant mode at the vacuum-receiver interface. By optimizing the doping concentration and chemical potential, they were able to produce a near-field radiative heat flux enhancement of five hundred times more than the far-field blackbody limit for temperatures of 400 K for the radiator and 300 K for the receiver.

Fernandez-Hurtado et al. [53] proposed the use of Si-based metasurfaces to enhance near-field radiative heat transfer. They theoretically investigated the radiative heat transfer between two Si metasurfaces separated by a separation gap that varies from 13 nm to 2 μm . It has to be noted that in practical applications, the radiator may not be paired with the same material. Thus, there are practical limitations to this approach. The metasurfaces feature two-dimensional periodic arrays of square holes on the surface of doped Si. Using these nano-structures, they were able to tune the dispersion relation of SPPs by changing geometrical parameters such as the lattice constant, the distance between holes, the gap size and the metasurface thickness. They were able to obtain a near-field radiative heat conductance that is much higher than any unstructured material e.g. SiO_2 plates.

Chang et al. [54] studied a theoretical near-field TPV system that uses a hyperbolic metamaterial (HMM) radiator made from W nanowire arrays embedded in aluminium oxide (Al_2O_3). They paired the radiator with an InGaSb TPV cell across a nanometric vacuum gap. They discovered that the epsilon-near-pole and hyperbolic modes in the HMM radiator enhance the radiative energy at different polarizations. They showed that by changing the filling ratio of the HMM (i.e. the size of the nanowires), they were able to alter the radiative heat flux. Thus,

they were able to achieve a power output that is 2.15 times the value achieved with a plain W radiator at a gap of 20 nm.

Jin et al. [55] performed a theoretical analysis of a near-field TPV system that pairs a HMM radiator at 1000 K with an indium arsenide (InAs) cell at 300 K. The HMM radiator consists of alternating layers of W and SiO₂ with variable thicknesses. The dispersion relation of waves inside the HMM is hyperbolic as opposed to elliptical, thus allowing evanescent waves to propagate. This phenomenon allows for the manipulation of these evanescent waves by changing the thicknesses of each layer in order to tune the near-field thermal radiation. After optimization, they were able to achieve an electric power output that is six times more than when a plain W radiator is used. They explained that the enhancement is the result of coupled plasmon modes at the metal-dielectric interfaces in the HMM radiator.

Yang et al. [56] proposed a multi-layered radiator with alternating layers of W and Al₂O₃ as a means of improving the performance of near-field TPV systems and is consistent with the work of Jin et al. [55]. Their radiator design is based on the work done by Narayanaswamy and Chen [57] who studied its effects in the far-field regime. They reported that most of the energy emission comes from the last W layer adjacent to the vacuum gap and the heat flux enhancement can be attributed to the SPP coupling in each W thin film. Moreover, they discovered that by changing the thicknesses of the alternating layers, the spectral near-field radiative heat flux profile could be altered. They found that the optimum thicknesses for the W and Al₂O₃ layers are 10 nm and 300 nm respectively for a radiator with a total of 20 layers. The optimization maximized the spectral radiative heat flux above the In_{0.18}Ga_{0.82}Sb TPV cell band gap of 0.56 eV which greatly enhances the power output when compared to a system that uses a plain W radiator. However it has to be noted that the conversion efficiency suffered when the multi-layered radiator was used.

2.4 Concluding Remarks

We have surveyed relevant research in the fields of near-field thermal radiation and near-field TPV and it is clear that fluctuational electrodynamics has become a well-established theoretical description of near-field radiative heat transfer. It mathematically describes the physical phenomena involved in near-field radiation heat transfer and is able to produce predictions

which are consistent with experimental results. Furthermore, the FE formalism has been successfully incorporated into the simulation of near-field TPV systems. These models or simulations predict greatly increased electrical power generation which is consistent with what researchers observe when conducting near-field TPV experiments. Thus, we can be confident that the FE formalism is theoretically robust and provides us with a reliable way to model near-field thermal radiation. However, it is only accurate as long as non-local effects do not play a significant role in the radiation exchange. There are alternative models which take non-local effects into account but are not well established yet. Thus, more work needs to be done in modelling radiation in the extreme near-field where FE breaks down. Though having said that, this formalism is applicable to most configurations, even where gap sizes are only a few nanometres wide [49].

We have also surveyed several proposals for selective radiators designed to manipulate the near-field thermal radiation spectrum which could lead to performance improvements in near-field TPV systems. Almost all of them involve the use of meta-materials which take advantage of surface waves to enhance or tune the near-field thermal radiation spectrum. The same strategy will be used in Chapter 6 in designing a selective radiator. It is worth noting that the aforementioned proposals are all theoretical; it would be interesting to know if the same enhancements can be achieved experimentally. However, that is beyond the scope of this thesis.

Chapter 3 Theory of Near-Field Thermophotovoltaic Systems

In this chapter, the fundamentals of near-field TPV systems are detailed. Such systems are broken down into two main components: the near-field thermal radiation problem and the photovoltaic effect that occurs in the TPV cell. It is imperative that these two components are well understood before one can come up with an accurate description of a near-field TPV device.

3.1 Near-Field Thermal Radiation

As mentioned in the introduction, near-field thermal radiation exchange occurs when the separation distance between two bodies exchanging radiative energy is comparable to the dominant wavelength of the radiation. At such geometries, the classical theory based on the blackbody concept breaks down as it only deals with incoherent radiation. The coherence length of a blackbody emission is of the same order of magnitude as its dominant wavelength [58]. Thus, in the near-field regime, the wave nature of radiation cannot be neglected requiring the use of the Maxwell equations to solve the radiative heat transfer problem. Moreover, in the near-field regime, both propagating waves and evanescent waves are involved in the heat transfer. Evanescent waves are the mechanism of interest here due to their ability to induce photon tunnelling which greatly increases radiative heat transfer.

3.1.1 Total Internal Reflection

In this section, we describe how evanescent waves are generated by the phenomenon of TIR based on electromagnetic wave theory. Consider the arrangement in Fig. 3.1 where a plane wave is propagating through medium 1 and is subsequently reflected at the interface separating the first and second media. The refractive index of medium 1, n_1 is greater than the refractive index of medium 2, n_2 and it is assumed that both media are non-absorbing dielectrics. Do note that the conclusions presented here apply to absorbing media as well. For the sake of simplicity, we will limit our analysis to the electric field of TM-polarized waves which oscillates parallel to the plane of incidence x - z . The same analysis can be applied to the magnetic field and extended further to include TE-polarized waves.

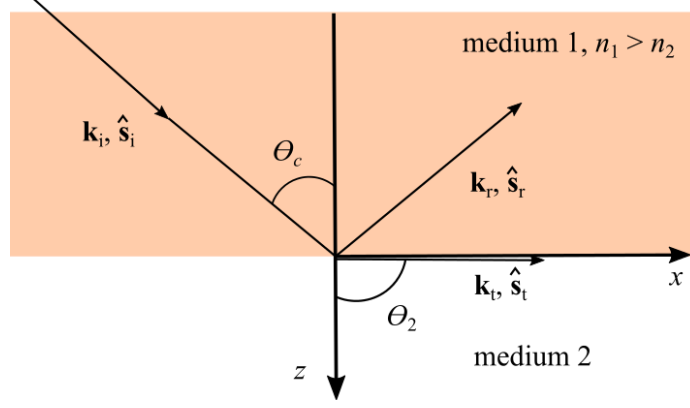


Fig. 3.1 Interaction of a wave with an interface at critical angle of incidence [59].

The electric fields in media 1 and 2 are given as [59,60]:

$$\mathbf{E}_1 = \mathbf{E}_{\parallel i} e^{i(\mathbf{k}_i \cdot \mathbf{r} - \omega t)} + \mathbf{E}_{\parallel r} e^{i(\mathbf{k}_r \cdot \mathbf{r} - \omega t)} \quad (3.1)$$

$$\mathbf{E}_2 = \mathbf{E}_{\parallel t} e^{i(\mathbf{k}_t \cdot \mathbf{r} - \omega t)} \quad (3.2)$$

where the complex electric field in medium 1, \mathbf{E}_1 consists of contributions from the incident and reflected waves while \mathbf{E}_2 is the electric field of the transmitted wave in medium 2. The term \mathbf{E}_{\parallel} refers to the amplitude vector of the electric field orthogonal to the direction of propagation in the plane of incidence. The wavevector, \mathbf{k} has both x and z -components and is written as [59]:

$$\mathbf{k} = k_v n \hat{\mathbf{s}} = k_x \hat{\mathbf{i}} + k_z \hat{\mathbf{k}} \quad (3.3)$$

where $\hat{\mathbf{s}}$ is the direction vector in the direction of propagation. The x -components of the wavevector, \mathbf{k} (i.e. k_x of each wave) are identical due to the fact that the tangential components (along the x -axis) of the electric field are conserved [59], thus yielding:

$$k_x = k_v n_1 \sin \theta_1 = k_v n_2 \sin \theta_2 \quad (3.4)$$

The z -component of the wavevector of the transmitted wave can now be written as:

$$k_{zt} = \sqrt{(k_v n_2)^2 - k_x^2} = k_v \sqrt{n_2^2 - (n_1 \sin \theta_1)^2} \quad (3.5)$$

Based on Eq. (3.5), it is clear that the angle of the incident wave, θ_1 has a huge bearing on the nature of the transmitted wave. If θ_1 is greater than the critical angle, θ_c it follows that $n_1 \sin \theta_1 > n_1 \sin \theta_c > n_2$. This would in turn cause k_{zt} to become purely imaginary which when substituted into Eq. (3.2) gives:

$$\mathbf{E}_2 = \mathbf{E}_{\parallel} e^{i(k_x x - \omega t)} e^{-k_{zt} z} \quad (3.6)$$

Thus we obtain a transmitted wave that propagates along the interface 1-2 and whose amplitude decays exponentially in the z -direction. In the far-field the z -component of the time-averaged Poynting vector is zero [58], expressing the fact that there is no net energy flow across the interface. However, when a third medium which is denser than the second is brought really close to the first, a net flow of energy across medium 2 is observed. As stated in the introduction this interesting phenomenon is called photon tunnelling or radiation tunnelling or in some cases frustrated total internal reflection. The physical picture can be described as follows: when the third medium is brought close to the first within the penetration depth of the evanescent wave, the second interface causes the evanescent field to be reflected back to the first interface. The interference between the two waves produces a Poynting vector with a non-zero component in the z -direction [59]. This kind of energy transfer can be further illustrated by studying the transmissivity of medium 2 when TIR occurs. For a non-absorbing system of three dielectrics with $n_1 = n_3 > n_2$ and for angles $\theta_1 > \theta_c$, the spectral transmissivity of medium 2 can be written as [59]:

$$T_\lambda = \frac{\sin^2 2\alpha}{\sin^2 2\alpha + \sinh^2 \left(2\pi n_2 |\cos \theta_2| \frac{d_2}{\lambda} \right)} \quad \text{where, } \tan \alpha = \begin{cases} \frac{n_1 |\cos \theta_2|}{n_2 \cos \theta_1}, & \text{TM - polarized} \\ \frac{n_2 |\cos \theta_2|}{n_1 \cos \theta_1}, & \text{TE - polarized} \end{cases} \quad (3.7)$$

An inspection of Eq. (3.7) reveals that the transmissivity increases when the thickness of medium 2, d_2 decreases. Furthermore, the greater the incident angle, θ_1 the smaller d_2 has to be in order to produce any noticeable transmissivity implying that the strength of the evanescent wave decays faster the greater the incident angle [59].

3.1.2 Surface Polaritons

Surface polaritons (SP) are surface waves which result from the coupling between an electromagnetic field and a resonant oscillation of energy carriers in the material. A SP generated by the coupling between electromagnetic radiation and the collective oscillation of free electrons is called a surface plasmon-polariton which occurs at the interfaces of metals and doped semiconductors. At the interfaces of dielectrics, the coupling between electromagnetic radiation and optical phonons produces SPs which are called surface phonon-polaritons [61]. As shown in Fig. 3.2, these SPs propagate along the interface of two different materials, forming evanescent fields which decay normal to the interface between the two media [62,63].

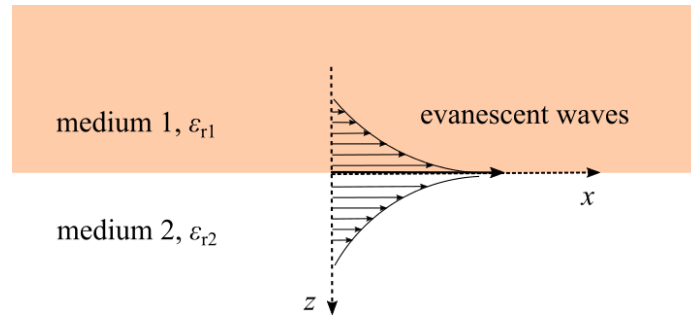


Fig. 3.2 Schematic representation of a surface polariton propagating along the interface.

The conditions for the existence of surface polaritons can be determined by finding the poles of the Fresnel reflection coefficients based on the fact that resonance produces diverging reflection coefficients [59]. The reflection coefficients in terms of the z -component of the wavevectors are [64,65]:

$$r_{12}^{TM} = \left(\frac{k_{z1}}{\epsilon_{r1}} - \frac{k_{z2}}{\epsilon_{r2}} \right) / \left(\frac{k_{z1}}{\epsilon_{r1}} + \frac{k_{z2}}{\epsilon_{r2}} \right) \quad (3.8)$$

$$r_{12}^{TE} = \left(\frac{k_{z1}}{\mu_1} - \frac{k_{z2}}{\mu_2} \right) / \left(\frac{k_{z1}}{\mu_1} + \frac{k_{z2}}{\mu_2} \right) \quad (3.9)$$

Equations (3.8) and (3.9) are divergent when their denominators are zero:

$$\frac{k_{z1}}{\epsilon_{r1}} + \frac{k_{z2}}{\epsilon_{r2}} = 0, \text{ TM} \quad (3.10)$$

$$\frac{k_{z1}}{\mu_1} + \frac{k_{z2}}{\mu_2} = 0, \text{ TE} \quad (3.11)$$

In order to generate evanescent fields, both k_{z1} and k_{z2} have to be pure imaginary numbers and have the same signs so that the reflected wave decays in the negative z -direction i.e. $e^{i(\mathbf{k}_r \cdot \mathbf{r})} = e^{i(k_{x1}x - ik_{z1}z)} = e^{ik_{x1}x + k_{z1}z}$ and the transmitted wave decays in the positive z -direction i.e. $e^{i(\mathbf{k}_t \cdot \mathbf{r})} = e^{i(k_{x2}x + ik_{z2}z)} = e^{ik_{x2}x - k_{z2}z}$ [59]. Thus, in order to satisfy Eq. (3.10), the dielectric functions of the two media, ϵ_{r1} and ϵ_{r2} , have to have opposite signs. If, for example, vacuum is paired with a metal whose real part of its dielectric function is negative, a TM-polarized wave can be used to excite SPs. However, if one wishes to excite SPs using TE-polarized waves, one of the media has to have a negative magnetic permeability as Eq. (3.11) clearly shows. Only materials such as negative index materials (NIM) fulfil this condition as opposed to most materials which are non-magnetic. In order to derive the dispersion relation at the interface 1-2 (TM-polarized) in Fig. 3.2, Eqs. (3.12) and (3.13) are used to eliminate the k_z terms from Eq. (3.10) to produce Eq. (3.14) [59].

$$k_1^2 = k_x^2 + k_{z1}^2 = k_v^2 \epsilon_{r1} \quad (3.12)$$

$$k_2^2 = k_x^2 + k_{z2}^2 = k_v^2 \epsilon_{r2} \quad (3.13)$$

$$k_x = k_v \sqrt{\frac{\epsilon_{r1} \epsilon_{r2}}{\epsilon_{r1} + \epsilon_{r2}}} \quad (3.14)$$

In order for SPs to exist, k_z has to be imaginary which occurs when k_x is real and greater than k_v . If $\epsilon_{r2} = 1$ (vacuum), then those conditions are only satisfied when $\epsilon_{r1} < -1$ [61].

3.1.3 Solution to the Stochastic Maxwell Equations

In this section, we derive an expression for the time-averaged Poynting vector (heat flux) by solving the stochastic Maxwell equations based on the fluctuational electrodynamics (FE) formalism. The brief derivation presented here is based on the work done by Francoeur et al. [25]. For more details the reader is referred to [25,66]. We first list the stochastic Maxwell equations that are to be solved in order to obtain the electric and magnetic field equations [25]:

$$\nabla \times \mathbf{E}(\mathbf{r}, \omega) = i\omega \mathbf{B}(\mathbf{r}, \omega) \quad (3.15)$$

$$\nabla \times \mathbf{H}(\mathbf{r}, \omega) = -i\omega \varepsilon \mathbf{E}(\mathbf{r}, \omega) + \mathbf{J}^r(\mathbf{r}, \omega) \quad (3.16)$$

$$\nabla \cdot \mathbf{D}(\mathbf{r}, \omega) = \nabla \cdot (\hat{\varepsilon} \mathbf{E}(\mathbf{r}, \omega)) = \rho_e \quad (3.17)$$

$$\nabla \cdot \mathbf{B}(\mathbf{r}, \omega) = \nabla \cdot (\mu_0 \mathbf{H}(\mathbf{r}, \omega)) = 0 \quad (3.18)$$

The term \mathbf{J}^r refers to the randomly fluctuating current density that causes thermal fluctuations of the field [67]. Due to its random nature, the Maxwell equations in turn become stochastic. In order to solve for the electric field, the magnetic induction, \mathbf{B} is written as a function of the magnetic vector potential: $\mathbf{B}(\mathbf{r}, \omega) = \nabla \times \mathbf{A}(\mathbf{r}, \omega)$ and is then substituted into Eq. (3.15) (Faraday's law) along with the vector identity $\nabla \times (\nabla \Phi_e) = 0$ to produce [25]:

$$\mathbf{E}(\mathbf{r}, \omega) = i\omega \mathbf{A}(\mathbf{r}, \omega) - \nabla \Phi_e(\mathbf{r}, \omega) \quad (3.19)$$

where Φ_e is the electric scalar potential. The relationship between \mathbf{A} and Φ_e is given by the Lorentz gauge [66]:

$$\nabla \cdot \mathbf{A}(\mathbf{r}, \omega) = i\omega \varepsilon \mu_0 \Phi_e(\mathbf{r}, \omega) \quad (3.20)$$

\mathbf{A} is then written as a function of the stochastic current density, \mathbf{J}^r and the Green's function, g resulting in Eq. (3.21) where \mathbf{r} is a field point and \mathbf{r}' represents a source point [25].

$$\mathbf{A}(\mathbf{r}, \omega) = \mu_0 \int_V \mathbf{J}^r(\mathbf{r}', \omega) g(\mathbf{r}, \mathbf{r}', \omega) dV' \quad (3.21)$$

Equations (3.20) and (3.21) are substituted into Eq. (3.19) in order to obtain a relation for \mathbf{E} in terms of the Green's functions. The solutions for all three orthogonal directions are combined to form Eq. (3.22) while the magnetic field, \mathbf{H} (Eq. (3.23)) is found by using Eq. (3.18) (Gauss's law) [68,69].

$$\mathbf{E}(\mathbf{r}, \mathbf{r}', \omega) = i\omega \mu_0 \int_V dV' \overline{\overline{\mathbf{G}}}^e(\mathbf{r}, \mathbf{r}', \omega) \cdot \mathbf{J}^r(\mathbf{r}', \omega) \quad (3.22)$$

$$\mathbf{H}(\mathbf{r}, \mathbf{r}', \omega) = \int_V dV' \overline{\overline{\mathbf{G}}}^m(\mathbf{r}, \mathbf{r}', \omega) \cdot \mathbf{J}^r(\mathbf{r}', \omega) \quad (3.23)$$

Both \mathbf{E} and \mathbf{H} are written in terms of the dyadic Green's functions (DGF). The electric dyadic Green's function is represented as [66,69]:

$$\overline{\overline{\mathbf{G}}}^e(\mathbf{r}, \mathbf{r}', \omega) = g(\mathbf{r}, \mathbf{r}', \omega) \left[\overline{\overline{\mathbf{I}}} + \frac{1}{k^2} \nabla \nabla \right] \quad (3.24)$$

while the magnetic Green's function is written as [66,69]:

$$\overline{\overline{\mathbf{G}}}^m(\mathbf{r}, \mathbf{r}', \omega) = \nabla \times \left(g(\mathbf{r}, \mathbf{r}', \omega) \overline{\overline{\mathbf{I}}} \right) \quad (3.25)$$

where $\overline{\overline{\mathbf{I}}}$ is the dyadic or idem factor [68]. The radiative heat flux between two bodies is then expressed as the time-averaged Poynting vector which is written in terms of the electric and magnetic fields [58,70]:

$$\langle \mathbf{S}(\mathbf{r}, \omega) \rangle = 2 \operatorname{Re} \left\langle \mathbf{E}(\mathbf{r}, \omega) \times \mathbf{H}^*(\mathbf{r}, \omega) \right\rangle \quad (3.26)$$

Substituting Eqs. (3.24) and (3.25) into Eq. (3.26) yields [25]:

$$\langle \mathbf{S}(\mathbf{r}, \omega) \rangle = 2 \operatorname{Re} \left\{ i \omega \mu_0 \int_V dV' \int_V dV'' \begin{bmatrix} \hat{\mathbf{x}}(G_{yn}^e G_{zj}^{m*} - G_{zn}^e G_{yj}^{m*}) \\ + \hat{\mathbf{y}}(G_{zn}^e G_{xj}^{m*} - G_{xn}^e G_{zj}^{m*}) \\ + \hat{\mathbf{z}}(G_{xn}^e G_{yj}^{m*} - G_{yn}^e G_{xj}^{m*}) \end{bmatrix} \left\langle J_n^r(\mathbf{r}', \omega) J_j^{r*}(\mathbf{r}'', \omega) \right\rangle \right\} \quad (3.27)$$

The fluctuational dissipation theorem (FDT) is employed to solve for the spectral density of the current fluctuations and is written as [25]:

$$\langle J_n^r(\mathbf{r}', \omega) J_j^{r*}(\mathbf{r}'', \omega) \rangle = \frac{\omega \varepsilon_0}{\pi} \operatorname{Im} \{ \varepsilon_r(\omega) \} \Theta(\omega, T) \delta_{nj} \delta(\mathbf{r}' - \mathbf{r}'') \quad (3.28)$$

There are several assumptions that accompany the use of the FDT. Firstly, and probably most importantly, the bodies involved in the radiative heat transfer are assumed to be in local thermodynamic equilibrium at an equilibrium temperature, T . Next, the media involved are assumed to be isotropic, non-magnetic and described by a local frequency-dependent dielectric function [25]. The second assumption is valid for vacuum gap distances greater than the atomic lattice constant. At distances smaller than that, non-local effects become more significant [71] and the formalism breaks down. Equation (3.28) is then substituted into Eq. (3.27) in order to obtain a general relation for the radiative heat flux [25]:

$$\langle \mathbf{S}(\mathbf{r}, \omega) \rangle = \frac{2\varepsilon_0\mu_0\omega^2}{\pi} \text{Re} \left\{ i \int_V dV' \int_V dV'' \begin{bmatrix} \hat{\mathbf{x}}(G_{yn}^e G_{zj}^{m*} - G_{zn}^e G_{yj}^{m*}) \\ + \hat{\mathbf{y}}(G_{zn}^e G_{xj}^{m*} - G_{xn}^e G_{zj}^{m*}) \\ + \hat{\mathbf{z}}(G_{xn}^e G_{yj}^{m*} - G_{yn}^e G_{xj}^{m*}) \end{bmatrix} \text{Im}\{\varepsilon_r(\omega)\} \Theta(\omega, T) \delta_{ij} \delta(\mathbf{r}' - \mathbf{r}'') \right\} \quad (3.29)$$

where the subscripts n and j refer to the summation over the three orthogonal components for the electric field vector and magnetic field vector respectively [25].

3.2 PV Cell

3.2.1 The p - n Junction

A PV cell is a semiconductor device that converts light or electromagnetic waves into electricity. It basically consists of a p -type region and an n -type region which form a p - n junction at their interface. The p -type region is doped with acceptor dopants such as boron (group III) which has fewer valence electrons than the intrinsic material. This results in an excess of free holes, i.e. the number of free holes exceeds the number of free electrons and thus, holes become the majority carriers while electrons are the minority carriers. In the n -type region the opposite is true. Donor dopants such as phosphorus (group V) with more valence electrons than the intrinsic material are used to generate more free electrons in the material. In this case, the majority carriers are electrons while minority carriers are holes. When these two layers are in contact, majority holes in the p -type region would diffuse towards the n -type region while majority electrons in the n -type region diffuse in the other direction. This diffusion process causes the acceptors in the p -type region to become negatively charged while donors in the n -type region become positively charged. This in turn produces an electric field at the junction

with a built-in voltage, V_0 . This electric field sweeps minority carriers from one region to the other, generating a drift current which opposes the diffusion current. The charged region (space charge region) will continue to expand until the drift current equals the diffusion current. And so at equilibrium, a charged region with a fixed width will be generated at the $p-n$ junction sandwiched by quasi-neutral regions. The charged region is also called the depletion region as all free carriers are swept away by the electric field, thus making the region depleted of free carriers. Without exposure to light, a PV cell behaves just like a diode. However, under illumination which exceeds the band-gap energy, electron-hole pairs (EHP) are excited in the material. The minority carrier density in both sides of the $p-n$ junction increases and as these photogenerated carriers get swept across the depletion region by the electric field, photocurrent is generated. When connected to a load, an illuminated PV cell would start producing electrical power.

3.2.2 Recombination of Electron-Hole Pairs

Recombination occurs when an electron drops from the conduction band into the valence band where it fills a valence band hole. This is the process by which the concentrations of carriers relax to their equilibrium values. There are three main recombination mechanisms that occur within the PV cell, namely Shockley-Read-Hall (SRH) recombination, Auger recombination and radiative recombination [72].

SRH recombination or recombination through defects (traps) occurs in semiconductors with impurities or defects in their crystal lattices. It involves a two-step process where an electron from the conduction band first relaxes to the energy level introduced by the trap within the band gap and subsequently relaxes to the valence band where it recombines with a hole [73]. The rate of SRH recombination depends on the location of the trap within the band gap. If the introduced energy level is closer to the conduction band edge, the trapped electron is more likely to get re-emitted into the conduction band. If, however, the energy level lies closer to the valence band, the ability of a trap to “capture” an electron suffers (the electron is required to release more energy), thus making it less likely for recombination to occur. Therefore, energy levels near the middle of the band gap serve as excellent recombination centres [74,75].

Auger recombination involves the transfer of energy from one electron which subsequently recombines, to another electron which then thermalizes back to the conduction band edge by transferring its energy to phonons. This form of recombination is the inverse process to impact ionization where a high energy electron generates an EHP by colliding with a crystal atom [72]. Auger recombination is dominant in heavily doped semiconductors or when the injection level is high.

Radiative recombination or band-to-band recombination involves the release of energy in the form of photons to bring about recombination. It is the inverse process to EHP generation through illumination. This recombination process occurs more prevalently in direct band-gap semiconductors such as gallium arsenide (GaAs). In indirect band-gap semiconductors the radiative recombination rate is really low and is often deemed negligible. Devices like light emitting diodes (LED) operate based on this form of recombination.

At the surfaces of semiconductors, the crystal lattice is abruptly terminated leaving a large number of dangling bonds which serve as recombination centres. Electrons and holes can recombine through them just as they do with traps. Surfaces are also more susceptible to impurities as they are exposed during the fabrication process, further increasing the likelihood of surface recombination [76]. A high surface recombination rate at the top surface of a PV cell greatly reduces the short-circuit current due to the fact that the region where most carriers are generated is near the top. One way to reduce the surface recombination rate is by adding a passivating layer on the surface which reduces the number of dangling bonds [77]. A material that is commonly used to passivate commercial solar cells is silicon nitride [78].

3.2.3 PV Cell Characterization

A common way to characterize PV cells is by determining the relationship between the electric current through the cell and the voltage across it, which is referred to as the current-voltage (J - V) characteristic. This relationship is used to define the cell's figures of merit or performance metrics such as the short-circuit current (J_{sc}), the open-circuit voltage (V_{oc}), the fill factor (FF), the maximum output power (P_m) and the conversion efficiency (η_c) [72]. When the applied voltage is low, the dark (diode/recombination) current is negligible and thus the net current is referred to as the short-circuit current. When the applied voltage is increased, the net current

decreases until it reaches zero, at which point the voltage is called the open-circuit voltage. The fill factor is a measure of the “squareness” of the J - V characteristic and is calculated as [72]:

$$FF = \frac{P_m}{V_{oc} J_{sc}} = \frac{V_{Pm} J_{Pm}}{V_{oc} J_{sc}} \quad (3.30)$$

where V_{Pm} and J_{Pm} are the voltage and current at the point that produces the maximum output power. An empirical expression for the fill factor is given as [75]:

$$FF = \frac{V_{oc} - \frac{kT}{e} \ln[eV_{oc}/kT + 0.72]}{V_{oc} + kT/e} \quad (3.31)$$

These figures of merit allow us to determine the properties of a high-performance PV cell. The goal here would be to maximize J_{sc} , V_{oc} and FF . The short-circuit current depends very much on the EHP generation rate and the collection probability, i.e. if the number of generated EHP is high and most of them reach the contacts before recombining, J_{sc} will be quite substantial [72]. V_{oc} on the other hand, is greatly affected by the dark current which in turn depends on the recombination rate. A low recombination rate will produce less dark current, allowing for a greater V_{oc} value. Increasing V_{oc} would subsequently increase the fill factor as evidenced by Eq. (3.31). Thus, it is clear that when designing high-performance PV cells, the recombination rates should be minimized and absorption of above-band-gap photons should be maximized [72].

3.3 Concluding Remarks

The fundamentals of near-field TPV systems have been discussed in this chapter. The mathematical description of a near-field TPV system basically involves only two components: the near-field thermal radiation problem and the photovoltaic effect that occurs in the TPV cell. The coupling of these two components would allow us to simulate the operation of such devices. For a more realistic simulation, a heat transport model is added to determine the evolution of the TPV cell temperature. These models are explored in detail in Chapter 4.

Chapter 4 Modelling and Simulation

The nano-gap TPV devices presented in this thesis are modelled as one-dimensional multi-layered systems as done in [34]. The dimensions along the x and y -axes are not considered as their geometries are infinitely wide compared to the thicknesses along the z -axis. In this system, multiple thin layers are sandwiched between two half-spaces which are assumed to be infinitely long. Each layer can be modelled as a different material allowing for multiple media to be simulated. The modelling of the device is divided into three main parts. The solution to the near-field thermal radiation problem is presented in Section 4.1. The modelling of the TPV cell operation (photovoltaic effect) is detailed in Section 4.2 and finally the heat transport models as applied to the TPV cell are described in Section 4.3.

4.1 Near-Field Thermal Radiation

In this section, expressions for the spectral radiative heat flux in the z -direction as a function of position are derived in terms of the Weyl components of the DGFs. In Section 4.1.1, the case of a radiating film is described followed by the case of a radiating bulk in Section 4.1.2.

The monochromatic radiative heat flux at point z_c in the z -direction is given as [26]:

$$q_\omega(z_c) = \langle S_z(z_c, \omega) \rangle = 2 \operatorname{Re} \left\{ E_x H_y^* - E_y H_x^* \right\} \quad (4.1)$$

where $\langle S_z(z_c, \omega) \rangle$ is the time-averaged Poynting vector in the z -direction and is represented in terms of the DGFs based on Eq. (3.29).

4.1.1 Film Radiator

Equation (4.1) is expanded and written in terms of the Weyl components of the DGFs. For the case of a film radiator, the monochromatic radiative heat flux expression becomes [26]:

$$q_{\omega,sl}(z_c) = \frac{k_v^2 \Theta(\omega, T_s)}{\pi^2} \operatorname{Re} \left\{ i \varepsilon_{rs}''(\omega) \int_0^\infty k_\rho dk_\rho \int_{z_s}^{z_{s+1}} dz' \left[\begin{array}{l} g_{sl\rho\rho}^E(k_\rho, z_c, z', \omega) g_{sl\theta\rho}^{H*}(k_\rho, z_c, z', \omega) \\ + g_{sl\rho z}^E(k_\rho, z_c, z', \omega) g_{sl\theta z}^{H*}(k_\rho, z_c, z', \omega) \\ - g_{sl\theta\theta}^E(k_\rho, z_c, z', \omega) g_{sl\rho\theta}^{H*}(k_\rho, z_c, z', \omega) \end{array} \right] \right\} \quad (4.2)$$

where the term $\Theta(\omega, T_s)$ is the mean energy of a Planck oscillator and can be found using $\hbar\omega/(e^{\hbar\omega/k_bT} - 1)$. The subscript s refers to the source layer i.e. the radiating layer and l refers to the layer where the radiative heat flux is calculated at a specific point z_c as depicted in Fig. 4.1. An integration is performed over the entire thickness of the film radiator in terms of each source point, z' to obtain the radiative heat flux contribution from the entire film radiator. The term g is the Weyl component of the DGFs and is written in terms of the forward and backward wave amplitudes (Eqs. (4.3) to (4.11)) [26]. A polar coordinate system is used which explains the use of the symbols ρ and θ to represent the radial and angular coordinates at each point along the z -axis.

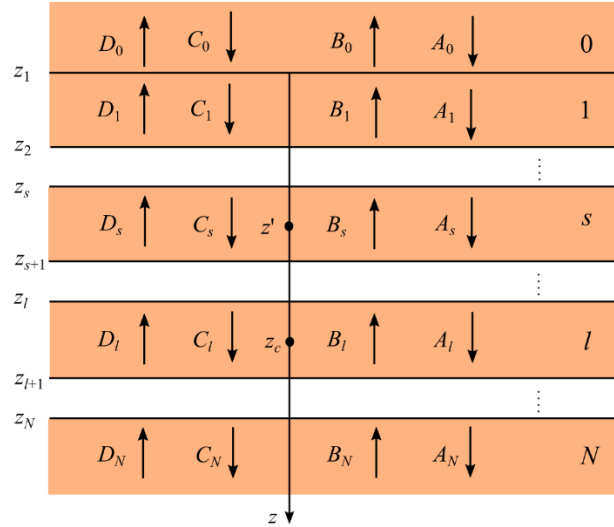


Fig. 4.1 Schematic diagram of a one-dimensional multi-layered system. Forward (A and B) and backward (C and D) wave amplitudes are depicted in each layer.

$$g_{sl\rho\rho}^E(k_\rho, z_c, z', \omega) = \frac{ik_{z_l}}{2k_s k_l} \left(\begin{array}{l} A_l^{TM} e^{i[k_{z_l}(z_c - z_l) - k_{z_s} z']} - B_l^{TM} e^{i[-k_{z_l}(z_c - z_l) - k_{z_s} z']} \\ - C_l^{TM} e^{i[k_{z_l}(z_c - z_l) + k_{z_s} z']} + D_l^{TM} e^{i[-k_{z_l}(z_c - z_l) + k_{z_s} z']} \end{array} \right) \quad (4.3)$$

$$\mathbf{g}_{sl\rho z}^E(k_\rho, z_c, z', \omega) = \frac{ik_{z_l}k_\rho}{2k_{z_s}k_s k_l} \begin{pmatrix} -A_l^{TM} e^{i[k_{z_l}(z_c-z_l)-k_{z_s}z']} + B_l^{TM} e^{i[-k_{z_l}(z_c-z_l)-k_{z_s}z']} \\ -C_l^{TM} e^{i[k_{z_l}(z_c-z_l)+k_{z_s}z']} + D_l^{TM} e^{i[-k_{z_l}(z_c-z_l)+k_{z_s}z']} \end{pmatrix} \quad (4.4)$$

$$\mathbf{g}_{sl\theta\theta}^E(k_\rho, z_c, z', \omega) = \frac{i}{2k_{z_s}} \begin{pmatrix} A_l^{TE} e^{i[k_{z_l}(z_c-z_l)-k_{z_s}z']} + B_l^{TE} e^{i[-k_{z_l}(z_c-z_l)-k_{z_s}z']} \\ + C_l^{TE} e^{i[k_{z_l}(z_c-z_l)+k_{z_s}z']} + D_l^{TE} e^{i[-k_{z_l}(z_c-z_l)+k_{z_s}z']} \end{pmatrix} \quad (4.5)$$

$$\mathbf{g}_{slz\rho}^E(k_\rho, z_c, z', \omega) = \frac{ik_\rho}{2k_s k_l} \begin{pmatrix} -A_l^{TM} e^{i[k_{z_l}(z_c-z_l)-k_{z_s}z']} - B_l^{TM} e^{i[-k_{z_l}(z_c-z_l)-k_{z_s}z']} \\ + C_l^{TM} e^{i[k_{z_l}(z_c-z_l)+k_{z_s}z']} + D_l^{TM} e^{i[-k_{z_l}(z_c-z_l)+k_{z_s}z']} \end{pmatrix} \quad (4.6)$$

$$\mathbf{g}_{slzz}^E(k_\rho, z_c, z', \omega) = \frac{ik_\rho^2}{2k_{z_s}k_s k_l} \begin{pmatrix} A_l^{TM} e^{i[k_{z_l}(z_c-z_l)-k_{z_s}z']} + B_l^{TM} e^{i[-k_{z_l}(z_c-z_l)-k_{z_s}z']} \\ + C_l^{TM} e^{i[k_{z_l}(z_c-z_l)+k_{z_s}z']} + D_l^{TM} e^{i[-k_{z_l}(z_c-z_l)+k_{z_s}z']} \end{pmatrix} \quad (4.7)$$

$$\mathbf{g}_{sl\rho\theta}^H(k_\rho, z_c, z', \omega) = \frac{k_{z_l}}{2k_{z_s}} \begin{pmatrix} A_l^{TE} e^{i[k_{z_l}(z_c-z_l)-k_{z_s}z']} - B_l^{TE} e^{i[-k_{z_l}(z_c-z_l)-k_{z_s}z']} \\ + C_l^{TE} e^{i[k_{z_l}(z_c-z_l)+k_{z_s}z']} - D_l^{TE} e^{i[-k_{z_l}(z_c-z_l)+k_{z_s}z']} \end{pmatrix} \quad (4.8)$$

$$\mathbf{g}_{sl\theta\rho}^H(k_\rho, z_c, z', \omega) = \frac{k_l}{2k_s} \begin{pmatrix} -A_l^{TM} e^{i[k_{z_l}(z_c-z_l)-k_{z_s}z']} - B_l^{TM} e^{i[-k_{z_l}(z_c-z_l)-k_{z_s}z']} \\ + C_l^{TM} e^{i[k_{z_l}(z_c-z_l)+k_{z_s}z']} + D_l^{TM} e^{i[-k_{z_l}(z_c-z_l)+k_{z_s}z']} \end{pmatrix} \quad (4.9)$$

$$\mathbf{g}_{slz\theta}^H(k_\rho, z_c, z', \omega) = \frac{k_l k_\rho}{2k_s k_{z_s}} \begin{pmatrix} A_l^{TM} e^{i[k_{z_l}(z_c-z_l)-k_{z_s}z']} + B_l^{TM} e^{i[-k_{z_l}(z_c-z_l)-k_{z_s}z']} \\ + C_l^{TM} e^{i[k_{z_l}(z_c-z_l)+k_{z_s}z']} + D_l^{TM} e^{i[-k_{z_l}(z_c-z_l)+k_{z_s}z']} \end{pmatrix} \quad (4.10)$$

$$\mathbf{g}_{slz\theta}^H(k_\rho, z_c, z', \omega) = \frac{k_\rho}{2k_{z_s}} \begin{pmatrix} -A_l^{TE} e^{i[k_{z_l}(z_c-z_l)-k_{z_s}z']} - B_l^{TE} e^{i[-k_{z_l}(z_c-z_l)-k_{z_s}z']} \\ -C_l^{TE} e^{i[k_{z_l}(z_c-z_l)+k_{z_s}z']} - D_l^{TE} e^{i[-k_{z_l}(z_c-z_l)+k_{z_s}z']} \end{pmatrix} \quad (4.11)$$

In order to solve for the Weyl components of the DGFs, the wave amplitudes need to be obtained first. For the case of a radiating film, A_0 , B_N , C_0 and D_N equal to zero due to the assumption that no waves are entering the system from the outside i.e. we only consider waves emitted by and travelling within the layers of the multi-layered media. The wave amplitudes in the layer s and the two half-spaces 0 and N can be found using Eqs. (4.12) to (4.19) [26]. The terms S^+ and S^- are the amplitudes of the source at point z_s in the forward and backward directions respectively and are found using Eqs. (4.20) and (4.21). The terms S_{11} , S_{12} , S_{21} and S_{22} are elements of scattering matrices of each layer relative to another layer and are calculated recursively. The solution to the scattering matrices are detailed in [26].

$$B_s = \frac{S_{21}(s, N)S^+}{1 - S_{21}(s, N)S_{12}(0, s)} \quad (4.12)$$

$$A_s = S_{12}(0, s)B_s \quad (4.13)$$

$$B_0 = S_{22}(0, s)B_s \quad (4.14)$$

$$A_N = S_{11}(s, N)(A_s + S^+) \quad (4.15)$$

$$C_s = \frac{S_{12}(0, s)S^-}{1 - S_{12}(0, s)S_{21}(s, N)} \quad (4.16)$$

$$D_s = S_{21}(s, N)C_s \quad (4.17)$$

$$C_N = S_{11}(s, N)C_s \quad (4.18)$$

$$D_0 = S_{22}(0, s)(D_s + S^-) \quad (4.19)$$

$$S^+ = e^{ik_{zs}(z_s - z')} \quad (4.20)$$

$$S^- = e^{ik_{zs}(z' - z_s)} \quad (4.21)$$

For $z < z'$, the wave amplitudes in layer $l = 1, \dots, s-1$ can be calculated using [26]:

$$B_l = \frac{B_0}{S_{22}(0, l)} \quad (4.22)$$

$$A_l = S_{12}(0, l)B_l \quad (4.23)$$

$$D_l = \frac{D_0}{S_{22}(0, l)} \quad (4.24)$$

$$C_l = S_{12}(0, l)D_l \quad (4.25)$$

For $z > z'$, the wave amplitudes in layer $l = s+1, \dots, N-1$ are given by [26]:

$$B_l = \frac{B_s - S_{21}(s, l)(A_s + S^+)}{S_{22}(s, l)} \quad (4.26)$$

$$A_l = S_{11}(s, l)(A_s + S^+) + S_{12}(s, l)B_l \quad (4.27)$$

$$D_l = \frac{D_s - S_{21}(s, l)C_s}{S_{22}(s, l)} \quad (4.28)$$

$$C_l = S_{11}(s, l)C_s + S_{12}(s, l)D_l \quad (4.29)$$

4.1.2 Bulk Radiator

The monochromatic radiative heat flux exchanged between a bulk radiator (layer 0) and a point of interest is given as [26]:

$$q_{\omega,0l}(z_c) = \frac{k_v^2 \Theta(\omega, T_s)}{2\pi^2} \operatorname{Re} \left\{ i \varepsilon_{r0}''(\omega) \int_0^\infty \frac{k_\rho dk_\rho}{k_{z0}''} \left[\begin{array}{l} g_{0l\rho\rho}^E(k_\rho, z_c, \omega) g_{0l\theta\rho}^{H*}(k_\rho, z_c, \omega) \\ + g_{0l\rho z}^E(k_\rho, z_c, \omega) g_{0l\theta z}^{H*}(k_\rho, z_c, \omega) \\ - g_{0l\theta\theta}^E(k_\rho, z_c, \omega) g_{0l\rho\theta}^{H*}(k_\rho, z_c, \omega) \end{array} \right] \right\} \quad (4.30)$$

where z' is factored out from the Weyl components and integrated analytically from $z_s = -\infty$ to $z_{s+1} = 0$ [26]. The wave amplitudes C and D for each layer are zero due to the fact that there are no waves emitted in the backward direction by the half-space 0 that travel within the system. Thus we are only left with the forward wave amplitudes which can be obtained using Eqs. (4.31) to (4.34) [26].

$$A_N = S_{11}(0, N) \quad (4.31)$$

$$B_0 = S_{21}(0, N) \quad (4.32)$$

$$B_l = \frac{B_0 - S_{21}(0, l)}{S_{22}(0, l)} \quad (4.33)$$

$$A_l = S_{11}(0, l) + S_{12}(0, l) B_l \quad (4.34)$$

4.1.3 Analytical Expression in terms of Reflection and Transmission Coefficients

Having an analytical expression for the radiative heat flux enables us to have a more intuitive understanding of how each layer affects the heat flux. Thus, in this sub-section, we present a general analytical expression for the monochromatic radiative heat flux from a multi-layered radiator, calculated at the top surface of a multi-layered receiver in terms of reflection and transmission coefficients. The expressions for the propagating and evanescent components are [26,79,80]:

$$q_{\omega}^{prop}(z_{m_{rec}}) = \frac{\Theta(\omega, T_{rad})}{4\pi^2} \int_0^{k_y} k_{\rho} dk_{\rho} \sum_{\gamma=TE, TM} \frac{(1 - |R_{n_{rad}}^{\gamma}|^2 - |T_{n_{rad}}^{\gamma}|^2)(1 - |R_{m_{rec}}^{\gamma}|^2)}{|1 - R_{n_{rad}}^{\gamma} R_{m_{rec}}^{\gamma} e^{2ik_{zn_{rad}+1}d_{gap}}|^2} \quad (4.35)$$

$$q_{\omega}^{evan}(z_{m_{rec}}) = \frac{\Theta(\omega, T_{rad})}{\pi^2} \int_{k_y}^{\infty} k_{\rho} dk_{\rho} e^{-2k_{zn_{rad}+1}d_{gap}} \sum_{\gamma=TE, TM} \frac{\text{Im}(R_{n_{rad}}^{\gamma})\text{Im}(R_{m_{rec}}^{\gamma})}{|1 - R_{n_{rad}}^{\gamma} R_{m_{rec}}^{\gamma} e^{-2k_{zn_{rad}+1}d_{gap}}|^2} \quad (4.36)$$

where n_{rad} is the radiator layer adjacent to the vacuum gap layer and m_{rec} is the receiver layer adjacent to that same vacuum gap layer as shown in Fig. 4.2.

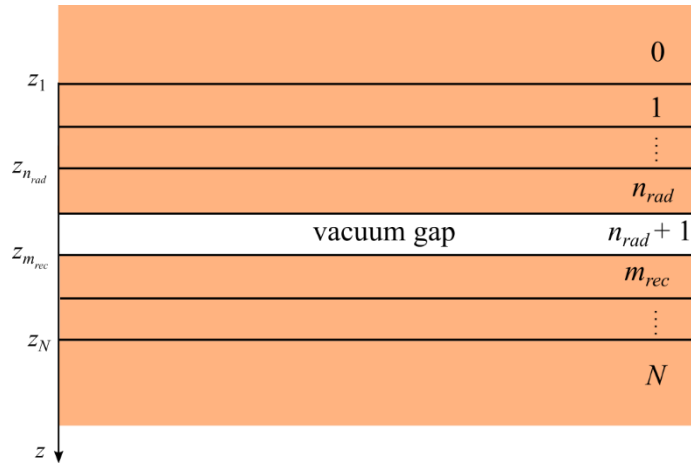


Fig. 4.2 Schematic diagram of the radiator and receiver layers.

Do note that layers 0 and N are bulk layers i.e. the layer thickness, $t \rightarrow \infty$. If the system consists of only two bulks exchanging radiative energy, the transmission coefficients are omitted from the expressions. The general expressions for the reflection and transmission coefficients in a multi-layered radiator configuration are [79]:

$$R_n^{\gamma} = \frac{r_{n+1,n}^{\gamma} + R_{n-1}^{\gamma} e^{2ik_{zn}t_n}}{1 + r_{n+1,n}^{\gamma} R_{n-1}^{\gamma} e^{2ik_{zn}t_n}} \quad (4.37)$$

$$T_n^{\gamma} = \frac{t_{n+1,n}^{\gamma} T_{n-1}^{\gamma} e^{2ik_{zn}t_n}}{1 + r_{n+1,n}^{\gamma} R_{n-1}^{\gamma} e^{2ik_{zn}t_n}} \quad n = n_{rad}, \dots, 1 \quad (4.38)$$

where R_0^{γ} and T_0^{γ} would just be $r_{1,0}^{\gamma}$ and $t_{1,0}^{\gamma}$ respectively. The general reflection coefficient in a multi-layered receiver is [79]:

$$R_m^\gamma = \frac{r_{m-1,m}^\gamma + R_{m+1}^\gamma e^{2ik_{zm}t_m}}{1 + r_{m-1,m}^\gamma R_{m+1}^\gamma e^{2ik_{zm}t_m}} \quad m = N-1, \dots, m_{rec} \quad (4.39)$$

where R_N^γ would be reduced to $r_{N-1,N}^\gamma$. The Fresnel reflection and transmission coefficients, r and t are taken from [65].

4.2 Photovoltaic Cell Model

The TPV cell is modelled as a p - n junction that consists of a p -type region on top of an n -type region as shown in Fig. 4.3 where it is discretized into nodes which represent control volumes. Grid A is the main grid where important values such as the excess minority carrier concentration and temperature are determined. Grid B is used to calculate the amount of heat flux absorbed in each control volume surrounding the nodes on grid A. In order to calculate the concentration of excess minority carriers—which is necessary for generating the J - V characteristic—the transport of holes and electrons in the TPV cell need to be modelled using the semiconductor equations which consist of Poisson's equation (Eq. (4.40)), the continuity equations (Eqs. (4.41) and (4.42)) and the current density equations (Eqs. (4.43) and (4.44)) [72]. In a uniformly-doped non-degenerate TPV cell at steady-state, the semiconductor equations can be reduced to Eqs. (4.45) and (4.46) [72].

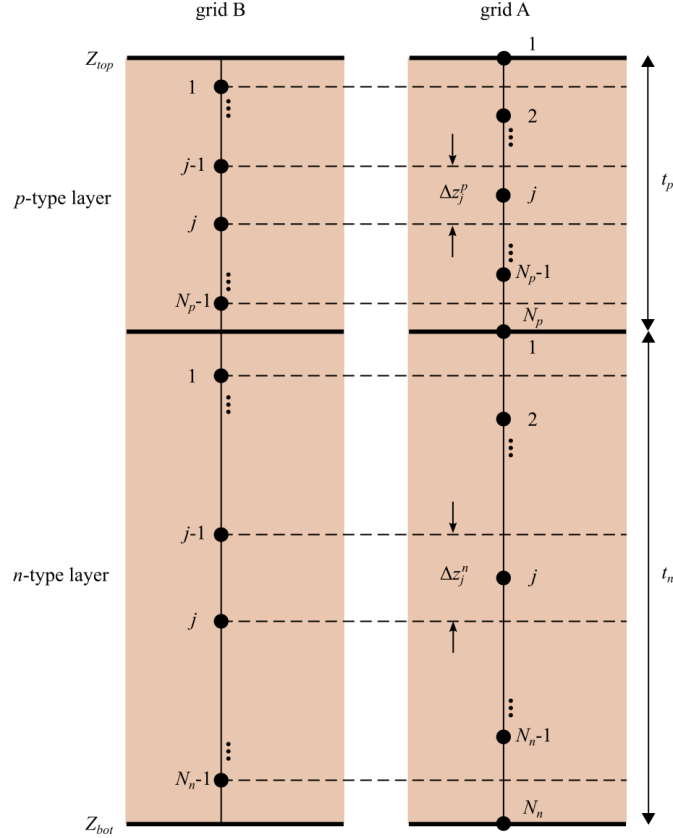


Fig. 4.3 Discretization of the TPV cell.

$$\nabla \cdot \epsilon \mathbf{E} = e(n_h - n_e + N) \quad (4.40)$$

$$\nabla \cdot \mathbf{J}_h = e \left(G - R_h - \frac{\partial n_h}{\partial t} \right) \quad (4.41)$$

$$\nabla \cdot \mathbf{J}_e = e \left(G - R_e - \frac{\partial n_e}{\partial t} \right) \quad (4.42)$$

$$\mathbf{J}_h = e\mu_h n_h \mathbf{E} + eD_h \nabla n_h \quad (4.43)$$

$$\mathbf{J}_e = e\mu_e n_e \mathbf{E} - eD_e \nabla n_e \quad (4.44)$$

$$e\mu_h \frac{d}{dz} (n_h \mathbf{E}) - eD_h \frac{d^2 n_h}{dz^2} = e(G - R) \quad (4.45)$$

$$e\mu_e \frac{d}{dz} (n_e \mathbf{E}) - eD_e \frac{d^2 n_e}{dz^2} = e(R - G) \quad (4.46)$$

The depletion-region approximation is utilised in this thesis to simplify the drift-diffusion equations. It is assumed that the regions outside the depletion-region are quasi-neutral and are under low-level injection causing the influence of the electric field to be negligible, thus the drift term in the drift-diffusion equations (Eqs. (4.45) and (4.46)) is neglected reducing them

to Eq. (4.47) [72]. The recombination rate, R is calculated as $\Delta n_{(e,h)}/\tau_{(e,h)}$. The EHP generation rate, G is rewritten as g_ω .

$$D_{(e,h)} \frac{d^2 \Delta n_{(e,h),\omega}(z)}{dz^2} - \frac{\Delta n_{(e,h),\omega}(z)}{\tau_{(e,h)}} + g_\omega(z) = 0 \quad (4.47)$$

$$g_{j,\omega} = \frac{q_{\omega,\Delta z_j^{(p,n)}}^{abs}}{\hbar \omega \Delta z_j^{(p,n)}} \quad (4.48)$$

$q_{\omega,\Delta z_j^{(p,n)}}^{abs}$ is calculated by subtracting the heat flux value at the bottom boundary of a control volume, Δz_j from the heat flux value at the top boundary or more specifically the absorbed heat flux in the control volume surrounding node j of grid A is determined from the difference between the heat fluxes at nodes $j-1$ and j of grid B. It is then used to calculate the EHP generation rate using Eq. (4.48). The minority carrier diffusion equation (MCDE) (Eq. (4.47)) is then applied to each node and discretized while taking into account the boundary conditions expressed by Eqs. (4.49) and (4.50) in order to solve for the spectral excess minority carrier concentration, $\Delta n_{(e,h),\omega}$ where $Z_{dp}^{(p,n)}$ is the top and bottom boundaries of the depletion-region. When solving for $\Delta n_{(e,h),\omega}$ in dark conditions, Eq. (4.50) is replaced by Eq. (4.51) where the equilibrium minority carrier concentrations are calculated as $n_{(e,h)0} = n_i^2 / N_{(a,d)}$. The resulting matrices are solved using the Thomas algorithm [81]. The total spectral photocurrent is calculated as the sum of Eqs. (4.52) to (4.54) [82] which when integrated over all frequencies gives the total photocurrent, J_{ph} generated. The J - V characteristic is generated using $J(V) = J_{ph} - J_0(V)$ where J_0 is the dark current found by solving Eq. (4.47) in dark conditions and V_f is the forward bias. The dark current represents the diffusion of electrons and holes across the junction—which eventually recombine (dark current is also called recombination current)—when bias is applied to the cell. It opposes the photocurrent, causing the net current to decrease until it reaches zero as the forward bias approaches the open-circuit voltage. The depletion-region width in the p and n -type regions are calculated using Eq. (4.55) [83] where ϵ_s is the static dielectric function and V_0 is the built-in voltage (equilibrium potential) across the depletion-region written as Eq. (4.56). The portion of the depletion-region width in the p -type region is measured from the boundary delineating the two doped regions and the same goes for the portion in the n -type region.

$$D_{(e,h)} \frac{d\Delta n_{(e,h),\omega}(Z_{top,bot})}{dz} = S_{(e,h)} \Delta n_{(e,h),\omega}(Z_{top,bot}) \quad (4.49)$$

$$\Delta n_{(e,h),\omega}(Z_{dp}^{(p,n)}) = 0 \quad (4.50)$$

$$\Delta n_{(e,h),\omega}(Z_{dp}^{(p,n)}) = n_{(e,h)0} \exp\left(\frac{eV_f}{k_b T_{cell}}\right) \quad (4.51)$$

$$J_{dp,\omega} = e \int_{Z_{dp}^p}^{Z_{dp}^n} g_{j,\omega} dz \quad (4.52)$$

$$J_{e,\omega} = eD_e \frac{d\Delta n_{e,\omega}(Z_{dp}^p)}{dz} \quad (4.53)$$

$$J_{h,\omega} = -eD_h \frac{d\Delta n_{h,\omega}(Z_{dp}^n)}{dz} \quad (4.54)$$

$$L_{dp}^{p,n} = \left[\frac{2\epsilon_s}{e} V_0 \left(\frac{N_{d,a}}{N_{a,d}(N_{a,d} + N_{d,a})} \right) \right]^{1/2} \quad (4.55)$$

$$V_0 = \left(\frac{k_b T_{cell}}{e} \right) \ln \left(\frac{N_a N_d}{n_i^2} \right) \quad (4.56)$$

The intrinsic carrier concentration, n_i is calculated as $n_i = (N_c N_v)^{0.5} e^{\frac{-E_g}{2k_b T_{cell}}}$ [84] where N_c and N_v are the effective density of states in the conduction and valence band respectively. The conversion efficiency of the nano-gap TPV device is calculated as the ratio of the maximum electrical power produced and the total radiative heat flux absorbed by the TPV cell:

$$\eta_c = 100\% \times \frac{P_m}{P_{abs}} \quad (4.57)$$

We are aware that when calculating the conversion efficiency for solar cells, the total radiative heat flux on the top surface of the cell (not merely what is absorbed) is often used as the denominator. However, that definition is only useful if the radiation is entirely propagating and is therefore incident on the cell surface which is not the case in this thesis. We retain the current definition of the conversion efficiency (Eq. (4.57)) as we deem it to be more useful and consistent with the literature [33,34].

4.3 Heat Transport Model

Here we present two ways to model heat transport in the TPV cell. The first uses Fourier's law while the second employs the phonon Monte Carlo (MC) simulation method to solve for the temperature profile in the cell.

The Fourier law depicts the relationship between the heat flux due to thermal conduction and the temperature gradient. It accurately describes the diffusive regime of heat transport but breaks down when object dimensions become comparable to the phonon mean free path. At such length scales, the transport of heat transitions into the semi-ballistic or ballistic regimes where scattering events (e.g. phonon-phonon scattering) need to be modelled explicitly; a procedure that the Fourier law is incapable of accomplishing. This leads us to the other method for modelling heat transport: the phonon Monte Carlo simulation which is capable of modelling the behaviour of phonons at the microscopic level. It takes into account the events that occur within the phonons' relaxation times, thus, allowing it to simulate semi-ballistic or ballistic transport. Furthermore, the MC simulation does not assume a single thermal conductivity value but calculates it statistically based on the distribution of phonons. In spite of all these, there is one major drawback to such simulation methods: the long computation times. Hence, it is usually only used for microscale or nanoscale applications.

In this thesis, both methods are used depending on the application. The Fourier law is used when the cell thickness is greater than the mean free path of phonons and a constant bulk thermal conductivity is assumed. The MC simulation on the other hand, is employed when studying the thermal conduction in thin films. In Chapter 7, we compare the two methods by implementing them at the same length scales and conditions.

4.3.1 Fourier's Law

Heat transport as described by Fourier's law is represented as Eq. (4.58). The top surface of the cell, Z_{top} is assumed to be insulated, thus the boundary condition is expressed as Eq. (4.59) where the second term on the left represents surface recombination. It is assumed that the bottom surface, Z_{bot} is exposed to convective cooling, thus Eq. (4.60) is used as the boundary condition where h_{conv} and T_{∞} are the heat transfer coefficient and the temperature of the cooling

liquid respectively. As done with the MCDE, the Fourier law equation is discretised into a system of linear equations and the Thomas algorithm is employed to solve for the temperature at each node.

$$k_{cond} \frac{d^2 T_{cell}(z)}{dz^2} + Q(z) = 0 \quad (4.58)$$

$$-k_{cond} \frac{dT_{cell}(Z_{top})}{dz} + S_e e E_g \int_{\omega_g}^{\infty} \Delta n_{(e,h),\omega}(Z_{top}) d\omega = 0 \quad (4.59)$$

$$-k_{cond} \frac{dT_{cell}(Z_{bot})}{dz} = h_{conv} [T_{cell}(Z_{bot}) - T_{\infty}] - S_h e E_g \int_{\omega_g}^{\infty} \Delta n_{(e,h),\omega}(Z_{bot}) d\omega \quad (4.60)$$

4.3.2 Phonon Monte Carlo Simulation

The phonon MC simulation is a statistical approach which relies on random sampling to simulate the behaviour of phonons as a means of solving the Boltzmann transport equation (BTE) (Eq. (4.61)). The MC simulation used in this thesis is based on the work done in [85] and [86] and is summed up in the flowchart of Fig. 4.4.

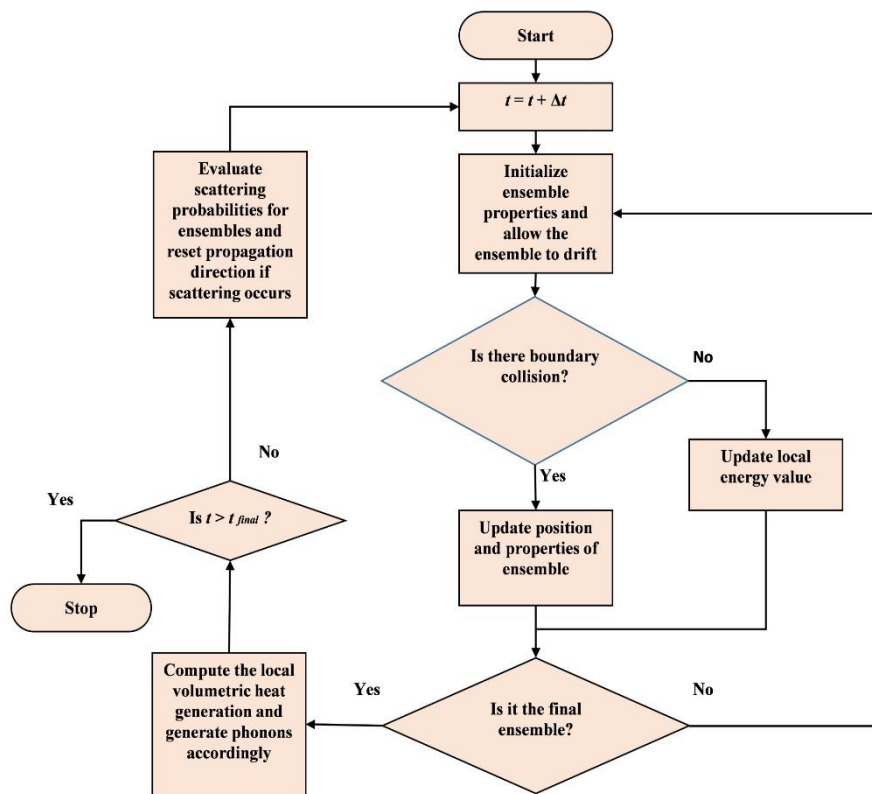


Fig. 4.4 Flow chart of the MC simulation for phonon transport [85].

The pseudo-temperature of each control volume in the TPV cell is calculated using Eq. (4.62) and is used to generate the temperature profile in the TPV cell. The phonon creation scheme due to local heat generation is based on Eq. (4.63) where Q_{gen} is the amount of heat energy generated in each control volume and is obtained by multiplying the total volumetric heat generation term, $Q_{tot}(z)$ with the control volume and simulation time step. The phonon creation process will cease once Eq. (4.63) is satisfied.

$$\frac{\partial f}{\partial t} + \bar{v}_{\bar{k}} \cdot \nabla_{\bar{r}} f + \dot{\bar{k}} \cdot \nabla_{\bar{k}} f = \left(\frac{\partial f}{\partial t} \right)_{col} \quad (4.61)$$

$$\sum_{pl} \sum_{i=1}^{N_b} \hbar \omega_i [f_0(\omega_i, T_{pseudo}) - f_0(\omega_i, T_{ref})] \times D_i(\omega_i, pl) \Delta \omega_i = \frac{E(x, y, z)}{\Delta x \Delta y \Delta z} \quad (4.62)$$

$$\sum_{i=1}^{N_{ph}} \hbar \omega_i = Q_{gen} \quad (4.63)$$

In the implementation of convective cooling in the MC simulation, the convective heat flux is calculated as, $q_{conv} = h_{\infty}(T_{final\ node} - T_{\infty})$ where $T_{final\ node}$ is the temperature at the bottom surface of the TPV cell. When this value is multiplied by the cross-sectional area and simulation time step, the convective energy is obtained which acts as a threshold for the phonon destruction scheme. To be more precise, phonons that collide with the bottom boundary will be destroyed if their energy exceeds the threshold value, thus simulating the cooling of a TPV cell. If however, the phonon energy is lower than the threshold, the boundary becomes adiabatic, reflecting the phonon back into the cell. It has to be noted that q_{conv} is constantly updated with every new $T_{final\ node}$.

4.3.3 Heat Generation

The volumetric heat generation term is calculated as $Q(z) = -S_r(z) + Q_T(z) + Q_{NRR}(z) + Q_{RR}(z)$ [34,82]. The first term in the heat generation equation is the local radiative heat source (Eq. (4.64)) where it is assumed that the lattice and free carrier absorption above the band-gap frequency is negligible. That same assumption holds for the second term which accounts for thermalization (Eq. (4.65)). The third term (Eq. (4.66)) is the heat generation caused by non-radiative recombination of EHPs while Eq. (4.67) is the heat generation caused by radiative recombination where Φ_{PR} represents the photon recycling factor [34,82].

$$S_{r,j} \approx \int_0^{\omega_g} \left[\frac{q_{\omega, \Delta z_j^{(p,n)}}^{emi} - q_{\omega, \Delta z_j^{(p,n)}}^{abs}}{\Delta z_j^{(p,n)}} \right] d\omega \quad (4.64)$$

$$Q_{T,j} = \int_{\omega_g}^{\infty} \left[\frac{q_{\omega, \Delta z_j^{(p,n)}}^{abs}}{\Delta z_j^{(p,n)}} \right] \left(1 - \frac{eE_g}{\hbar\omega} \right) d\omega \quad (4.65)$$

$$Q_{NRR,j} = \int_{\omega_g}^{\infty} \frac{eE_g}{\tau_{(e,h),NRR}} \Delta n_{(e,h),j,\omega} d\omega \quad (4.66)$$

$$Q_{RR,j} = \int_{\omega_g}^{\infty} \frac{eE_g}{\Phi_{PR} \tau_{(e,h),RR}} \Delta n_{(e,h),j,\omega} d\omega \quad (4.67)$$

The term $q_{\omega, \Delta z_j^{(p,n)}}^{emi}$ is calculated by multiplying $q_{\omega, \Delta z_j^{(p,n)}}^{abs}$ by $\frac{\Theta(\omega, T_{cell,j})}{\Theta(\omega, T_{rad})}$. It has to be noted that

$Q(z)$ does not take into account surface recombination. Thus in order to find the total volumetric heat generation term, $Q_{tot}(z)$ we add to $Q(Z_{top})$ and $Q(Z_{bot})$ (first and last node) the heat source due to surface recombination of EHPs which is calculated as $\frac{S_{e,h} eE_g \Delta n_{e,h}(Z_{top,bot})}{\Delta z}$ where $\Delta n_{e,h}$

is integrated over all frequencies above the band-gap frequency. The Q_{tot} value for the remaining nodes are equal to Q . To clarify, $Q(z)$ is used when employing Fourier's law while $Q_{tot}(z)$ is used when employing the MC simulation because it only models phonons and thus, does not include surface recombination of EHPs.

4.4 Concluding Remarks

A one-dimensional opto-electro-thermal model of a nano-gap TPV system to be used in the numerical simulation of a user-defined nano-gap TPV device is presented in this chapter. A general analytical expression for the radiative heat flux at the surface of the receiver is also detailed. The aforementioned numerical simulation allows us to predict the responses and performance of nano-gap TPV devices defined by user-defined parameters. This simulation method will be used in subsequent chapters to simulate different system configurations in order to gain more insight into their behaviours.

Chapter 5 Parametric Investigation of Nano-Gap Thermo-photovoltaic Energy Conversion

In this chapter, we study several parameters that affect the responses and performance of nano-gap TPV devices. It is important to have a good understanding of the parameters involved in order to guide the design of a particular near-field TPV converter. There are many factors that influence the performance of such devices such as the materials used, radiator design, gap size, layer thickness, cell design and temperature, just to name a few. The physics behind the operation of near-field TPV devices is well established, thus it is just a matter of applying that knowledge to produce predictions or to gain more understanding regarding the relationships between different quantities. One example would be the relationship between near-field radiative heat flux and gap size which is well documented. We know that as the vacuum gap shrinks, the near-field heat flux experiences enhancements but as the gap approaches zero, the heat flux value saturates as the radiative regime transitions into the conductive regime [8]. Furthermore, the rate of increase of the heat transfer depends on the thicknesses of the layers involved. For two SiC films exchanging radiative energy, the variation of the radiative heat transfer with gap size is governed by the ratios between the film thicknesses and the gap size [80]. The complexity of the problem is pretty evident here. It is not merely a relationship between two quantities but an intricate web of interconnecting factors that ultimately affect the near-field radiative energy exchange. Material type is another key component in the design of near-field TPV systems. Basu et al. [87] studied how the complex dielectric function of the radiator affected the near-field radiative heat transfer. They reported that the peak heat flux value for different constant dielectric functions occurs at different vacuum gap sizes e.g. for the case of $\epsilon_r = -1 + i0.1$, the heat flux value peaks when the gap size is 0.6 nm. This implies that each dielectric function has its own optimal gap size for maximum radiative heat transfer [87] and vice versa. However, real materials have frequency-dependent dielectric functions, necessitating the need to model these real materials in order to accurately gauge their effects on the near-field radiative heat transfer and subsequently the near-field TPV device.

The purpose of this chapter is not to provide a thorough theoretical explanation of how a single parameter and its underlying factors affect a nano-gap TPV system but to provide practical insights that can be used to guide the design process. The first parameter studied is the radiator material. Different types of materials are modelled and the resultant near-field radiative heat

transfer profiles are discussed. A metric to gauge the effectiveness of each material is presented. Next, different TPV cell materials are studied. Their electrical responses are discussed alongside their optical ones. The third parameter discussed is the cell thickness. We show how cell thickness affects the absorption of heat flux within the cell and how that affects the performance of the nano-gap TPV device. We then study the temperature profile within GaAs films of differing thicknesses subjected to near-field radiative heating through the use of phonon Monte Carlo (MC) simulations. In the last section, the doping-dependence of nano-gap TPV responses and performance is studied. We look at how varying the doping concentration affects the optical and electrical responses of the device and also its performance in terms of metrics such as the maximum output power and conversion efficiency.

Sections 5.1 to 5.5 have been published in the *Journal of Quantitative Spectroscopy and Radiative Transfer* and can be found in [88].

5.1 System Configuration and Simulation Parameters

In this chapter, a simple configuration which involves a bulk radiator and a film TPV cell separated by a 10-nm vacuum gap is modelled as depicted in Fig. 5.1. We are aware that such gap sizes are unrealistic with today's technology but since the purpose of this chapter is to capture parametric trends of nano-gap TPV systems, real-life reproducibility of the gap size is not of foremost concern. Moreover, we should expect similar trends for larger gap widths as long as the near-field regime is invoked. For configurations with larger gap sizes, the reader is referred to Chapters 6 to 8. The p -type region is given a thickness of 0.4 μm with a doping level, N_a of 10^{19} cm^{-3} while the n -type region is 10- μm thick with a doping level, N_d of 10^{17} cm^{-3} . Do note that these parameters are based on the values found in [33]. The radiator temperature, T_0 is assumed to be 1000 K (below the melting points of the radiator materials) while the cell temperature is kept at 300 K. The cooling system is modelled as vacuum to simplify the problem. The radiative heat flux transferred from the radiator to any point in the TPV cell is calculated using Eq. (4.30). When modelling the responses within the TPV cell, it is first discretised into one-dimensional nodes as shown in Fig. 4.3. The p -type region has 401 nodes while the n -type region has 801 nodes.

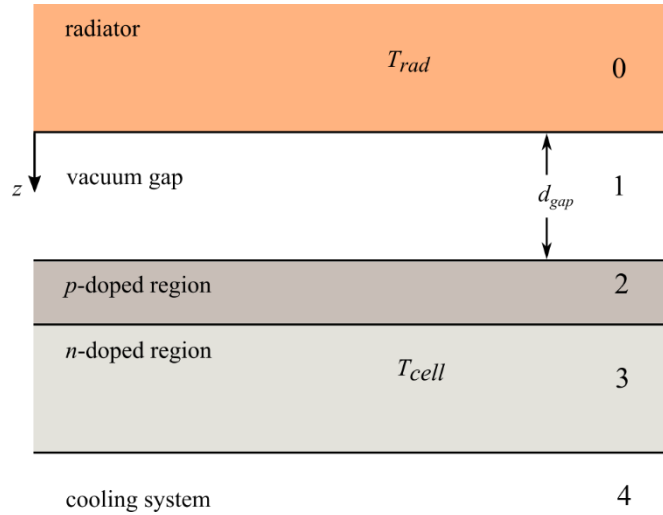


Fig. 5.1 Schematic representation of a nano-gap TPV device.

Four radiator materials are included in this investigation: tungsten (W), gallium arsenide (GaAs), silicon carbide (SiC) and, gold (Au). The dielectric functions of W and SiC are based on the data provided in [89]. The Au radiator is modelled using the Drude model based on the parameters in [70] which are listed in Appendix A and finally GaAs is modelled using Adachi's model [90]. Three TPV cell materials have also been included. The first material is silicon (Si) whose dielectric model is based on Green and Keever's work [91]. Its minority carrier mobility equations and the minority carrier lifetimes are taken from [92], and [93] respectively. GaAs can also function as a TPV cell. Its electrical properties are based on the work done by Satoodeh et al. [94]. The third cell material is indium gallium antimonide ($\text{In}_{0.18}\text{Ga}_{0.82}\text{Sb}$) whose dielectric function is modelled using Adachi's model [90] as done in [34,60] using the parameters provided in [95]. Its electrical properties: diffusion coefficients, lifetimes and surface recombination velocities are based on the work done in [34,60] and [95]. The same surface recombination velocity will be used for all three cell materials to make comparisons more meaningful. The doping dependence of the dielectric function of $\text{In}_{0.18}\text{Ga}_{0.82}\text{Sb}$ is not included due to insufficient data. For the sake of consistency, the same condition is applied to the other materials.

Once all the components are known and put into place, the numerical simulation described in Chapter 4 can then be started and will eventually yield the performance of the nano-gap TPV device. It has to be noted that the TPV cell is assumed to be at a constant 300 K, thus the heat transport modelling is not necessary. The internal quantum efficiency (IQE) of the TPV cell,

$\eta_{q,\omega}$ which can be defined as the percentage of absorbed photons converted into photocurrent is calculated as [33]:

$$\eta_{q,\omega} = \frac{\hbar\omega J_{ph,\omega}}{e[q_\omega(Z_2^+) - q_\omega(Z_4^+)]} \quad (5.1)$$

5.2 Radiator Materials

In order to study the effect of different radiator materials on the near-field heat transfer, the near-field radiative heat flux is calculated as a function of wavelength. GaAs is chosen as the TPV cell material as its properties are well understood. Furthermore, it is also a widely used PV cell material. Based on Fig. 5.2, the combination of GaAs-GaAs produces the most heat flux while Au-GaAs produces the least.

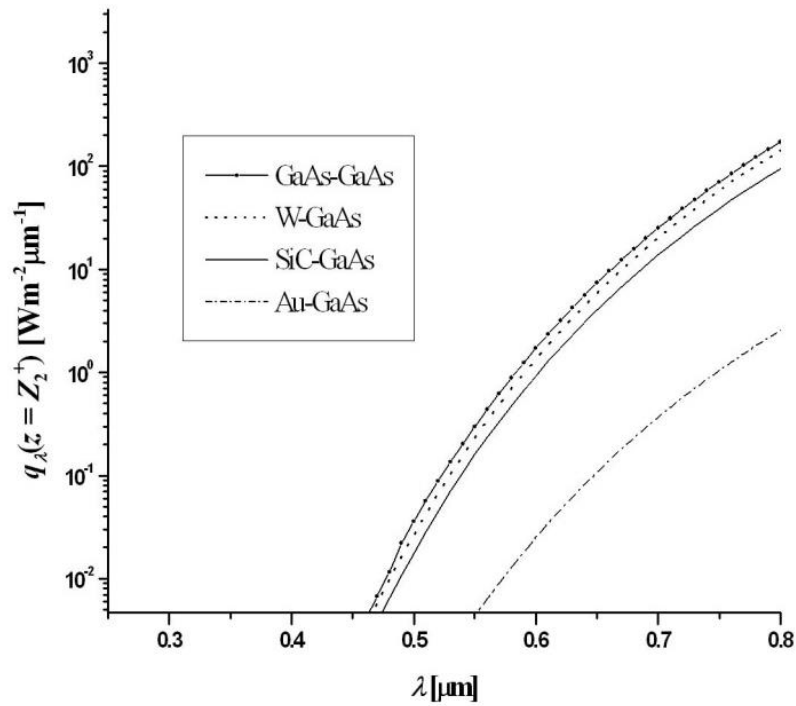


Fig. 5.2 Monochromatic radiative heat flux on the surface of the TPV cell for four radiator materials.

It is desirable for us to identify key characteristics that differentiate a good radiator from a bad one. One way to do this would be to study the near-field heat flux equation written here in terms of reflection coefficients [21,60]:

$$q_{\omega}^{prop}(z_2^+) = \frac{\Theta(\omega, T_0)}{4\pi^2} \int_0^{k_v} k_{\rho} dk_{\rho} \sum_{\gamma=TE, TM} \frac{(1 - |r_{01}^{\gamma}|^2)(1 - |R_2^{\gamma}|^2)}{|1 + r_{01}^{\gamma} R_2^{\gamma} e^{2ik_{z1}d_{gap}}|^2} \quad (5.2)$$

$$q_{\omega}^{evan}(z_2^+) = \frac{\Theta(\omega, T_0)}{\pi^2} \int_{k_v}^{\infty} k_{\rho} dk_{\rho} e^{-2k_{z1}d_{gap}} \sum_{\gamma=TE, TM} \frac{\text{Im}(-r_{01}^{\gamma})\text{Im}(R_2^{\gamma})}{|1 + r_{01}^{\gamma} R_2^{\gamma} e^{-2k_{z1}d_{gap}}|^2} \quad (5.3)$$

$$R_2^{\gamma} = \frac{r_{1,2}^{\gamma} + R_3^{\gamma} e^{2ik_{z2}t_2}}{1 + r_{1,2}^{\gamma} R_3^{\gamma} e^{2ik_{z2}t_2}} \quad (5.4)$$

$$R_3^{\gamma} = \frac{r_{2,3}^{\gamma} + r_{3,4}^{\gamma} e^{2ik_{z3}t_3}}{1 + r_{2,3}^{\gamma} r_{3,4}^{\gamma} e^{2ik_{z3}t_3}} \quad (5.5)$$

The Fresnel's reflection coefficient can be calculated using [65,96]:

$$r_{ij}^{TE} = \frac{k_{zi} - k_{zj}}{k_{zi} + k_{zj}} \quad (5.6)$$

$$r_{ij}^{TM} = \frac{\varepsilon_{rj} k_{zi} - \varepsilon_{ri} k_{zj}}{\varepsilon_{rj} k_{zi} + \varepsilon_{ri} k_{zj}} \quad (5.7)$$

Near-field heat transfer is dominated by its evanescent component, q^{evan} . Hence, we will be focusing on the evanescent heat flux equation. The term $\text{Im}(-r_{01}^{\gamma})$ can be described as the generalized emissivity (GE) of the radiator [21], allowing us to use it qualitatively to compare a variety of radiator materials. It has to be noted though that the term is not the emissivity defined in literature but merely a value which provides a description of a material's emittance in the near-field regime. Furthermore, GE is not a precise measurement of the strength of near-field heat transfer because it neglects possible surface polariton coupling between the radiator and the receiver and also wave interference effects. Though having said that, if no surface polariton coupling exists, a radiator with the highest GE value should yield the greatest heat flux. $\sum_{\gamma=TE, TM} \text{Im}(-r_{01}^{\gamma})$ is integrated over k_{ρ} from k_v to ∞ in order to obtain the overall GE value for the four radiators.

It is interesting to note from Table 5.1 that although W has a higher GE value than GaAs, the heat flux generated by the W-GaAs combination is lower. This observation could be explained by the coupling of surface phonon polaritons (SPhPs) in polar materials such as GaAs. When

both radiator and receiver support SPhPs, the surface waves would couple and enhance the heat transfer between the two media. Tungsten does not support SPhPs and would thus be unable to generate more heat flux than GaAs.

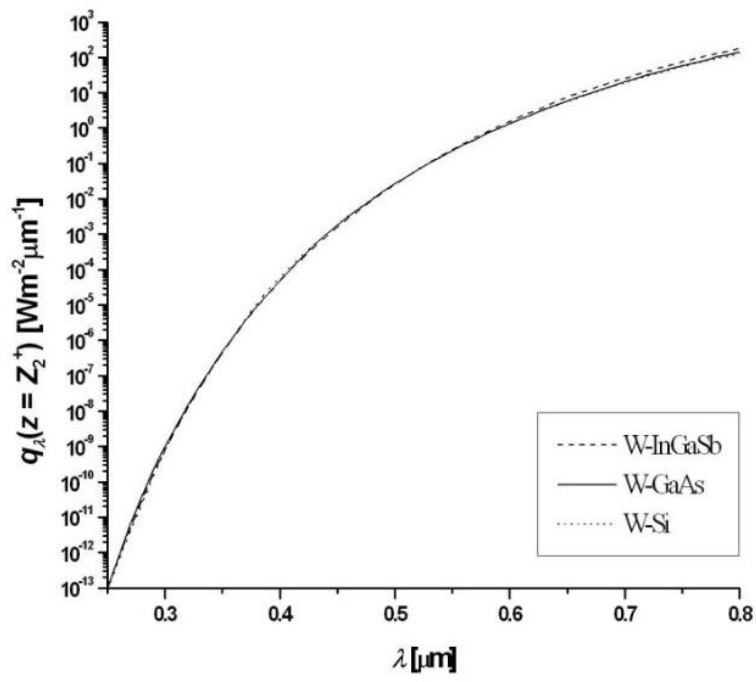
Table 5.1 GE values at $\lambda = 0.8 \mu\text{m}$

Material	Generalized Emissivity
GaAs	2.53×10^7
W	6.733×10^7
SiC	1.477×10^7
Au	3.227×10^6

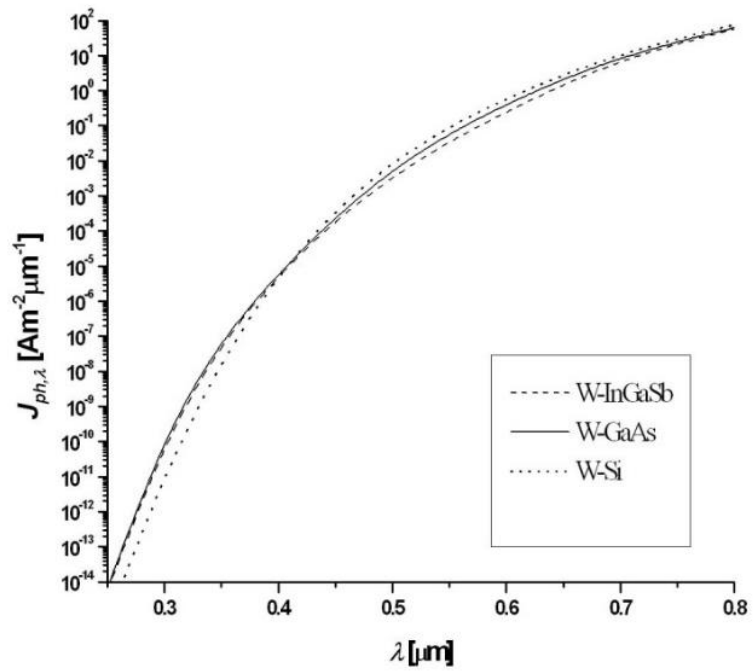
5.3 Cell Materials

The next parameter under investigation is the TPV cell material. The choice of material will affect the near-field heat flux, photocurrent generated, and the conversion efficiency. Tungsten (W) will be used as the sole radiator material. W was also used in past literature [33,60]. This will provide a basis for comparisons.

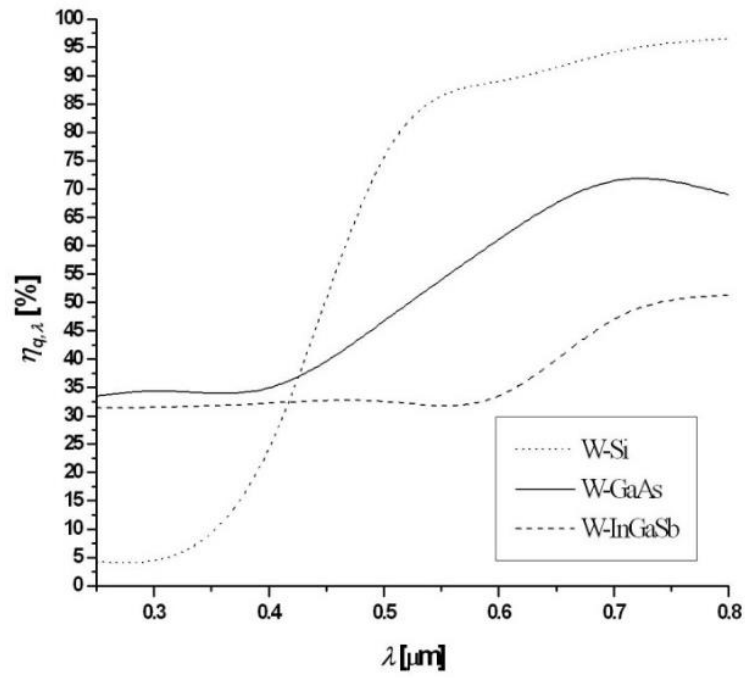
As shown in Fig. 5.3(a) and Fig. 5.3(b), the heat flux on the surface of the three cell materials and their photocurrents do not differ by much. Greater deviations start to appear at longer wavelengths where more heat flux is generated on the $\text{In}_{0.18}\text{Ga}_{0.82}\text{Sb}$ cell. At longer wavelengths, Si produces more photocurrent than the rest but produces less at shorter wavelengths. This is explained by the IQE results. The cells' IQEs as shown in Fig. 5.3(c), are heavily determined by their material properties. At longer wavelengths, the absorption coefficient decreases (Fig. 5.4) which causes the heat flux absorption to spread out across the entire thickness of the cell as depicted in Fig. 5.5(b).



(a)



(b)



(c)

Fig. 5.3 (a) Monochromatic radiative heat flux on the surface of the TPV cell for three radiator-receiver combinations. (b) Monochromatic photocurrents for three radiator-receiver combinations. (c) Internal quantum efficiency for three radiator-receiver combinations.

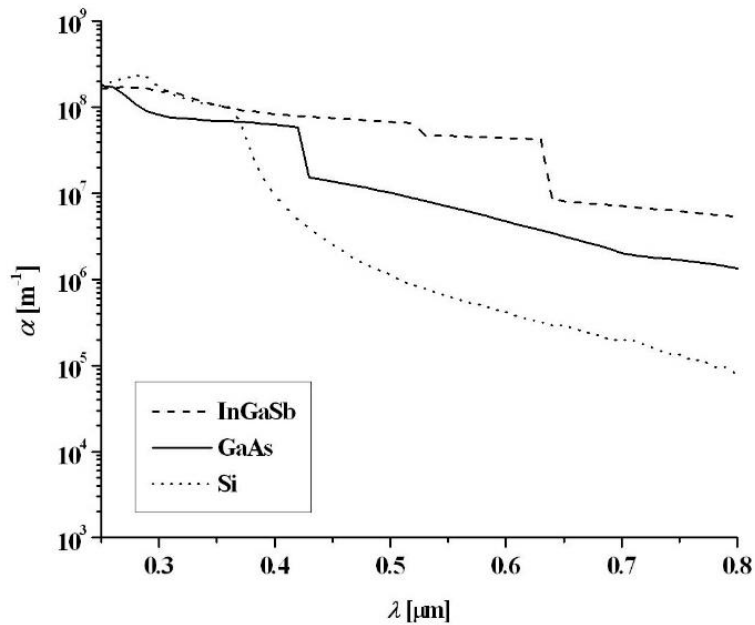
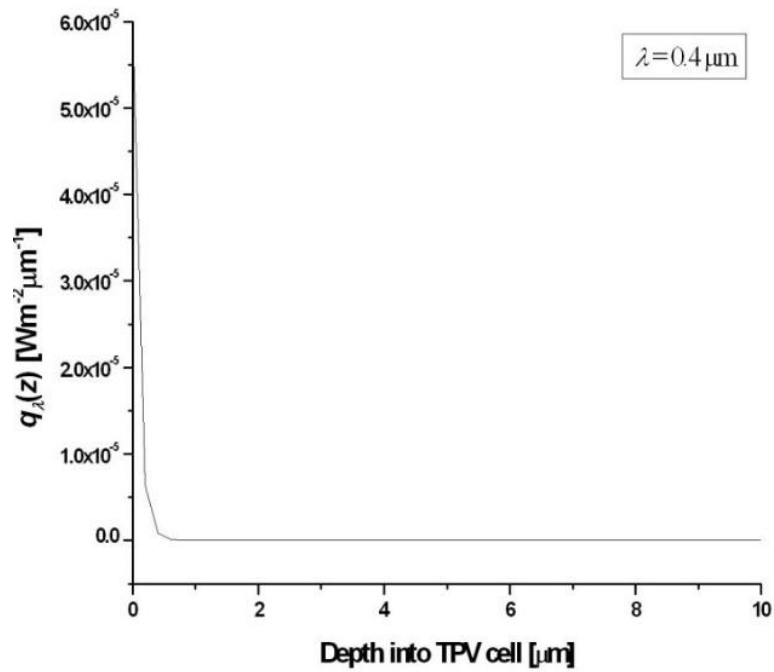
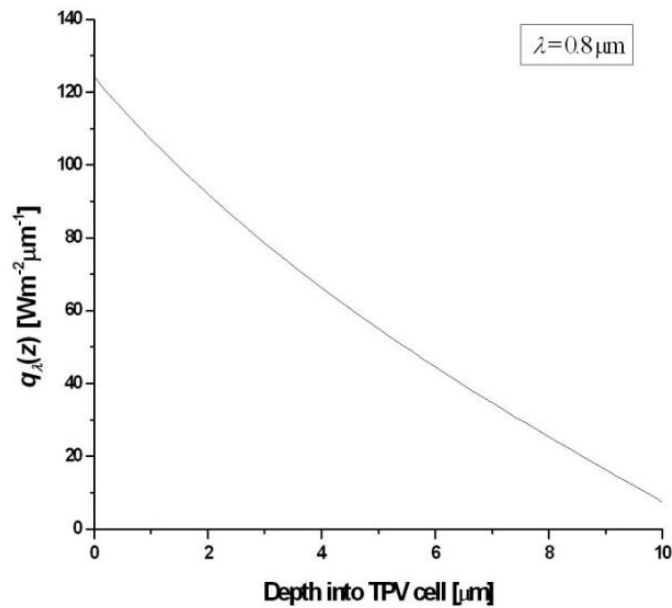


Fig. 5.4 Absorption coefficient for three TPV cell materials.



(a)



(b)

Fig. 5.5 Monochromatic radiative heat flux penetration into a Si cell at wavelengths, (a) $\lambda = 0.4 \mu\text{m}$ and (b) $\lambda = 0.8 \mu\text{m}$.

Due to the fact that the *n*-type region is thicker, the diffusion coefficient and the lifetime of minority holes within the *n*-type region greatly influence the IQE. In general, it is desirable to have high diffusion coefficients and minority carrier lifetimes. The Si cell achieved an IQE of

over 90% which could be explained by its properties in Table 5.2. Its diffusion coefficients are slightly lower compared to the other two materials but it has a far greater minority hole lifetime value. The τ_h value for Si is around three orders of magnitude larger than the rest.

Table 5.2 Electrical properties at 300 K

Properties	Si	GaAs	In _{0.18} Ga _{0.82} Sb
S_e (p -type region) [m/s]	2×10^{-4}	2×10^{-4}	2×10^{-4}
S_h (n -type region) [m/s]	0	0	0
D_e [m ² /s]	2.61×10^{-4}	4×10^{-3}	3.52×10^{-3}
D_h [m ² /s]	7.76×10^{-4}	7.07×10^{-4}	1.83×10^{-3}
τ_e [s]	2.27×10^{-8}	5.46×10^{-10}	5.52×10^{-9}
τ_h [s]	1.25×10^{-5}	8.54×10^{-9}	3.03×10^{-8}

On the other hand, at shorter wavelengths, most of the heat flux is absorbed at the surface of the cell (i.e. in the p -type region) as seen in Fig. 5.5(a). When this happens, minority electron properties and the surface recombination velocity of the surface become more important. The high S_e greatly reduced the IQE for all three materials. It is interesting to note that this time around, the IQE for Si is far lower compared to the rest. The effect of a lower diffusion coefficient is evident here.

5.4 Cell Thickness

In this section, a nano-gap TPV simulation is conducted for multiple thicknesses. The first simulation involves varying the n -type region's thickness while the p -type region is fixed at 0.4 μm . In the same way, when the p -type region's thickness is being varied, the n -type region is fixed at 10 μm . For all cases, a W radiator and a GaAs TPV cell are used.

Referring to Fig. 5.6 and Fig. 5.7, it can be observed that the IQE increases as thickness decreases up to a maximum point, from which it starts to fall. This could be explained by analysing the results in Fig. 5.8. As thickness increases, the absorption of heat flux shifts towards the surface. That is to say, a greater percentage of heat flux is absorbed closer to the surface. Initially this increases the IQE because more EHPs are generated closer to the depletion region, increasing the chances of collection as EHPs have a shorter distance to cover.

A greater percentage of heat flux is also absorbed within the depletion region itself, where it is assumed that all EHPs are swept across by the strong electric field and collected. However, as the thickness increases beyond the maximum IQE point, the influence of the surface recombination velocity of the top surface starts to dominate. Recombination also increases within the cell as EHPs in the p -type region are generated increasingly further away from the depletion region. Minority electrons in the p -type region have a shorter lifetime thus providing another possible explanation for the increase in recombination.

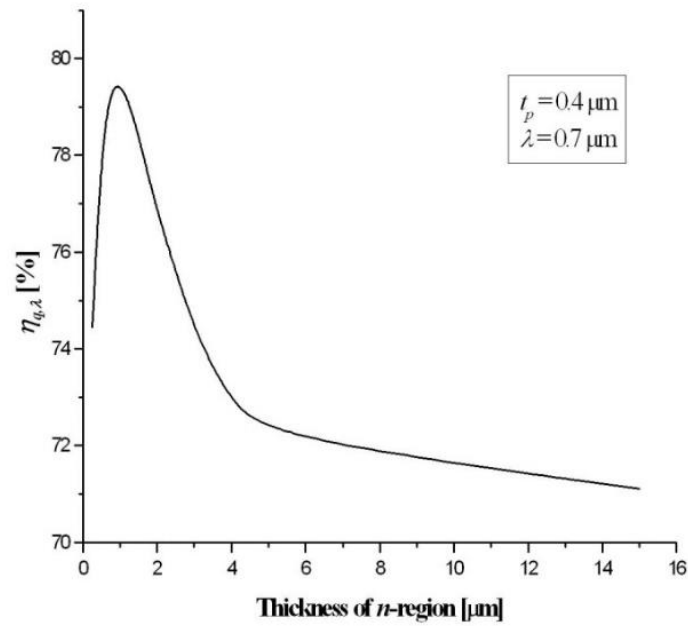


Fig. 5.6 Internal quantum efficiencies for varying n -type region thicknesses.

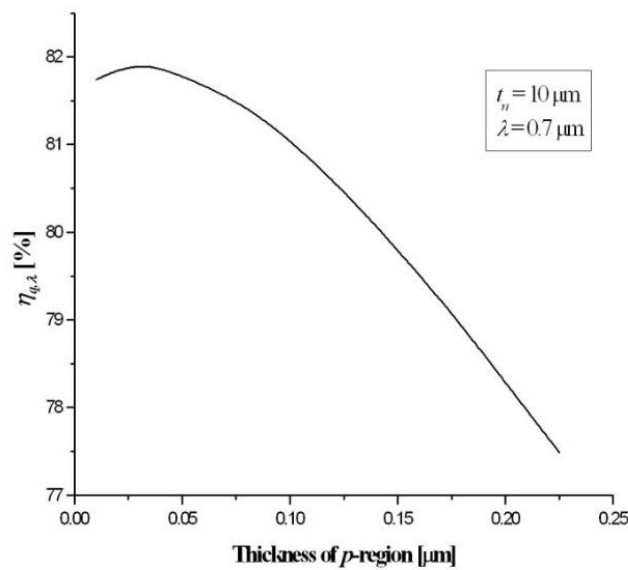


Fig. 5.7 Internal quantum efficiencies for varying p -type region thicknesses.

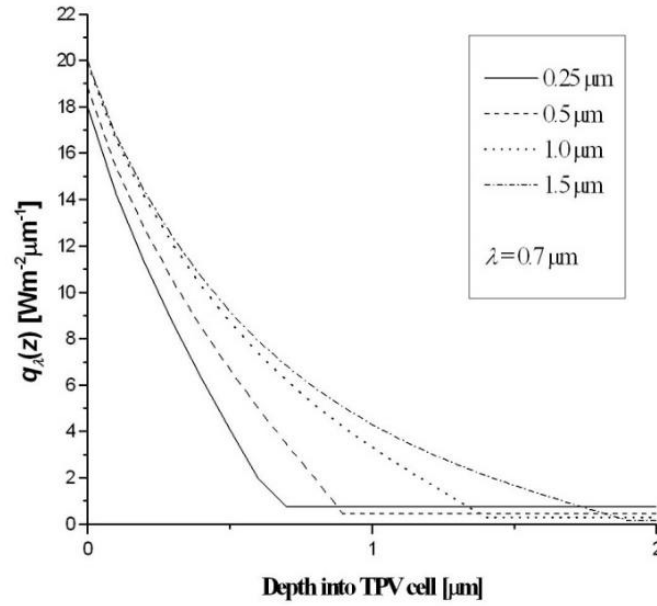


Fig. 5.8 Monochromatic radiative heat flux as a function of depth for varying n -region thicknesses.

5.5 Assessment of Temperature Profiles in GaAs Thin Films

A Monte Carlo simulation for phonon transport which is detailed in Section 4.3.2 is used to compute the temperature profile in thin-film layers of GaAs TPV cells. Do note that this analysis is separate from the nano-gap TPV simulation. The current work uses the MC simulation which has been detailed in [85] and [86]. A flow chart is shown in Fig. 4.4. The current simulation does not differentiate between the n -type and p -type layers. Instead, both layers are treated as a single layer of the same intrinsic material for simplicity. The main aim here is to study the effect of local heating due to the near-field thermal radiation on the temperature gradient in the thin-film layer.

The thin-film layer is assumed to have all adiabatic surfaces for the purpose of this study. In order to compute the local heat generation due to the near-field radiative heating, the volumetric heat absorbed is included in the MC simulation via a phonon creation scheme. The amount of heat generated, Q_{gen} in the system can be determined by multiplying the power density with the control volume and the time step applied in the simulation. Note that the power density here is the below-band-gap volumetric heat flux from the radiator absorbed by the thin film integrated over the effective frequency range of 7.7×10^{13} rad/s to 2.16×10^{15} rad/s (GaAs band gap) with

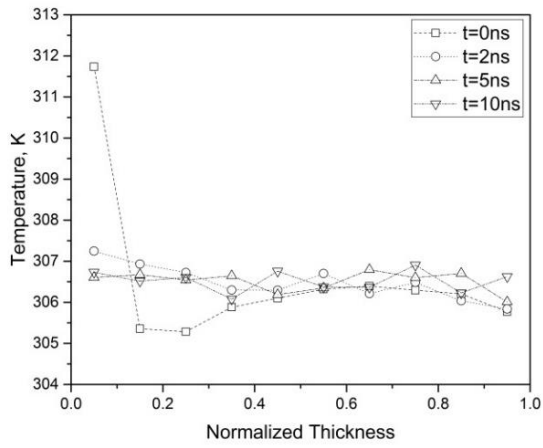
steps of 0.5×10^{13} rad/s. Thus, the power density in this case is not the internal heat generation detailed in Section 4.3.3.

The pseudo-temperature, T_{pseudo} of each of the control volumes can be computed based on Eq. (4.62). The number of phonons injected based on the corresponding local T_{pseudo} has to satisfy Eq. (4.63). It should be noted that this is only a crude approach to couple the MC simulation for phonon transport with the near-field radiative heating, as has been described by Wong et. al [97]. We have excluded the electron-hole pair generation in the current simulation, therefore only the heat absorbed below the band gap is being considered in the coupling process. This is based on the fact that electron-hole pairs will only be created if the energy level is above the band gap. Without consideration of the optical phonons which act as intermediaries between photons and acoustic phonons, and exist only for a very short amount of time in comparison to acoustic phonons, we hereby assume that the energy level below the band gap will be generating acoustic phonons directly. In addition, the heat absorbed will generate electron-hole pairs initially in reality. These electrons will disperse the energy further into the material before scattering the energy to phonons, thus leading to local heating. Without the incorporation of these mechanisms, the simulation will be only providing a crude overview of the temperature profile at the steady state. The information for the transient process on the other hand, calls for the inclusion of the electron-hole pairs and optical phonon generation.

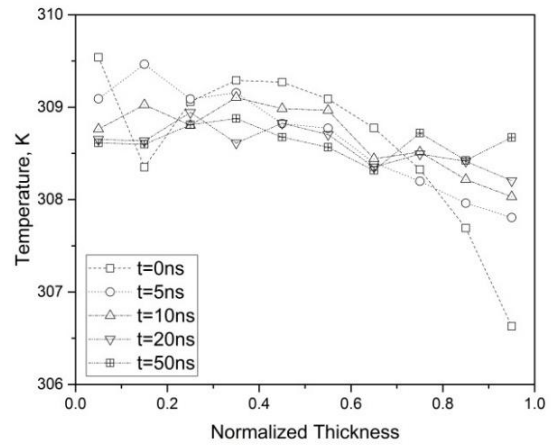
As heat is absorbed by the thin-film layer, phonons will be generated and the temperature is bound to rise. The thin-film layer is assumed to be intrinsic GaAs of thicknesses 1 μm , 3 μm and 5 μm exposed to near-field thermal radiation from a W radiator. These thicknesses are chosen because they are comparable or less than the acoustic phonon mean free path at room temperature [98] enabling us to study the interaction between semi-ballistic phonons and near-field thermal radiation. The type of material assumed differs from the initial assumption for the near-field radiative heating simulation which differentiates the *n*-type and *p*-type layers. The incorporation of the different doped layers requires information on the corresponding material properties in order to ensure an accurate MC simulation. This information however, is not readily available to the best of our knowledge. Careful recalibration of the MC simulation will also be required based on the new set of input. However, as the main interest of the current work lies in verifying whether or not a temperature gradient exists in the thin-film layer subjected to near-field radiative heating, the aforementioned assumption is therefore undertaken for the sake of simplicity.

Initially, the temperature of the GaAs thin-film layer is assumed to be at 300 K. Once heat is absorbed from the near-field radiative heating process, additional phonons are “created” following the local heat absorption rate. Thus, the temperature profile at the start will resemble that of the heat absorption profile. It has to be noted that however, due to the relatively small amount of energy below the band gap, it is insufficient to generate phonons at small time intervals of several picoseconds. As such, even though the simulation continues for a long period of time, no phonons will be generated and the temperature shall remain constant at 300 K throughout. This does not represent the true picture as continuous local heating will increase local temperature over time.

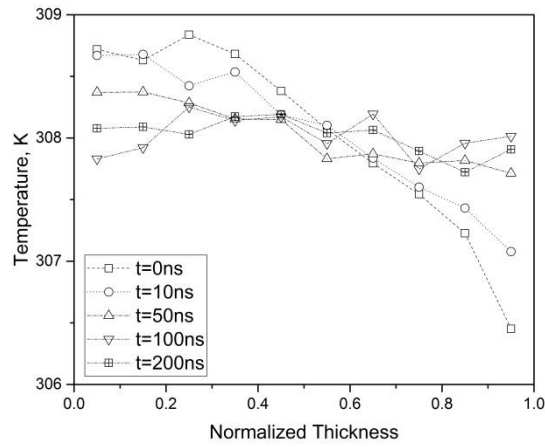
In view of this particular issue, we instead accumulate the heat absorbed up to 100 ms and 10 ms for radiator temperatures of 1000 K and 2000 K respectively before releasing the entire “parcel” of energy into the thin-film layer. Therefore, the heat absorbed time is numerically forced in the simulation. The time 100 ms and 10 ms are used respectively in order to achieve a considerable rise in temperature, thus providing a clearer view of the evolution of the temperature profile. Any lower value will lead to a lower temperature rise and the change in temperature profile will not be as distinct, since the temperature range will be much smaller. The use of any higher value is doable, but at the expense of longer computational time. Here, the amount of energy accumulated is sufficient to increase the temperature up to several kelvins, and is able to provide us with the initial temperature profile at $t = 0$ ns as shown in Fig. 5.9 and Fig. 5.10. This is done so as to demonstrate that transient near-field thermal radiation heating occurs at a much slower pace compared to the transient response of phonon conduction in GaAs. Even with the accumulated amount of near-field energy over a random selected timing hitting the material simultaneously, the temperature gradient still fades over time before the next amount sets in. As a result, there would be no temperature gradient within the film established over time. Rather, the entire film is at a uniform temperature which increases as time progresses.



(a)

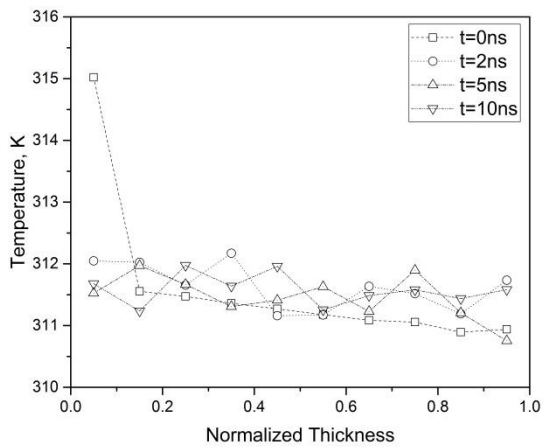


(b)

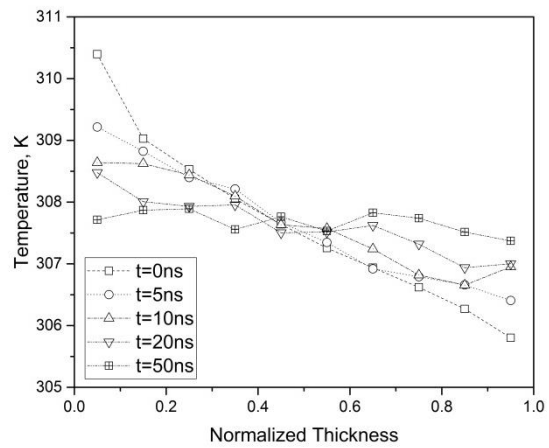


(c)

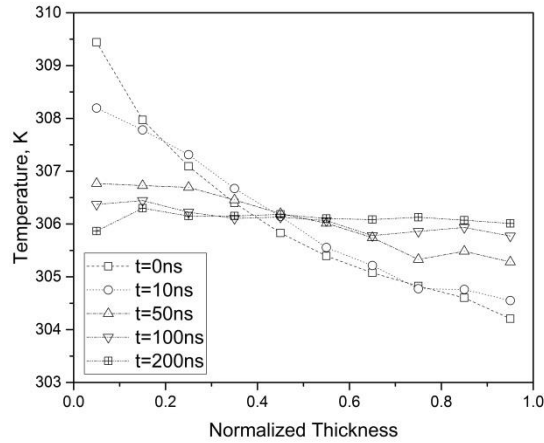
Fig. 5.9 Temperature profile in GaAs thin-film layer at radiator temperature of 1000 K, for layer thickness of (a) 1 μm , (b) 3 μm and (c) 5 μm .



(a)



(b)



(c)

Fig. 5.10 Temperature profile in GaAs thin-film layer at radiator temperature of 2000 K, for layer thickness of (a) 1 μm , (b) 3 μm and (c) 5 μm .

Note that the term normalized thickness used in both figures is computed as the ratio of thickness of the medium up to a particular point to the total thickness of the medium. It shows the thickness as a fraction of the total medium thickness. In both cases considered in this work, the local temperature at the start as well as the temperature at steady state (i.e. when the profile stabilizes) is the highest in the 1- μm thin film, and it gradually decreases as thickness increases to 3 μm and 5 μm . On the other hand, the transient process is longer in materials of higher thickness. While it takes approximately 10 ns to achieve steady state at a thickness of 1 μm , it takes up to 50 ns at 3 μm and 200 ns at 5 μm . The main implication here is that it will take a power density that is several orders of magnitude higher than that is obtained for GaAs to generate phonons at any particular instant in time. With low heat absorption rate, a very small phonon population is created at any instant to transport the energy slowly through the material. This coupled with a low material thermal conductivity means that the generated phonons will generally remain within the thin film and will be taking a longer amount of time to reach the lower temperature end. In view of the relatively short amount of time it takes to achieve steady state and the time for accumulating the energy prior to releasing it in the medium, the difference ranges from 5 to 7 orders of magnitude in all the cases considered. As such, it is possible that over time, a temperature gradient may not be expected within the thin-film layer and the temperature rise over a long period of time due to near-field radiative heating may closely resemble a single constant value. Thus, any crude computations related to the thin film can be carried out by assuming a single temperature over time instead of assuming a temperature gradient. A similar conclusion was also obtained based on a previous work [97]; however, the

material used in that particular work was silicon, which has different phonon properties than those of gallium arsenide.

5.6 Doping Dependence

Many studies have shown that varying the doping concentration affects the performance of PV cells. One such study was conducted by Duran et al. [99] where they attempted to optimize the junction depth and doping concentration of solar cell emitters. The term ‘emitter’ used in this section refers to the top layer of the p - n junction and should not be confused with the TPV radiation source. They varied the emitter doping concentration from $8 \times 10^{18} \text{ cm}^{-3}$ to 10^{20} cm^{-3} and discovered that the cell efficiency increases with doping concentration up to an optimum value of $1.5 \times 10^{19} \text{ cm}^{-3}$ above which the efficiency decreases. Karazhanov [100] studied the doping-dependence of a Si solar cell by varying the doping concentration of its p -type base region. As doping concentration is increased from 10^{16} cm^{-3} to 10^{18} cm^{-3} , the minority carrier diffusion length, short-circuit current, J_{sc} , open-circuit voltage, V_{oc} , fill factor, FF and efficiency experience declines. They concluded that the optimal doping concentration should be less than 10^{17} cm^{-3} . Relatively similar conclusions were made by Ouyang et al. [101] in their experimental study of thin-film polycrystalline Si solar cells. The doping concentration of the p -type base/absorber region was varied from around $2 \times 10^{15} \text{ cm}^{-3}$ to $8 \times 10^{17} \text{ cm}^{-3}$. Their results show that J_{sc} values are greatest at lower doping concentrations while V_{oc} and pseudo fill factor values peak at concentrations of $1\text{--}2 \times 10^{17} \text{ cm}^{-3}$. They noted that J_{sc} is the dominating determinant of conversion efficiency, thus cell efficiency decreases as base doping concentration increases. Furthermore, they determined that the effective diffusion length, L_{eff} of minority carriers is one of the major parameters that affect quantum efficiency. A high L_{eff} would increase the collection probability of light-generated carriers, subsequently increasing efficiency. It has to be noted that these studies use an n -on- p cell configuration where the n -type layer is placed above the p -type layer with the n -type layer receiving light first.

The doping concentration of a semiconductor also influences near-field heat transfer. Fu and Zhang [102] studied the thermal energy transfer between Si parallel plates at different doping concentrations. Based on their calculations, an increase in doping concentration significantly increases the extinction coefficient of Si due to increased free carrier absorption. This increased contribution from free carriers causes greater spectral radiative heat flux at lower angular

frequencies (below 10^{14} rad/s). Moreover, the net energy flux between two heavily doped Si plates is significantly higher than Si plates with lower doping concentrations. In another paper, the PV cell properties such as minority carrier mobility, diffusion coefficient, lifetime and depletion region length are all shown to be doping-dependent [82].

These studies allow us to safely conclude that changing the doping concentration of the TPV cell in a nano-gap TPV device would definitely affect its optical and electrical responses which in turn determine the performance of the entire system. As a reminder, a TPV cell is merely a PV cell used within the context of a TPV system. In this section, we would like to shed more light on the relationship between doping concentration and the aforementioned responses of the device. The doping-dependence of a nano-gap TPV device that utilizes a *p-on-n* Si PV cell will be studied. The radiator is kept at 2000 K while the TPV cell remains at 300 K with a gap of 10 nm separating the two layers.

5.6.1 System Configuration and Simulation Parameters

We model a nano-gap TPV device based on the configuration depicted in Fig. 5.11 which is similar to the one in Fig. 5.1 except that we now keep the radiator temperature at 2000 K and introduce additional terms to the diagram. The terms, t_{emit} and t_{abs} refer to the thickness of the TPV cell emitter and absorber regions respectively. Silicon carbide, SiC (a common infrared radiator) is used as the radiator (layer 0) while a Si (an extremely common PV cell material) *p-n* junction (layers 2 and 3) is used as the TPV cell. Media 1 and 4 are modelled as vacuum. The SiC radiator is modelled as a damped harmonic oscillator (Eq. (5.8)) using the parameters (Table 5.3) found in [89]. The Si TPV cell's dielectric function is described using a Drude model (Eq. (5.9)) detailed in [102] with the addition of a lattice absorption model from [103]. The ionization model of dopants used in our work is taken from [104].

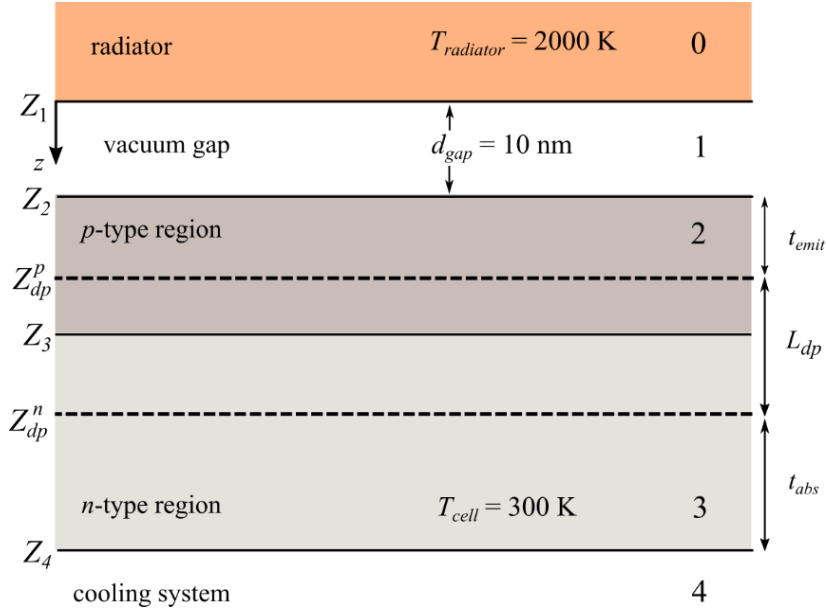


Fig. 5.11 Schematic diagram of a nano-gap TPV device.

Table 5.3 Parameters for modelling SiC.

ε_∞	ω_{TO} [rad/s]	ω_{LO} [rad/s]	Γ [s^{-1}]
6.7	1.494×10^{14}	1.825×10^{14}	8.966×10^{11}

$$\varepsilon_r(\omega) = \varepsilon_\infty \left(\frac{\omega^2 - \omega_{LO}^2 + i\Gamma\omega}{\omega^2 - \omega_{TO}^2 + i\Gamma\omega} \right) \quad (5.8)$$

$$\varepsilon_r(\omega) = \varepsilon_{bl} - \frac{N_e e^2 / \varepsilon_0 m_e^*}{\omega^2 + i\omega / \tau_e} - \frac{N_h e^2 / \varepsilon_0 m_h^*}{\omega^2 + i\omega / \tau_h} \quad (5.9)$$

The SiC radiator is kept at 2000 K while the TPV cell is kept at 300 K. The frequency range of the simulation is from 5×10^{12} rad/s to 3.8×10^{15} rad/s. The thickness of the p -type region is $0.4 \mu\text{m}$ while the n -type region is $10 \mu\text{m}$ thick. The surface recombination velocities of the TPV cell are taken from [82] where $S_e = 10$ m/s, $S_h = 1$ m/s. The doping concentration in the p -type region (acceptor), N_a is varied from 10^{23} m^{-3} to 10^{25} m^{-3} . For each N_a value, the n -type region doping concentration (donor), N_d is varied from 10^{21} m^{-3} to 10^{24} m^{-3} . These values are chosen based on the doping concentrations used in past studies which are mentioned in the introduction of Section 5.6. The results are presented below.

5.6.2 Performance

As shown in Fig. 5.12 the highest conversion efficiency among the simulated conditions occurs when $N_a = 10^{23} \text{ m}^{-3}$ and $N_d = 10^{22} \text{ m}^{-3}$. It is interesting to note that as N_a is increased, the optimum N_d —to produce the greatest efficiency—for that particular N_a value increases as well, up to $N_d = 10^{23} \text{ m}^{-3}$ where P_m is greatest (Fig. 5.13(b)). This is because at higher N_a values (p -type region), the rise in P_{abs} (Fig. 5.13(a)) is less sensitive to the increase in N_d (n -type region) while the sensitivity of P_m increases. In other words, the P_{abs} profile is flatter at higher N_a values. Thus at $N_a = 10^{25} \text{ m}^{-3}$ and $N_d = 10^{23} \text{ m}^{-3}$, the efficiency peak coincides with the P_m peak. Referring to Fig. 5.14, the short-circuit current, J_{sc} (equivalent to J_{ph}) and the open-circuit voltage, V_{oc} are maximum at around $N_d = 10^{23} \text{ m}^{-3}$ which coincides with the point of maximum P_m . It is commonly reported that the doping concentration of the PV cell absorber region (N_d) needs to be as low as possible in order to maximize the effective minority carrier diffusion length, L_{eff} in order to achieve greater J_{sc} values which should improve efficiency [101]. However, the diffusion length may not be the only deciding factor, especially when TPV cells are relatively thin as is the case in this section. The results shown in Fig. 5.12 to Fig. 5.14 do seem to indicate that increasing N_d does improve performance up to a certain optimum value. This interesting observation will be analysed in Section 5.6.4.

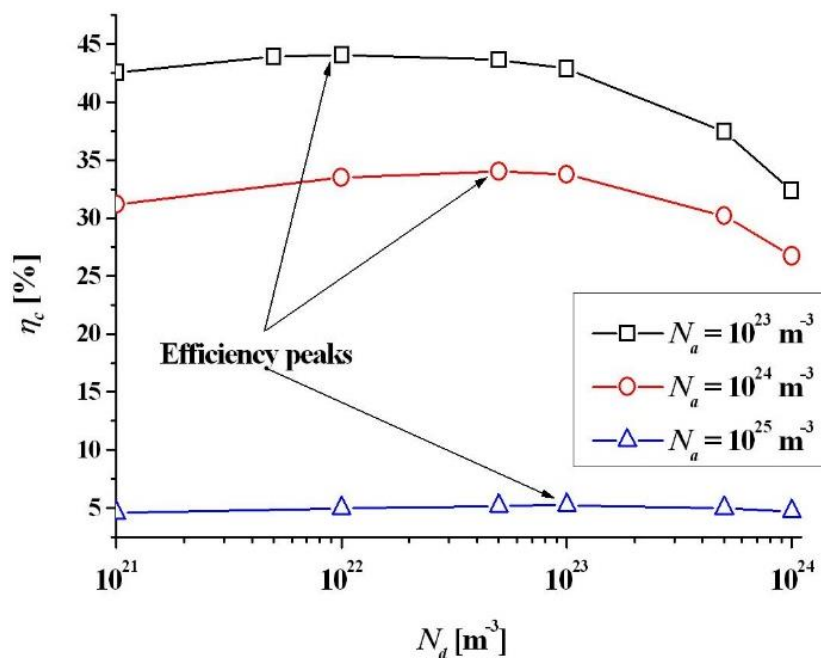
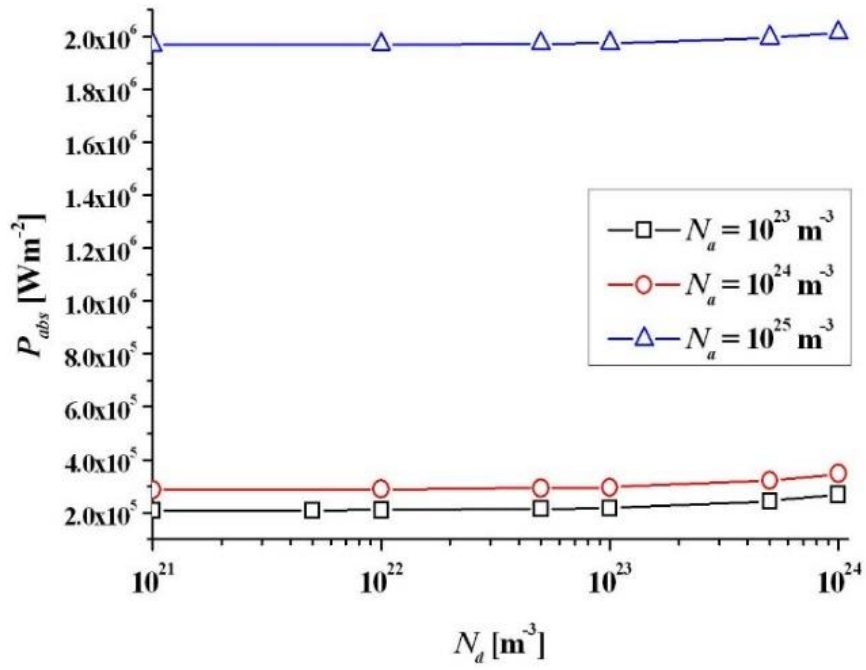
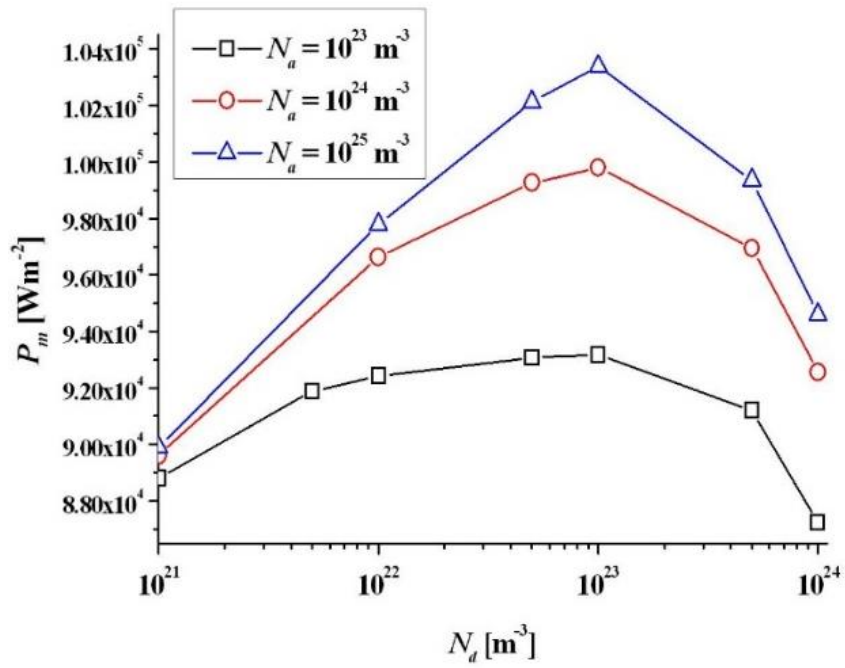


Fig. 5.12 Conversion efficiencies at different doping concentrations. (Note that only symbols represent actual data points. This is true for all figures with symbols).

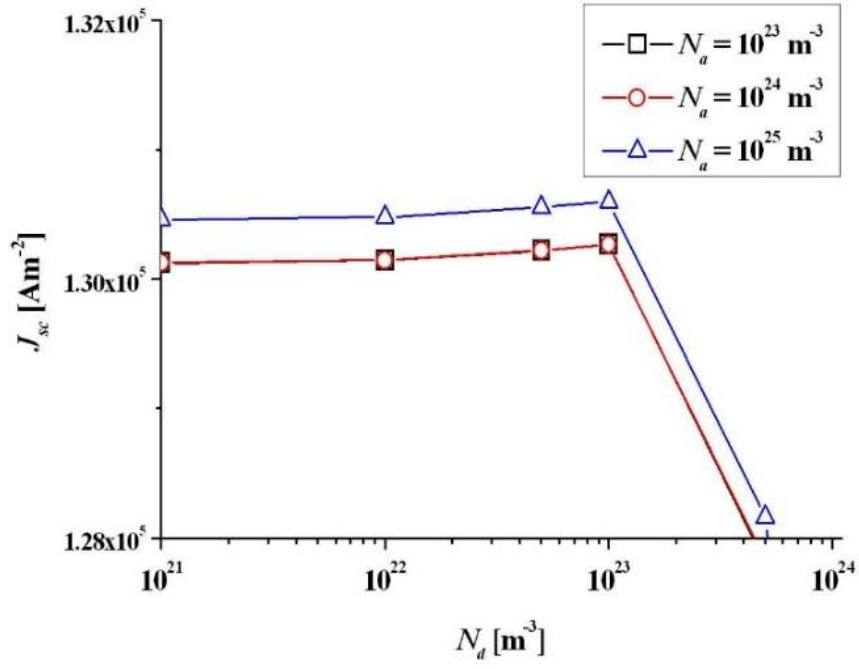


(a)

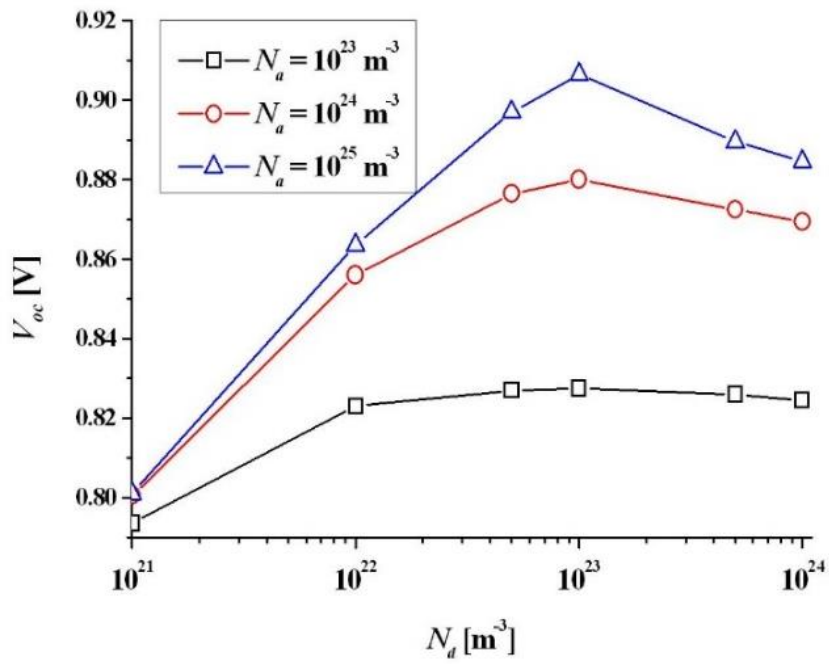


(b)

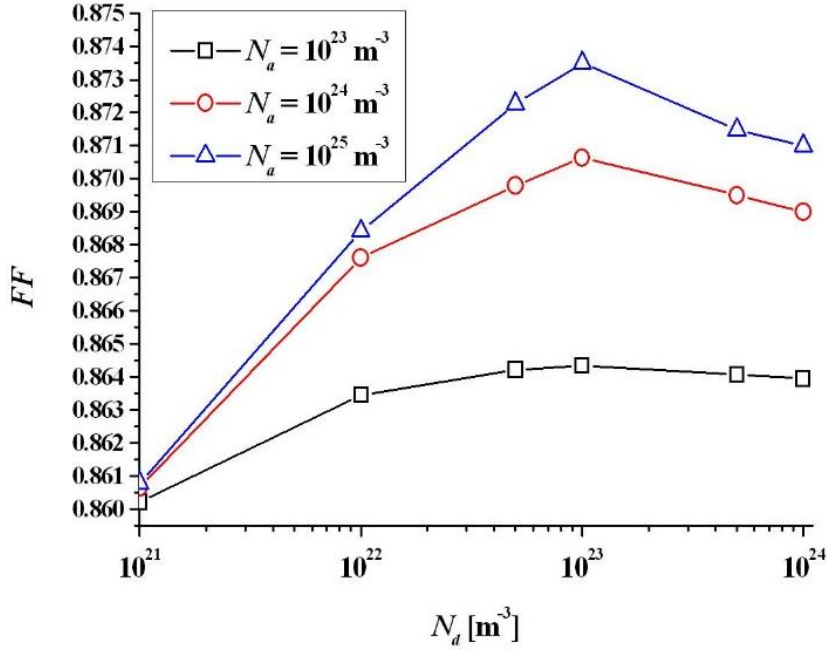
Fig. 5.13 (a) Total absorbed radiative heat flux and (b) maximum output power at different doping concentrations.



(a)



(b)



(c)

Fig. 5.14 (a) Short-circuit current, (b) open-circuit voltage and (c) fill factor at different doping concentrations.

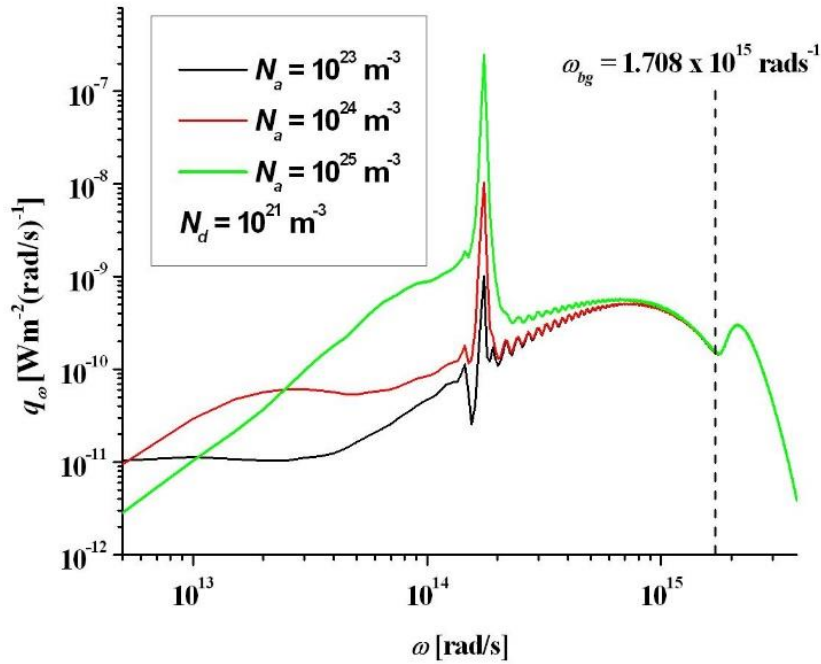
5.6.3 Optical Response

In this section, the optical response of the nano-gap TPV device is analysed. The effect of doping concentration on the spectral radiative heat flux profile is presented.

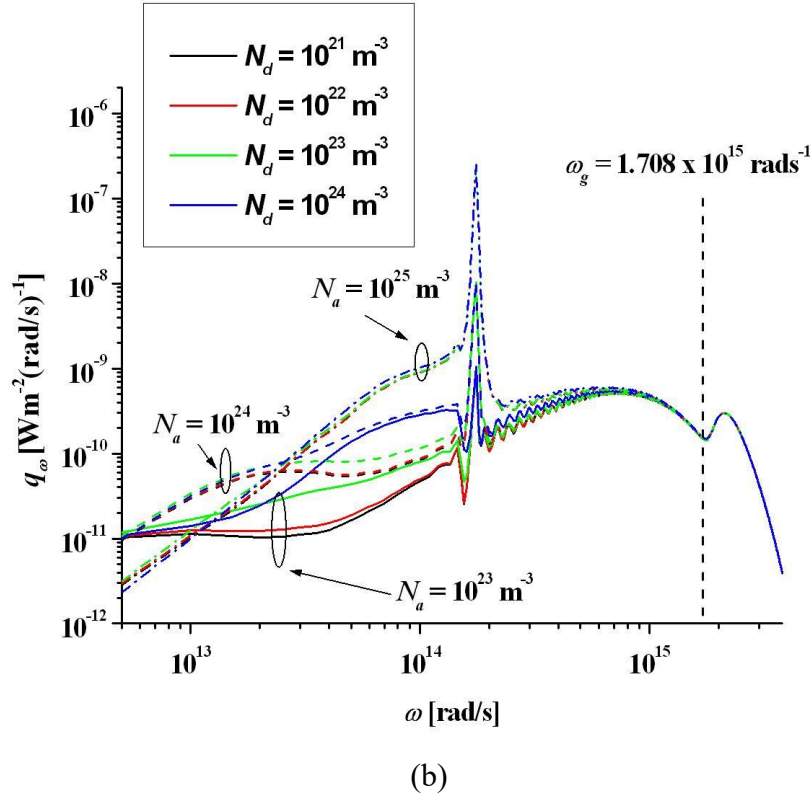
Based on Fig. 5.15(a), as N_a is increased, the spectral radiative heat flux on the surface of the TPV cell increases significantly below the band-gap frequency, ω_g while above-band-gap improvements are rather small. The narrow heat flux peak is caused by surface phonon-polariton resonance. The increase in heat flux can be explained by the greater absorption coefficient in highly doped silicon [102] due to increased free carrier absorption. Greater absorption increases the so-called spectral absorptance (generalized emissivity), $\left(1 - |R_2^\gamma|^2\right)$ and $\text{Im}(R_2^\gamma)$ (in Eqs. (5.2) and (5.3), respectively) of the TPV cell [21,60,88]. However, greater absorption below the band gap does not result in increased generation rate, thus the conversion efficiency of the nano-gap TPV device drops drastically as N_a increases as shown in Fig. 5.12. It is interesting to note that the heat flux values at lower frequencies for $N_a = 10^{25} \text{ m}^{-3}$ are smaller than the other two profiles. It is difficult to pinpoint the exact reason for this observation but one possible explanation could be the increased monochromatic behaviour as a result of

greater coupling at and around the resonant frequency of the SiC-vacuum interface (1.786×10^{14} rad/s). Increasing N_a beyond 10^{25} m^{-3} may further enhance and narrow the radiative heat flux profile. However, such enhancements will not improve conversion efficiency as they occur below the band gap. Another thing to note is the oscillatory behaviour between approximately 2×10^{14} rad/s and 10^{15} rad/s. The curious profile is caused by low absorption in the cell which leads to a greater number of reflected waves. These waves overlap to produce those interference patterns [60].

Referring to Fig. 5.15(b), at lower N_a values, as N_d increases, the heat flux sees noticeable increase between 10^{13} rad/s and 1.5×10^{14} rad/s due to increased free carrier absorption. However, at $N_a = 10^{25} \text{ m}^{-3}$, the change in heat flux induced by the change in N_d becomes insignificant which explains the weaker sensitivity of P_{abs} to N_d . This shows that at higher absorption coefficients, the optical response of the surface layer is the dominant factor in determining the radiative heat flux. Thus, in order to achieve maximum radiative heat transfer, only a very thin layer at the surface of the TPV cell needs to be highly doped. It is interesting to note that even though the increase in N_d generates more unusable spectral heat flux (below ω_g), the conversion efficiency actually increases up to a certain optimum value which differs for different values of N_a as discussed in Section 5.6.2. This shows that the improvements brought about by increasing N_d outweighs its negative effects.



(a)



(b)
 Fig. 5.15 Monochromatic radiative heat flux on the surface of the TPV cell as a function of angular frequency when (a) N_d is fixed at 10^{21} m^{-3} and for (b) different combinations of N_a and N_d .

5.6.4 Electrical Response

In this section, the effect of doping concentration on the electrical properties of the TPV cell and subsequently the generated photocurrent, J_{ph} at short-circuit conditions is analysed and the reason for the improvements generated by increasing N_d is explained.

5.6.5 Varying N_a

Referring to Fig. 5.16, as N_a increases, J_e (p -type region) experiences improvements while J_h (n -type region) declines. The increase in J_e is due to the buildup of excess minority carriers, Δn_e (Fig. 5.17(a)) in the emitter region. This buildup is caused by greater electron-hole pair (EHP) concentration as t_{emit} increases and the diffusion coefficient decreases (Table 5.4). The value of J_{dp} depends on the width of L_{dp} which is the sum of the depletion region width in both p and n -type regions. Furthermore, they are all functions of N_a and N_d [83,84]. Thus, a wider depletion region generates more J_{dp} . When N_d is below 10^{22} m^{-3} , an increasing N_a widens L_{dp} . However, above $N_d = 10^{22} \text{ m}^{-3}$, the opposite is true as L_{dp} becomes narrower which explains the

decreasing J_{dp} as N_a increases in Fig. 5.16(a). However, the portion of the depletion region width in the n -type region continues to increase as N_a increases (t_{abs} decreases), causing less radiative heat flux to be absorbed in the absorber region thus generating less EHPs which reduces J_h albeit in small amounts (Fig. 5.16(b)). Overall, the increase in J_e and J_{dp} causes the total photocurrent, J_{ph} to increase as N_a is increased from 10^{23} m^{-3} to 10^{25} m^{-3} .

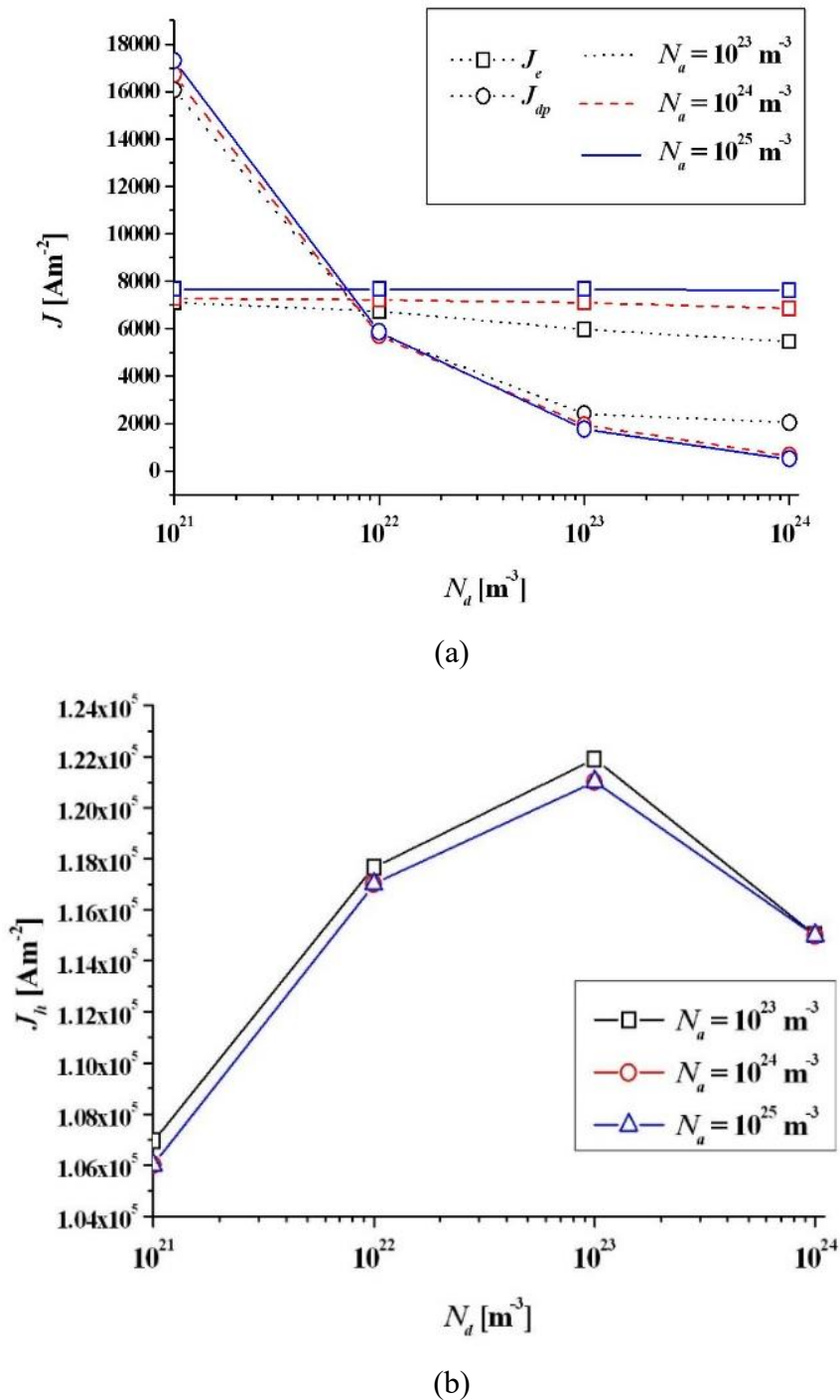
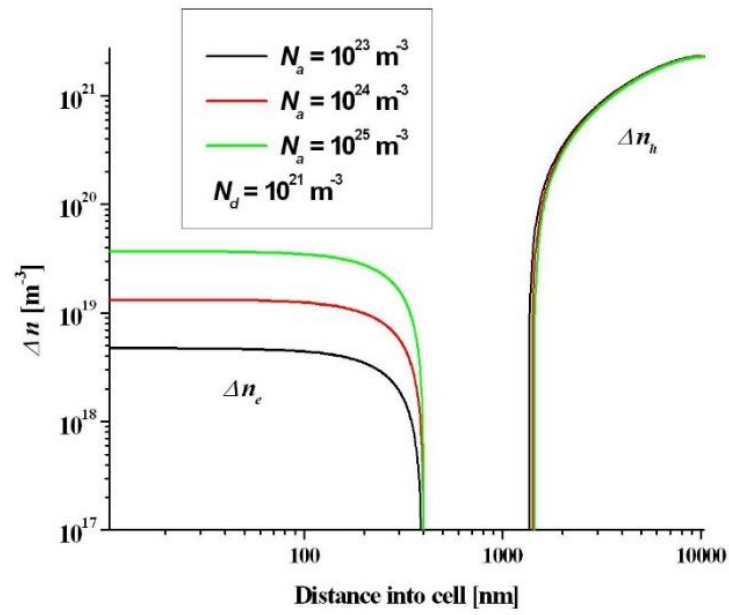
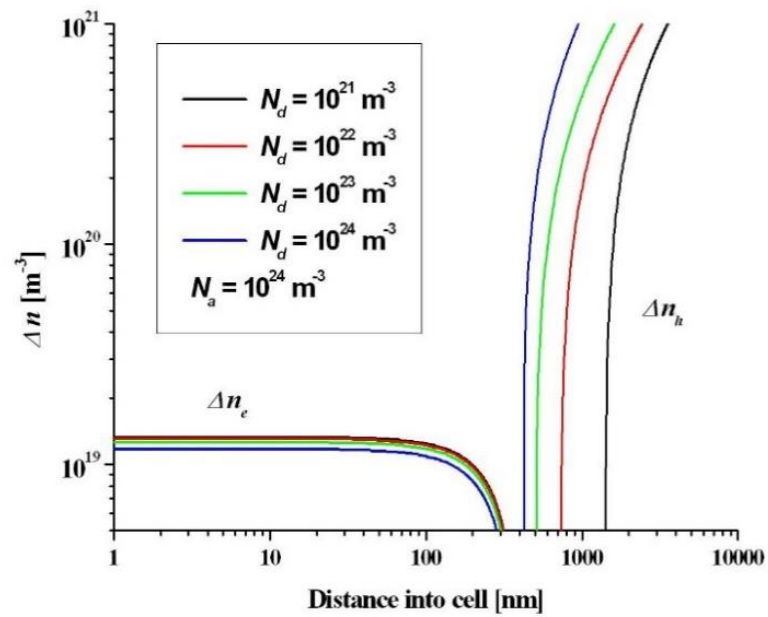


Fig. 5.16 Photocurrents, (a) J_e , J_{dp} and (b) J_h at different doping concentrations.



(a)



(b)

Fig. 5.17 Excess minority carrier concentration as a function of distance into cell when (a) N_d is fixed at 10^{21} m⁻³ and (b) N_a is fixed at 10^{24} m⁻³.

Table 5.4 Diffusion coefficient, lifetime and effective diffusion length of minority electrons at different acceptor concentrations.

N_a (m ⁻³)	D_e (m ² /s)	τ_e (s)	$L_{eff,e}$ (m)
10 ²³	1.86×10 ⁻³	2.89×10 ⁻⁶	7.33×10 ⁻⁵
10 ²⁴	6.91×10 ⁻⁴	2.82×10 ⁻⁷	1.40×10 ⁻⁵
10 ²⁵	2.61×10 ⁻⁴	2.27×10 ⁻⁸	2.43×10 ⁻⁶

5.6.6 Varying N_d

Referring to Fig. 5.16, J_e and J_{dp} decrease as N_d is increased. Greater N_d values cause the portion of the depletion region width in the p -type region to expand when N_a is fixed. This reduces the thickness of the TPV cell emitter region, t_{emit} which subsequently reduces the amount of EHPs generated in this region, hence the declining J_e . However, the overall width, L_{dp} shrinks (t_{abs} increases) causing less J_{dp} to be generated.

J_h increases as N_d is increased from 10²¹ m⁻³ to 10²³ m⁻³ but drops when N_d is increased further. J_h is proportional to D_h and also to the excess minority carrier gradient at the depletion region boundary in the n -type region [82]. The increase of J_h as doping concentration increases can be explained by the increase in the gradient due to the buildup of Δn_h (Fig. 5.17(b)) during illumination as a result of the lower D_h (Table 5.5) while τ_h remains largely unchanged i.e. the recombination rate is hardly affected. This shows that a lower D is only useful when τ remains relatively constant. However, it has to be noted that the diffusion length, $L_{eff,h}$ continues to decrease. At $N_d = 10^{24}$ m⁻³, the negative effect of a much lower D_h on J_h outweighs the buildup of Δn_h , hence the smaller J_h value. Furthermore, at 10²⁴ m⁻³, τ_h experiences quite a significant decline which also compromises the buildup of Δn_h . This ties in with the physical picture where a lower D_h and τ_h reduce the collection probability of EHPs, causing less current to be generated. However, it is clear that relying on L_{eff} as a measure to predict performance is not sufficient especially when the TPV cell is thin to begin with. It would be wiser to include in the analysis the effects of D and τ as the interplay between these two parameters paints a more complete picture. J_h is the main contributor of photocurrent and thus the J_{ph} profile trend is consistent with that of J_h . The peak value of J_{ph} occurs at $N_d = 10^{23}$ m⁻³ which explains the P_m profile in Fig. 5.13(b).

Table 5.5 Diffusion coefficient, lifetime and effective diffusion length of minority holes at different donor concentrations.

N_d (m^{-3})	D_h (m^2/s)	τ_h (s)	$L_{\text{eff},h}$ (m)
10^{21}	1.21×10^{-3}	1.25×10^{-5}	1.23×10^{-4}
10^{22}	1.10×10^{-3}	1.25×10^{-5}	1.17×10^{-4}
10^{23}	7.76×10^{-4}	1.25×10^{-5}	9.85×10^{-5}
10^{24}	3.70×10^{-4}	1.04×10^{-6}	1.96×10^{-5}

5.6.7 Dark Current

Based on Fig. 5.18, as N_d increases from 10^{21} m^{-3} to 10^{23} m^{-3} , the dark current (diode current) decreases. As doping increases (greater majority carrier concentration), the dark saturation current due to recombination decreases as it is inversely proportional to the doping concentration [72]. This is because recombination is limited by the equilibrium minority carrier concentration, thus a lower minority carrier concentration would reduce the recombination rate [76]. However, at $N_d = 10^{24} \text{ m}^{-3}$, the trend reverses due to the much lower τ_h , which increases recombination. This explains the V_{oc} and FF profiles in Fig. 5.14(b) and Fig. 5.14(c). Thus maximizing the photocurrent should not be the only goal as reducing the dark current contributes towards the increase in efficiency.

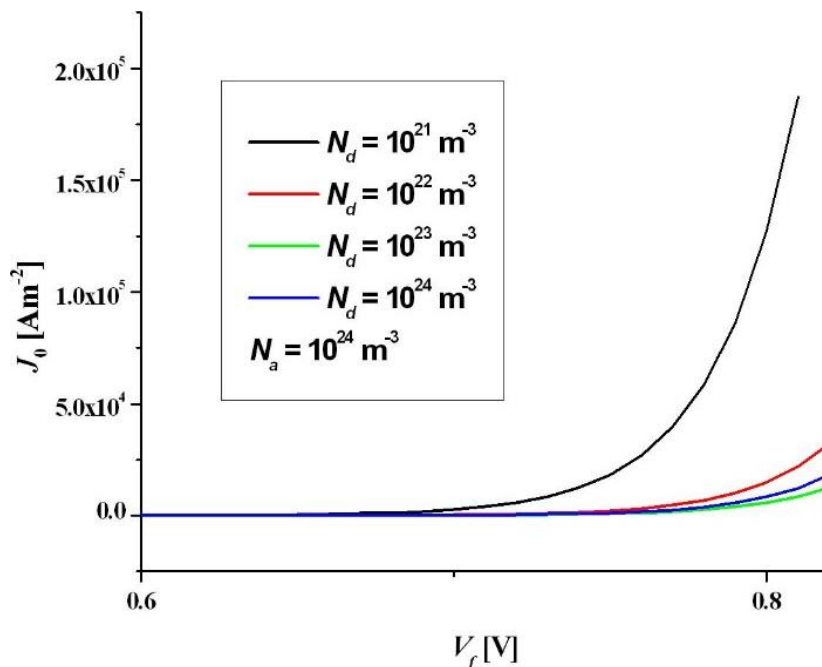


Fig. 5.18 Dark current as a function of applied voltage at different doping concentrations. N_a is fixed at 10^{24} m^{-3} .

5.7 Concluding Remarks

The influence of four parameters, namely, radiator material, cell material, cell thickness and doping concentration on the responses and performance of nano-gap TPV devices has been analysed in this chapter. This information may come in handy when designing nano-gap TPV power generators. It has been discovered that the most desirable radiator material would be one that possesses a high GE value and also supports surface polaritons of the same kind and spectrum as the TPV cell material (receiver). Furthermore, a TPV cell's internal quantum efficiency is mostly determined by its electrical properties and to a certain extent, its thickness. A high-performance cell should exhibit low surface recombination velocities, and high minority carrier diffusion coefficient and lifetime values. With regards to the thermal response, a constant temperature rise can be assumed for TPV cells which are sufficiently thin. We then studied the doping-dependence of a nano-gap TPV device that uses a *p-on-n* Si TPV cell. The optical response of the device depends very much on the doping concentration of the TPV cell. At high N_a values, the optical response is less sensitive to the change in N_a . It is also discovered that the lowest donor concentration in the absorber region may not necessarily produce the best results despite the greater diffusion length. Increasing the doping concentration also reduces the generation of dark current provided that the minority carrier lifetime is not too low.

Chapter 6 Indium Tin Oxide-Based Selective Radiator for Nano-Gap Thermophotovoltaic Applications

Nano-gap TPV systems have many advantages over their solar energy counterparts but their effectiveness is hampered by low conversion efficiencies [15]. One way to improve efficiency is to focus radiative heat flux onto a narrower spectrum. Ideally, the heat flux should be monochromatic at a frequency matching the band gap of the thermophotovoltaic cell. Thus, a radiator whose emission spectra can be easily tuned is crucial in the design of high-efficiency TPV systems. In this chapter, we will be focusing on the plasmonic material: indium tin oxide (ITO). Because it is transparent in the visible region and conducts electricity, it is commonly used as a transparent conductive coating, e.g. as the front contact on PV cells. In TPV applications however, the focus is on the infrared region where ITO has increased opacity and exhibits some interesting properties. It has a relatively low plasma frequency, allowing it to support surface plasmon-polaritons (SPP) in the infrared region [105]. Under the right circumstances, a heat flux enhancement which occurs at the resonant frequency can be generated. The plasma frequency of ITO is also highly tuneable. It has been shown that varying the percentage of tin, Sn in ITO allows one to alter its plasma frequency [106]. Furthermore, ITO properties can also be tuned by altering the preparation conditions [107]. Varying the porosity of ITO is another way to tune its properties. This technique has been applied to another plasmonic material, gold [108] and could potentially be applied to ITO as well.

In the literature, ITO's potential as a plasmonic radiator in the near-field regime has been investigated. Ilic et al. [109] simulated the near-field heat transfer between a bulk ITO radiator and a low band-gap TPV cell (InAs). They chose to use ITO with 45% tin doping in order to obtain a lower plasma frequency to match the band gap of the cell. They achieved PV power of 34 Wcm^{-2} and a conversion efficiency of 45% at a radiator temperature of 1200 K. Chang et al. [110] used ITO nanowires as hyperbolic metamaterial (HMM) radiators which allow the propagation of evanescent waves without much losses thus allowing for greater heat transfer. They demonstrated that the heat transfer between two nanowire arrays exceeds that between two ITO bulks. Boriskina et al. [79] investigated the near-field heat transfer between films of plasmonic materials including ITO. They showed that plasmonic films are superior to silicon carbide (SiC) films with optimized thicknesses. They proceeded to study the radiative heat transfer profile between hybrid multi-layered stacks which consist of ITO, SiC, MgF_2 , and SiO_2

arranged in a specific order with varying thicknesses. They were able to obtain multiple resonant peaks using this configuration taking advantage of both SPPs and SPhPs.

It has also been shown that multi-layered radiators are capable of increasing heat transfer at frequencies near the band gap. Narayanaswamy et al. [57] proposed a multi-layered radiator design that consists of alternating layers of tungsten (or silver) and a low-loss dielectric (e.g. alumina). They demonstrated that the multi-layered structure is able to achieve greater emissivity compared to bare tungsten. Furthermore, the spectral profile of emissivity can be altered to a certain degree by varying the thickness of the dielectric layers. Yang et al. [56] applied the same structure to a nano-gap TPV application. They reported increased heat flux as compared to a bulk tungsten radiator albeit with lower conversion efficiencies.

In this chapter, through the use of numerical simulation, we study a two-layer radiator which consists of an ITO thin film paired with an emitting substrate material. Two ITO processing techniques are explored, namely the BK7 glass and the sol-gel methods which provide a way to tune the ITO SPP's resonant frequency in order to increase the power output and conversion efficiency of nano-gap TPV systems. Several substrate materials and the effects of their thicknesses are considered as well by analysing their impact on the optical response of the whole system. Finally, the performances of several nano-gap TPV configurations are computed and discussed.

The bulk of this chapter was published in the *Journal of Nano Research* and can be found in [111].

6.1 Surface Polaritons

It has been shown that surface polaritons such as SPPs and SPhPs increase the local density of electromagnetic states (LDOS) within the vicinity of the interface upon which they propagate [52,56,60,61]. This subsequently can enhance heat transfer in the near-field regime. Moreover, the heat flux enhancements formed by SPPs occur over a narrower spectrum, causing them to be quasi-monochromatic. All these features of SPPs make them crucial in designing selective radiators.

As mentioned in the introduction to this chapter, ITO supports SPPs in the infrared region. If ITO is bordered with a metal, SPPs only exist at frequencies between the plasma frequencies of both materials, where their ϵ_r' (real part of the dielectric function) values are of opposite signs [112]. If for example, a thin ITO film is sandwiched by a metal and vacuum, the SPPs generated at each interface will not couple, due to the difference in frequency. In our case, this would prove beneficial; because if the ITO film were submerged in vacuum, SPPs of both interfaces would couple, causing the single SPP dispersion curve to split into two modes [113,114]. If the two modes are far enough apart in terms of their asymptotic frequencies, the heat flux enhancement would split in two with both modes having a weaker heat flux value compared to the single mode (single interface). However, if multiple modes can be generated at the same resonant frequency, the heat flux enhancement should be greater [80].

6.2 System Configuration and Simulation Parameters

Based on Fig. 6.1, the radiator consists of a bulk material (substrate) with a thin layer of ITO deposited on it. The radiators and the TPV cell are separated by a 10-nm vacuum gap as done in Chapter 5. Similarly, the *p*-type region has a thickness of 0.4 μm with a doping level, N_a of 10^{19} cm^{-3} while the *n*-type region is 10- μm thick with a doping level, N_d of 10^{17} cm^{-3} . Again, these values are taken from [33]. As shown in Fig. 4.3, the TPV cell is discretised into nodes (each node being the centre of a control volume) at which quantities like monochromatic radiative heat flux and minority carrier concentration are computed. The *p*-type region has 401 nodes while the *n*-type region has 801 nodes which yield a total of 1201 nodes as both regions share the same node at their boundary (grid A). The bulk and film radiator temperatures, T_0 and T_1 are assumed to be 1000 K (below the melting points of the radiator materials) while the cell temperature is kept at 300 K.

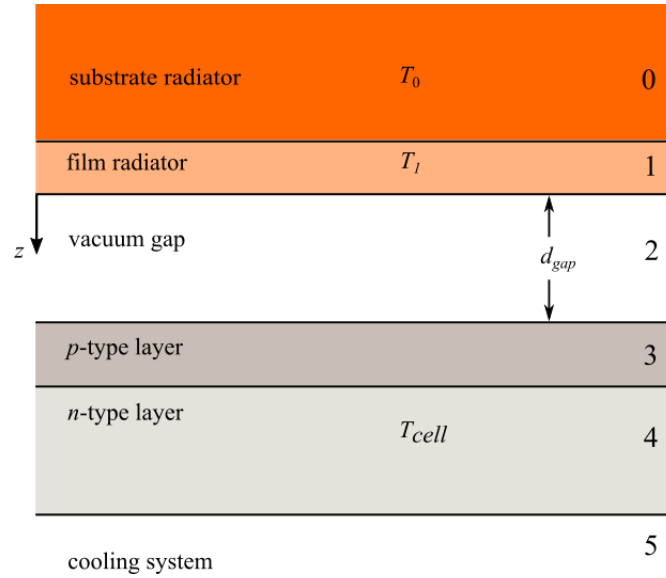


Fig. 6.1 Schematic diagram of a nano-gap TPV device.

Multiple radiator materials are included in this chapter. The dielectric function of tungsten, W and silicon carbide, SiC are taken from [89], silver, Ag from [115] (Appendix A) and finally ITO from [107]. The TPV cell material is indium gallium antimonide ($\text{In}_{0.18}\text{Ga}_{0.82}\text{Sb}$) whose dielectric function is modelled using Adachi's model [90] as done in [60] using the parameters provided in [95] along with a bowing constant of 0.42 when using Vegard's law. Its electrical properties, diffusion coefficients, lifetimes and surface recombination velocities are based on the work done in [60] and [95]. The doping dependence of the dielectric function of $\text{In}_{0.18}\text{Ga}_{0.82}\text{Sb}$ is not included due to insufficient data.

6.3 Indium Tin Oxide

In this section, two types of ITO processing techniques are compared, namely the BK7 glass and the sol-gel (SG) methods. Table 6.1 shows the Drude parameters used to model both types of ITO. Using these parameters, their dielectric functions, SPP dispersion relations ($\Gamma = 0$) and radiative heat flux spectra are modelled. The variation between the two dielectric functions is shown in Fig. 6.2.

Table 6.1 Drude model parameters for two types of ITO materials.

Parameters	BK7 glass [105]	Sol-gel [107]
ω_p (eV)	2.19	1.57882
Γ (eV)	0.111	0.17618
ε_∞	3.8	3.8375

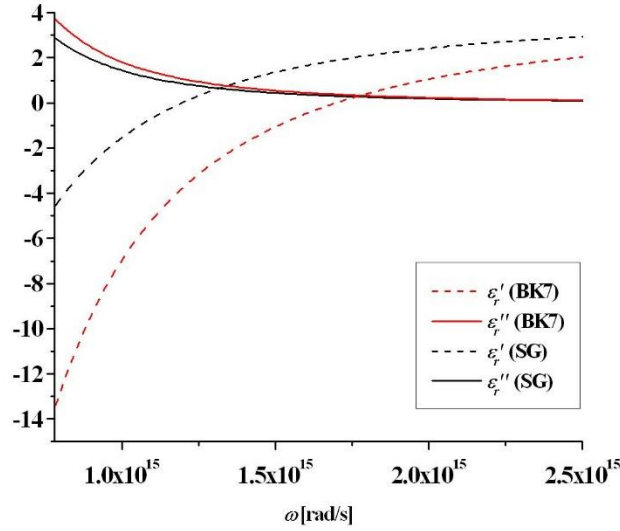
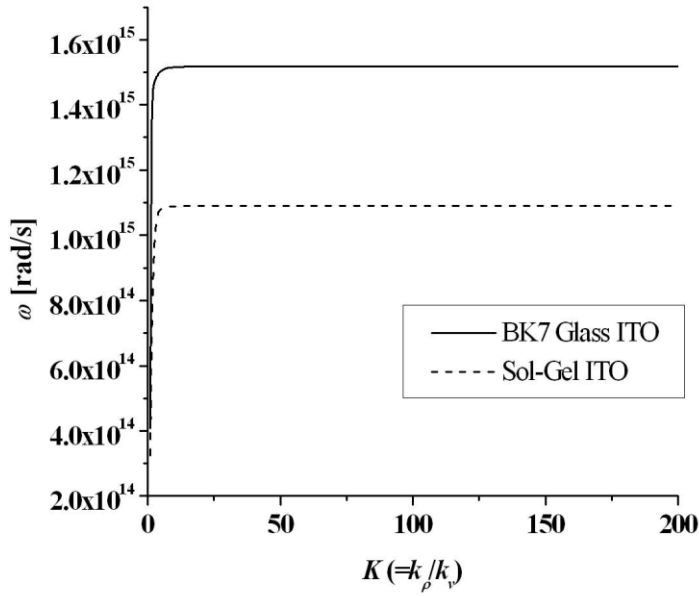


Fig. 6.2 Dielectric function of BK7 glass and sol-gel ITO.

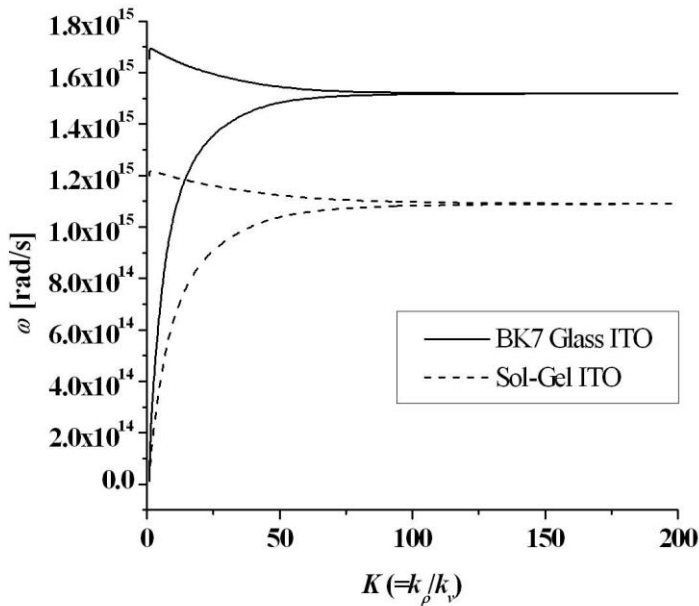
6.3.1 Bulk ITO

The dispersion relation curve (frequency as a function of normalized wavevector) of SPPs at the interface between ITO and vacuum in Fig. 6.3(a) is analysed. The dispersion relation curve reaches an asymptote when ε_r' of ITO is negative one. This condition can be used to calculate the frequency where the heat flux is enhanced by resonant SPPs. ITO is modelled using the Drude model, thus, by setting $\varepsilon_r' = -1$ and assuming that damping is zero, the resonant frequency is:

$$\omega_{res} = \frac{\sqrt{4\left(\frac{\omega_p^2}{\varepsilon_\infty + 1}\right)}}{2} \quad (6.1)$$



(a)



(b)

Fig. 6.3 Dispersion relation curve of SPPs (a) at an ITO/vacuum interface and (b) within an ITO film in vacuum.

The asymptotic frequency corresponds to the resonant frequency where a noticeable heat flux enhancement exists. Using Eq. (6.1), the resonant frequency for BK7 glass ITO is calculated to be around 1.5×10^{15} rad/s which matches the heat flux enhancement shown in Fig. 6.4 (see the ‘hump’ on the downward slope). However, it can be seen that the heat flux at resonant frequency is not the maximum heat flux. This is due to the influence of the mean energy of a

Planck oscillator, Θ which is used in Eqs. (4.2) and (4.30). As shown in Fig. 6.5, the mean energy decreases as frequency increases, thus at high frequencies, the SPP-induced heat flux enhancement is hardly significant due to low Θ values.

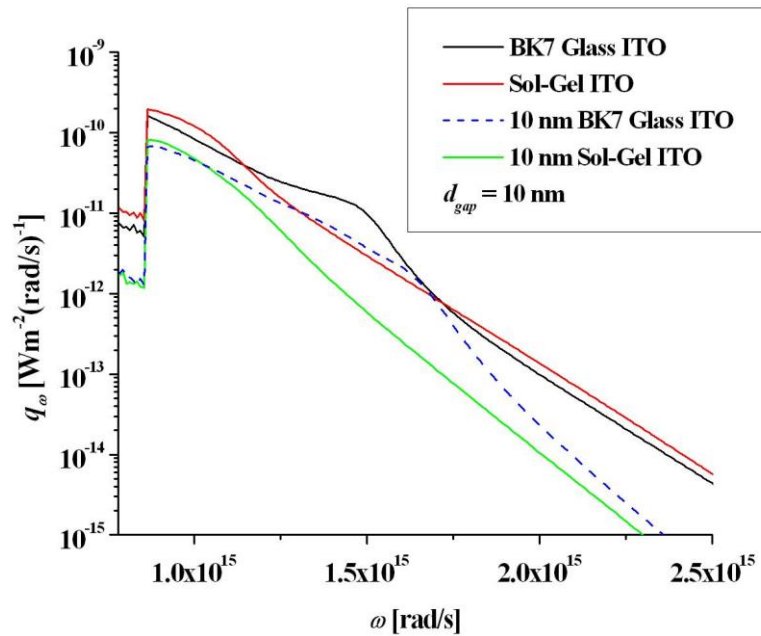


Fig. 6.4 Monochromatic radiative heat flux of bulk and film ITO radiators (1000 K) on the surface of the TPV cell (300 K) for both BK7 glass and sol-gel methods.

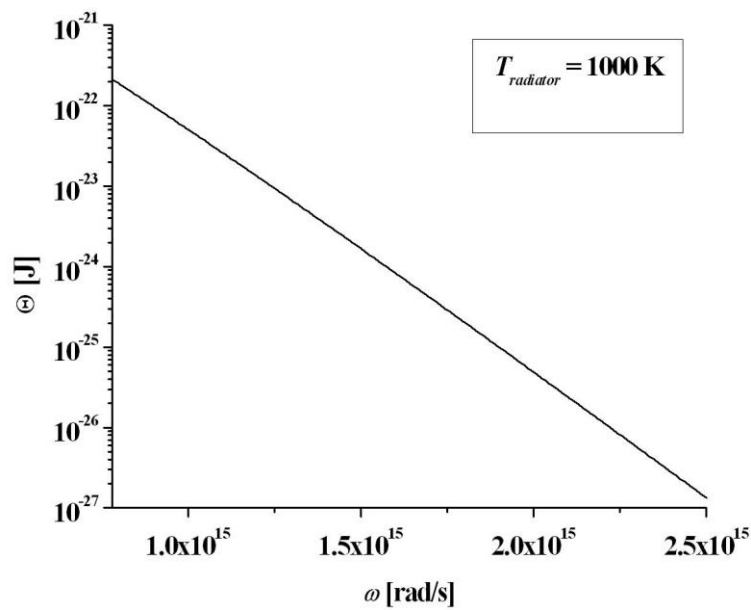


Fig. 6.5 Mean energy of a Planck oscillator as a function of frequency.

The results of sol-gel ITO can be explained in the same way. The resonant frequency of a bulk sol-gel ITO radiator is 1.09×10^{15} rad/s which is noticeably lower than BK7 glass ITO. As shown in Fig. 6.2, the lowering of the plasma frequency of the ITO radiator (by changing the processing method from BK7 glass to sol-gel) shifts the dielectric function curves to the left causing the resonant frequency of SPPs to shift towards lower frequency values. This in turn causes the heat flux enhancement to occur at lower frequencies where the mean energy is greater. This shows that changing the processing technique can be used to tune the resonant frequency to match the band gap of a TPV cell.

6.3.2 Film ITO

Based on Fig. 6.3(b), when ITO is a 10-nm thin film, the dispersion relation curve splits into two modes due to the coupling between SPPs at the top and bottom interfaces. This results in the heat flux enhancement at resonant frequency becoming less prominent. The thinner ITO layer also generates less heat flux overall.

In order to prevent SPP coupling between the two interfaces of an ITO film, it is proposed that a substrate material be added upon which the ITO film is deposited as shown in Fig. 6.1. The TPV cell material of $\text{In}_{0.18}\text{Ga}_{0.82}\text{Sb}$ has a band gap of around 8.575×10^{14} rad/s. Thus, sol-gel ITO is chosen as the ITO radiator in Section 6.4 due to its lower plasma frequency. Sol-gel ITO will henceforth be referred to as ITO in that section for the sake of convenience.

6.4 Optical Response of the Nano-Gap TPV System

6.4.1 Substrate-ITO Radiators

The heat flux spectra of three substrate-ITO combinations are modelled and compared with the spectrum for bulk W. The three arbitrarily chosen substrate materials are Ag, W and SiC. This section aims to find out how different substrate materials affect the heat flux spectrum when paired with an ITO film. The radiator and TPV cell temperatures are kept at 1000 K and 300 K respectively.

As can be seen from Fig. 6.6, the W-ITO and SiC-ITO combinations produce the most heat flux across the spectrum while the Ag-ITO combination yields a maximum heat flux comparable to the other two but which exists within a narrower frequency range. High heat flux within a narrow spectrum is highly favourable in our quest to achieve a higher conversion efficiency without compromising too much on maximum power output. The sharp drop in heat flux and its oscillatory behaviour below the band gap of 8.575×10^{14} rad/s can be attributed to low optical absorption in the cell.

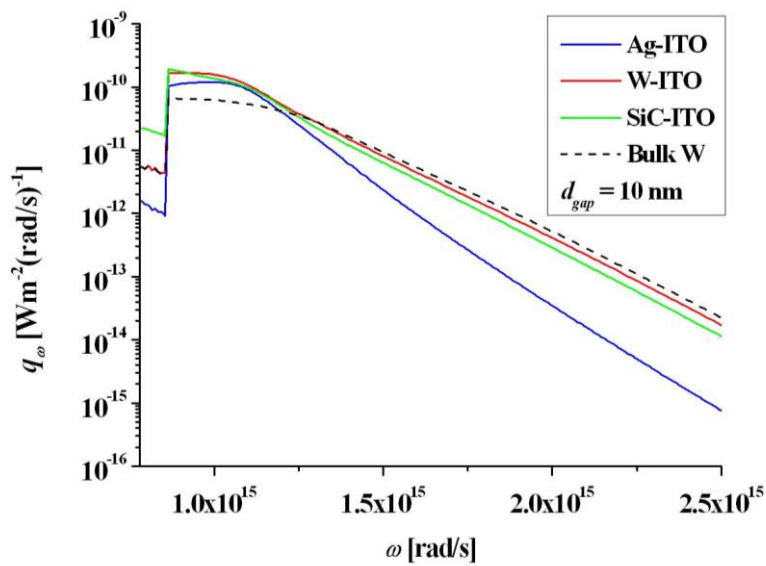
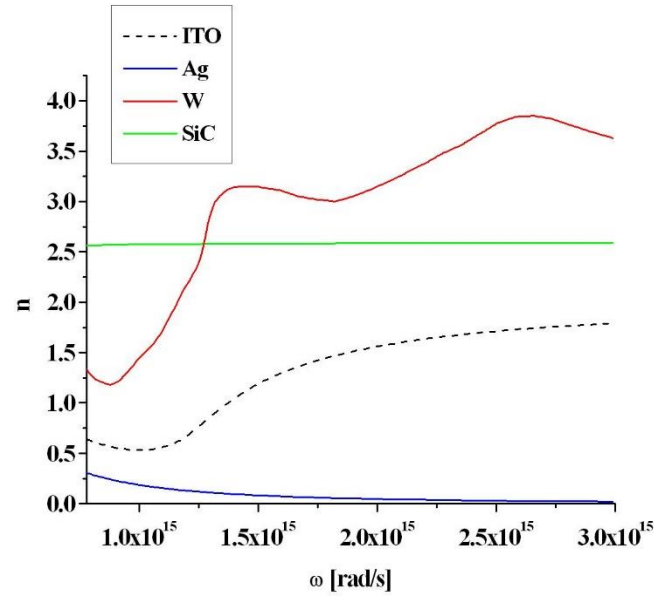
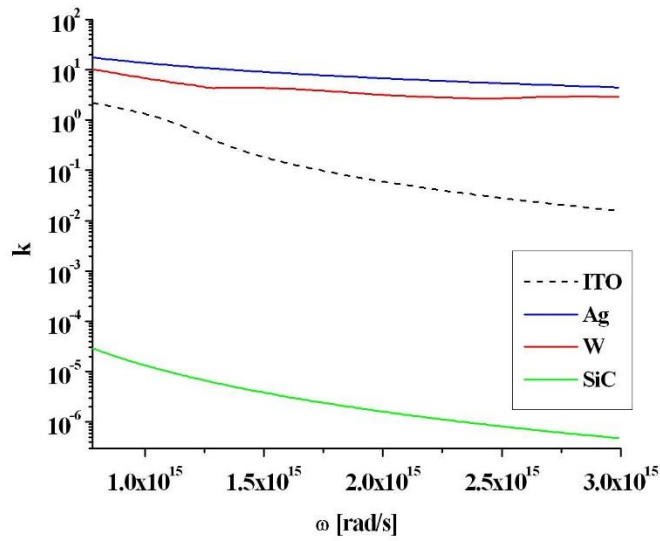


Fig. 6.6 Monochromatic radiative heat flux of various radiator configurations at 1000 K on the surface of the TPV cell.

Referring the Fig. 6.7, Ag has the lowest refractive indices (real part), \mathbf{n} compared to the other two substrate materials and high extinction coefficients, \mathbf{k} comparable to W. It would seem that the most suitable substrate material should exhibit lower \mathbf{n} values which should produce lower ϵ_r' and ϵ_r'' values (real and imaginary parts of the dielectric function).



(a)

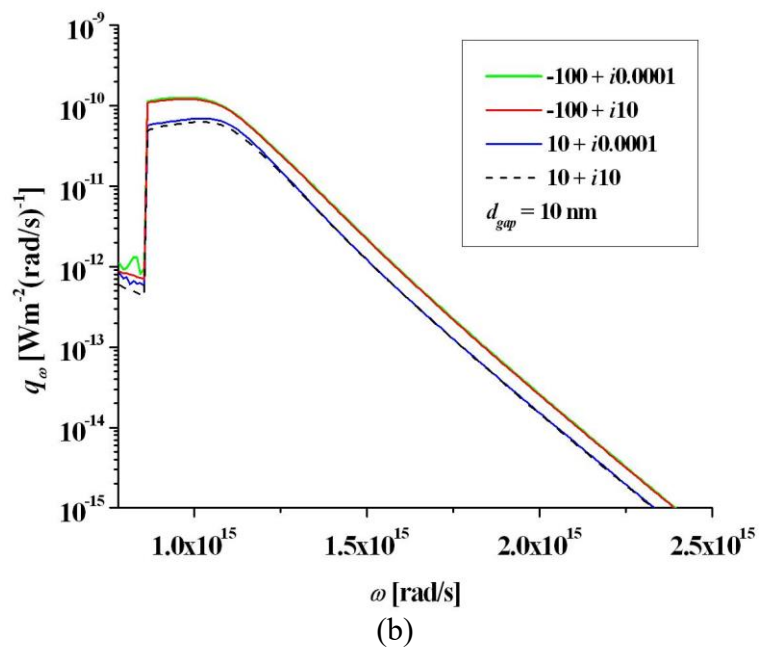
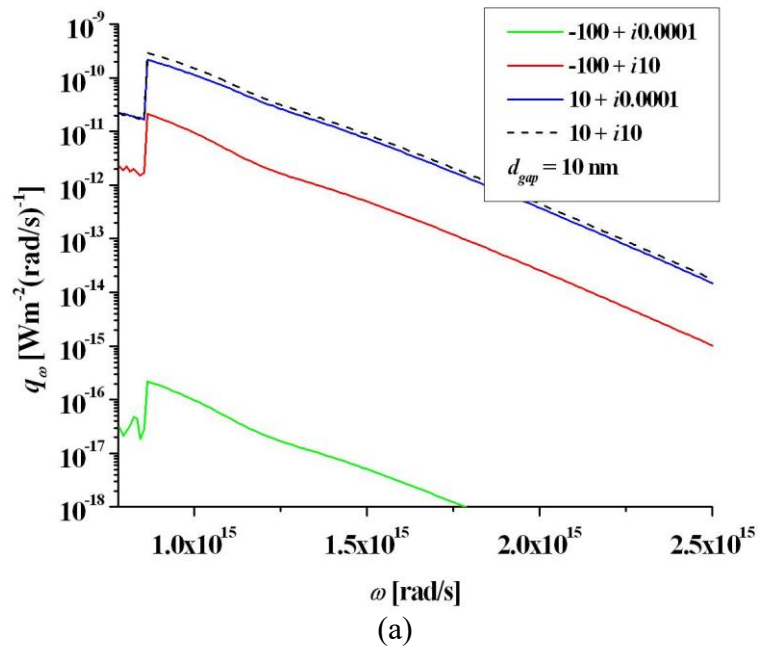


(b)

Fig. 6.7 (a) Refractive indices and (b) extinction coefficients of various materials.

In order to pursue this further, four different artificial substrate materials were paired with ITO and the results are shown in Fig. 6.8. Each artificial substrate has a constant dielectric function which differs from the rest. Based on Fig. 6.7 and Fig. 6.8, we could conclude that a substrate radiator with smaller n and low k values would produce the most desirable results (sufficiently high heat flux within a narrow spectrum). In terms of the dielectric function, the material should have a large negative ϵ_r' and a very small ϵ_r'' (low absorption). This will reduce the contribution from the substrate and maximize the contribution of ITO at the resonant frequency. A narrow overall spectral heat flux profile is mainly due to the contribution from ITO. If however, the

goal is to maximize heat flux at all costs, then greater ϵ_r' and ϵ_r'' values would be necessary in order to increase the heat flux emitted at all frequencies at the expense of efficiency. It has to be noted that these results only apply to the specific configuration described in this chapter where $d_{gap} = 10$ nm.



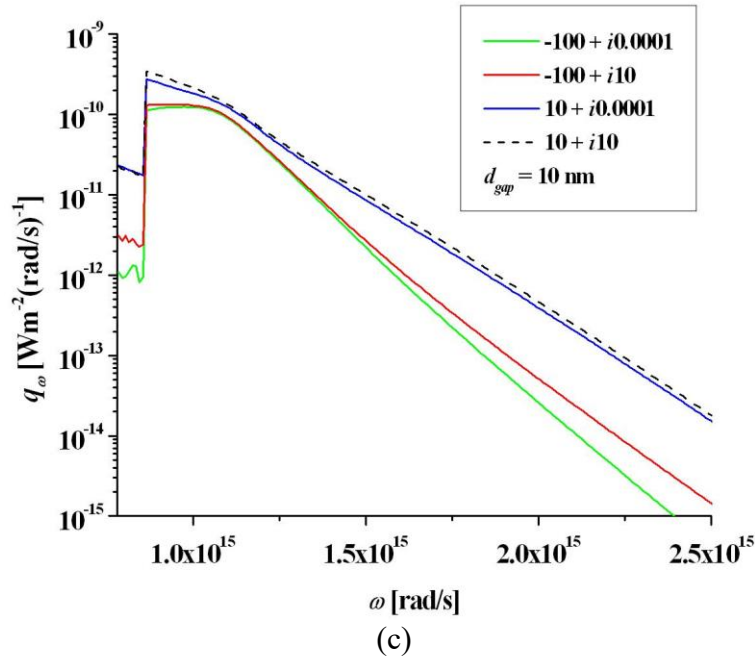


Fig. 6.8 Monochromatic radiative heat flux contributions from the (a) artificial substrate material (each represented by a different constant dielectric function), (b) ITO film and (c) the sum of both contributions.

6.4.2 Thickness Effects

In this section, a slightly different nano-gap TPV configuration is used. The goal here is to observe how changing the thickness of the radiator layer adjacent to the ITO layer affects the optical response of the system. Thus, the bulk substrate radiator (layer 0 in Fig. 6.1) is modelled as a film as shown in Fig. 6.9. Layer 0 is now assumed to be vacuum while the TPV cell is modelled as a single layer in order to simplify the heat transfer problem. The vacuum substrate (layer 0) can be replaced with alumina (Al_2O_3) when designing real devices as its optical response is very much like vacuum at most frequencies [116]. The thicknesses of the substrate materials in Section 6.4.1, which are now treated as film radiators (layer 1), are varied and their effect on the heat flux spectral profile is presented. Do note that the ITO layer remains unchanged. The temperatures of the radiators and TPV cell remain at 1000 K and 300 K respectively.

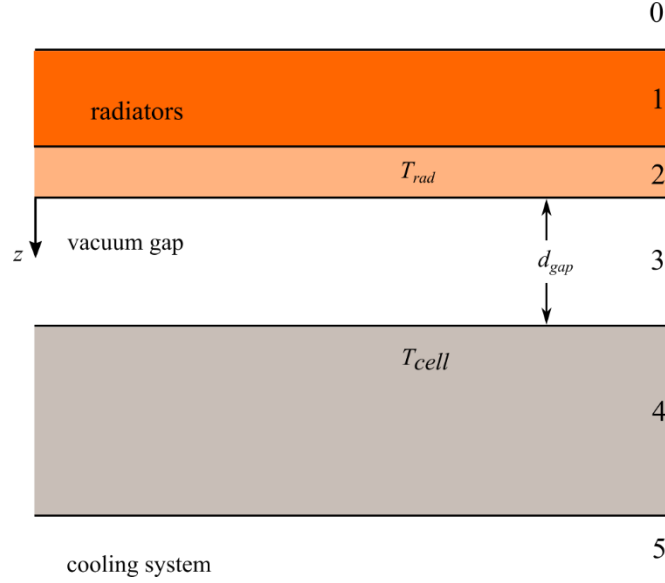


Fig. 6.9 Schematic diagram of a 2-film radiator nano-gap TPV system.

An explicit analytical expression for the monochromatic radiative heat flux emitted by a two-film radiator on the surface of the TPV cell is presented here to facilitate the analysis of two-film radiators. The analytical expression for a bulk radiator is acquired from [26] while the effective transmission and reflection coefficients (T_n^γ and R_n^γ) for multi-layered radiators are derived based on the work done in [79]. R_4^γ in Eqs. (6.2) and (6.3) has the same general form as R_1^γ . The Fresnel coefficients are taken from [65].

$$q_\omega^{prop}(z_4^+) = \frac{\Theta(\omega, T_{rad})}{4\pi^2} \int_0^{k_y} k_\rho dk_\rho \sum_{\gamma=TE, TM} \frac{(1 - |R_2^\gamma|^2 - |T_2^\gamma|^2)(1 - |R_4^\gamma|^2)}{|1 - R_2^\gamma R_4^\gamma e^{2ik_{z3}d_{gap}}|^2} \quad (6.2)$$

$$q_\omega^{evan}(z_4^+) = \frac{\Theta(\omega, T_{rad})}{\pi^2} \int_{k_v}^\infty k_\rho dk_\rho e^{-2k_{z3}^* d_{gap}} \sum_{\gamma=TE, TM} \frac{\text{Im}(R_2^\gamma) \text{Im}(R_4^\gamma)}{|1 - R_2^\gamma R_4^\gamma e^{-2k_{z3}^* d_{gap}}|^2} \quad (6.3)$$

$$T_2^\gamma = \frac{t_{3,2}^\gamma T_1^\gamma e^{2ik_{z2}t_2}}{1 + r_{3,2}^\gamma R_1^\gamma e^{2ik_{z2}t_2}} \quad (6.4)$$

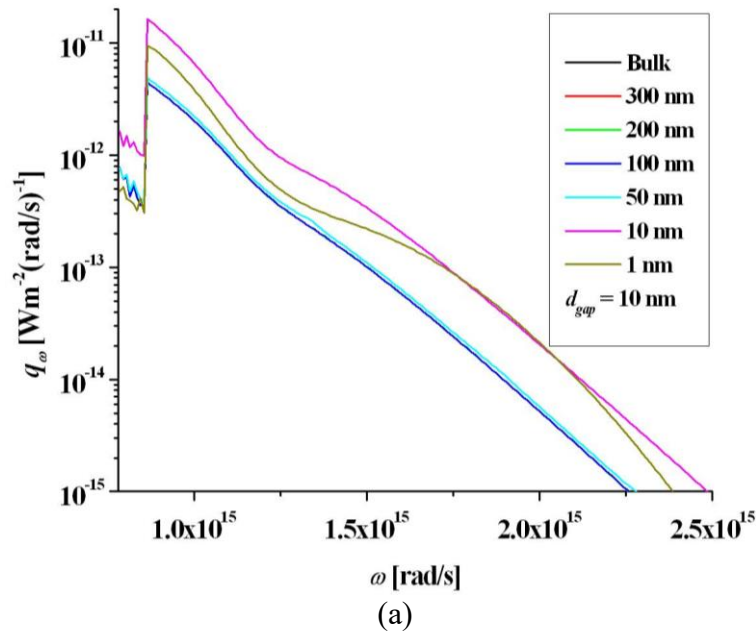
$$T_1^\gamma = \frac{t_{2,1}^\gamma t_{1,0}^\gamma e^{2ik_{z1}t_1}}{1 + r_{2,1}^\gamma r_{1,0}^\gamma e^{2ik_{z1}t_1}} \quad (6.5)$$

$$R_2^\gamma = \frac{r_{3,2}^\gamma + R_1^\gamma e^{2ik_{z2}t_2}}{1 + r_{3,2}^\gamma R_1^\gamma e^{2ik_{z2}t_2}} \quad (6.6)$$

$$R_1^\gamma = \frac{r_{2,1}^\gamma + r_{1,0}^\gamma e^{2ik_z t_l}}{1 + r_{2,1}^\gamma r_{1,0}^\gamma e^{2ik_z t_l}} \quad (6.7)$$

The monochromatic radiative heat flux on the surface of the TPV cell is calculated using Eqs. (6.2) through (6.7). The thickness of the top emitting film, t_l is the parameter in question. As t_l decreases, the exponential terms in R_1^γ increase, magnifying the effect of the top interface (between vacuum and the top radiator) upon the system. When t_l is infinity, the exponential terms become zero, causing the top interface to lose all influence on the system.

Based on Fig. 6.10, the heat flux contribution of the Ag film remains the same as bulk Ag as its thickness is reduced to 300 nm. Below that thickness, the total heat flux increases albeit in negligible amounts. Significant differences appear at thicknesses of 10 nm and below. At around 5 nm, the heat flux contribution from both Ag and ITO are the greatest. As the thickness of Ag is reduced further, the contribution from ITO suffers at most frequencies. In summary, as Ag thickness decreases, the heat transfer between the radiator and the TPV cell increases up to a certain optimal thickness below which overall heat transfer starts to decline.



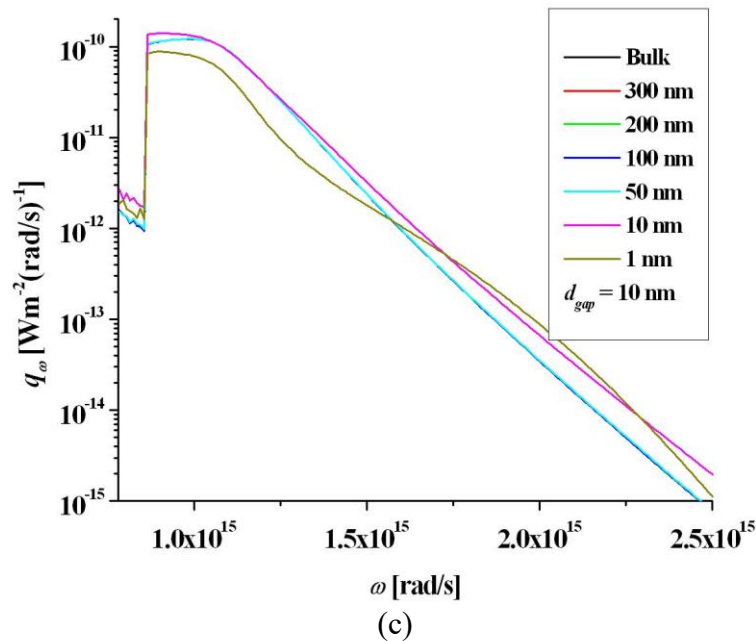
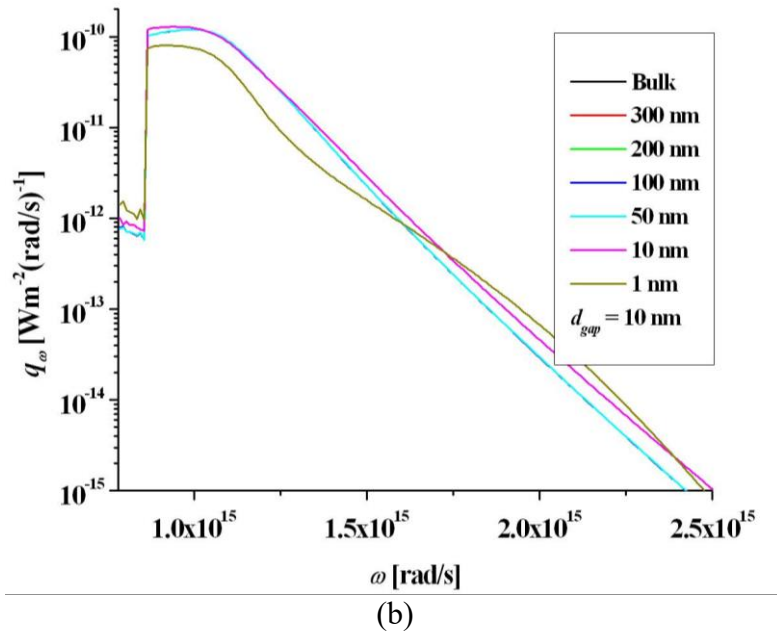
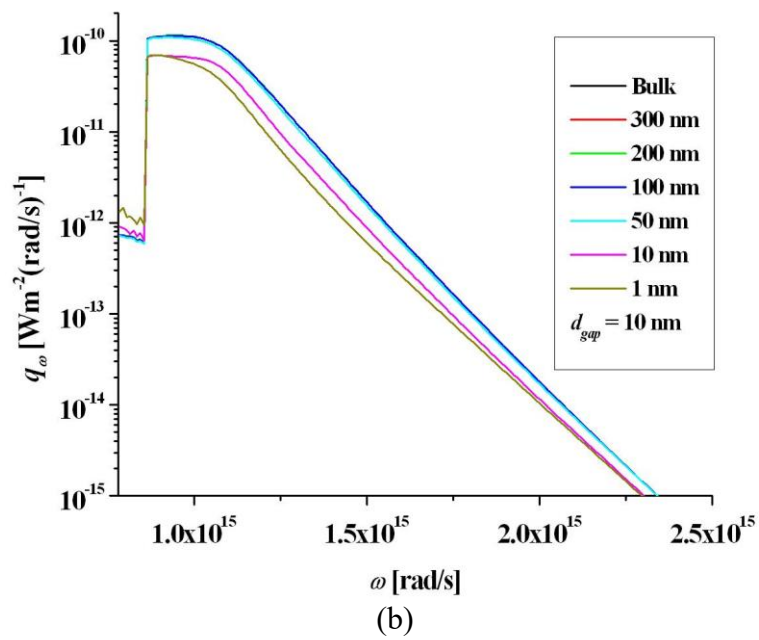
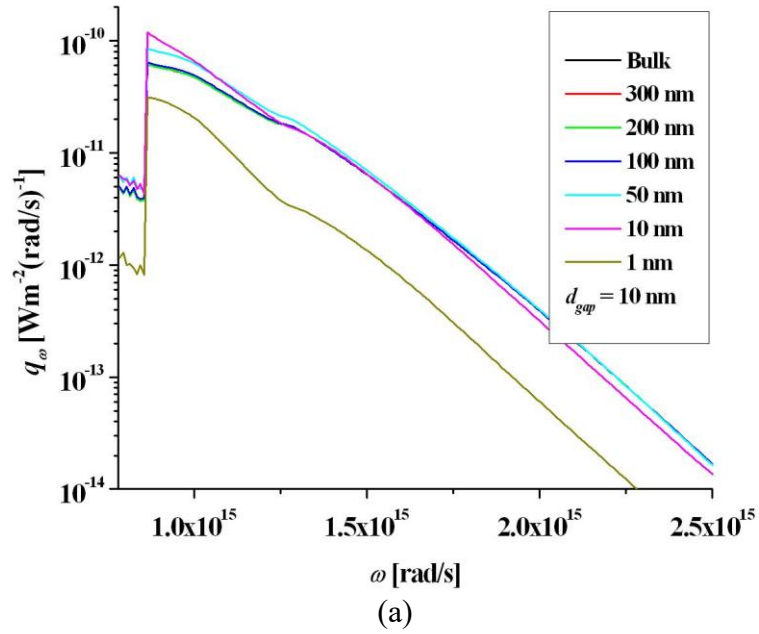


Fig. 6.10 Monochromatic radiative heat flux contributions from (a) Ag, (b) ITO and (c) the total sum of both contributions at various Ag thicknesses.

The W layer exhibits a similar trend to Ag as shown in Fig. 6.11. The profiles of bulk W down to a thickness of 300 nm are largely the same with changes occurring below that thickness. However, the change in the profile only becomes noticeable below 100 nm. The maximum total heat flux occurs at around 20 nm mainly due to the contribution from W as the contribution from ITO decreases as W thickness decreases. Below 20 nm, contribution from both W and ITO experience declines causing overall heat transfer to suffer. However, despite lower heat

flux values, narrower spectral profiles are produced, which could allow for greater conversion efficiencies.



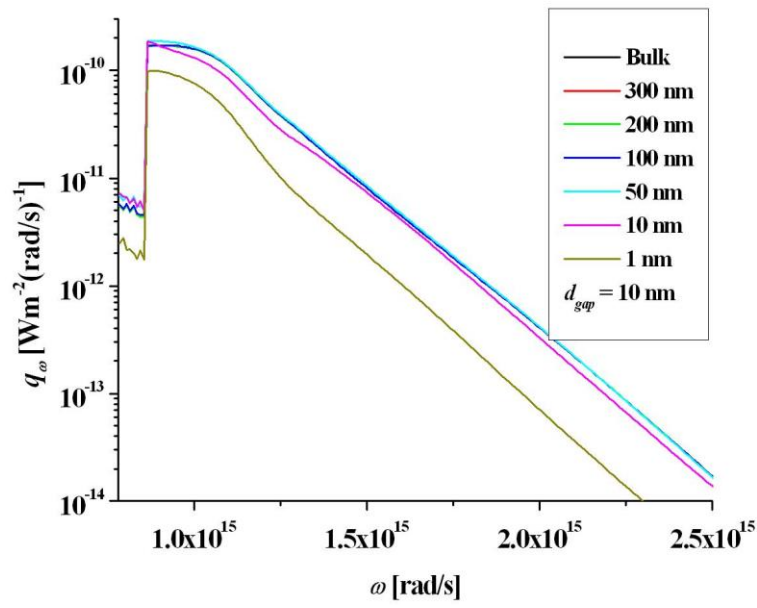
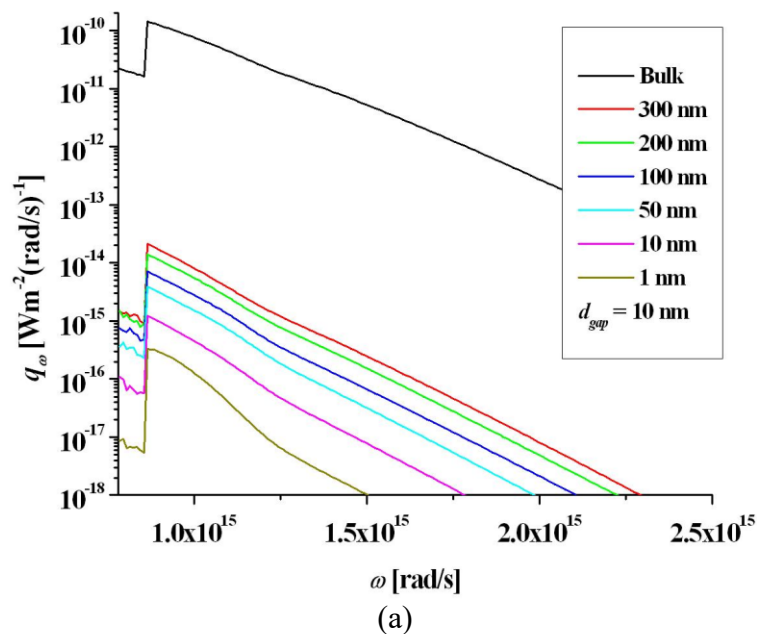


Fig. 6.11 Monochromatic radiative heat flux contributions from (a) W, (b) ITO and (c) the total sum of both contributions at various W thicknesses.

As shown in Fig. 6.12, SiC exhibits a different trend as compared to the two metals. The total heat flux contribution from the two-layer radiator decreases as SiC thickness decreases. However, at thicknesses below 10 nm, SiC's effect on the system dwindles as it behaves more and more like a vacuum layer causing the profile to match the heat flux spectrum of a thin-film ITO radiator suspended in vacuum.



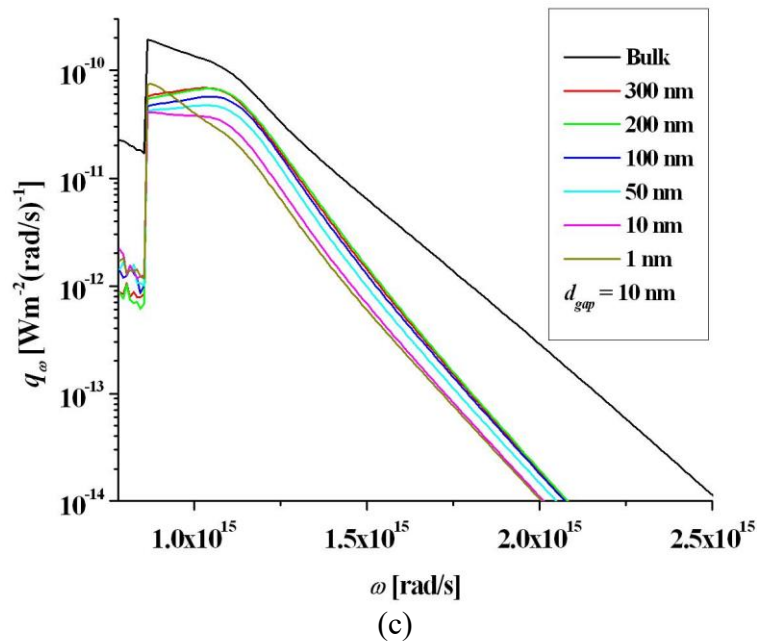
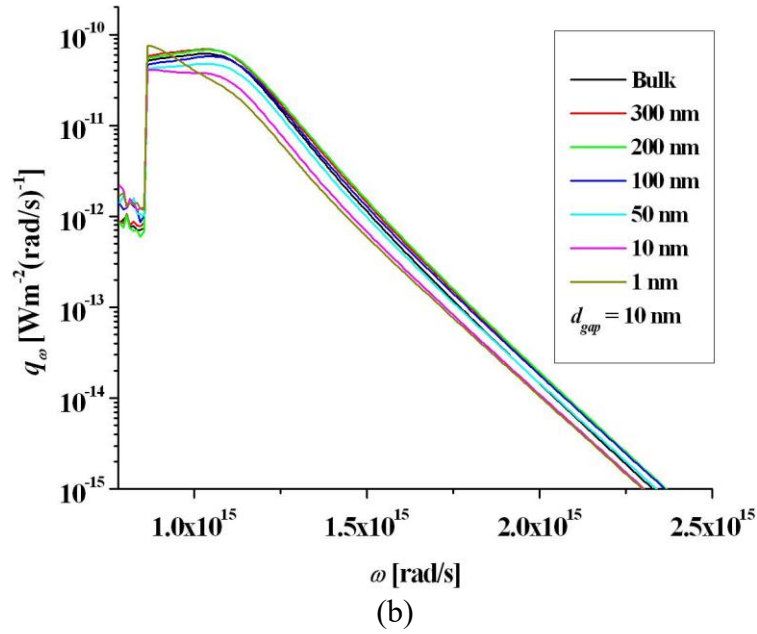


Fig. 6.12 Monochromatic radiative heat flux contributions from (a) SiC, (b) ITO and (c) the total sum of both contributions at various SiC thicknesses.

Based on the analysis done on the effect of the thickness of layer 1, several suggestions could be made. Due to the fact that the main contributor is ITO in the Ag-ITO configuration, it is therefore unnecessary for Ag to be a bulk layer. Reducing the thickness of the Ag layer down to 300 nm does not change the heat flux spectrum. Furthermore, a thinner layer 1 may make manufacturing more economical as less material is needed. In regards to the W-ITO

combination, if the goal is to achieve greater heat transfer between the radiators and the TPV cell, the thickness of W should remain in the hundreds of nanometres. If however, conversion efficiency is an issue, a thinner W layer would be advisable. Finally, SiC does not provide much positive contribution making it unattractive as a material for layer 1.

6.5 Performance of Nano-Gap TPV Systems with ITO-Based Radiators

The performance of nano-gap TPV systems using ITO-based radiators is examined and compared to systems that use bare Ag (a relatively low-loss medium) and W (bulk) (commonly used in the literature) radiators. The first set of configurations uses a bulk Ag substrate paired with two different ITO films made using the BK7 glass technique and the sol gel method respectively (the same result can be obtained with a 300-nm Ag film) at 1000 K (below the melting point of Ag). The second uses a W (bulk)-ITO (the same two processing methods are used) configuration at 2000 K (the same temperature is used in [33]). A bare Ag-radiator system will be simulated at 1000 K and a W-radiator system at 2000 K.

Fig. 6.13(a) shows the heat flux spectrum of the configurations in question on the TPV cell surface as compared to the results of bare radiators. As mentioned throughout this chapter, the SPPs induced within the ITO radiators cause pronounced resonant heat flux enhancements which can be tuned by changing the material properties of ITO. By changing the processing technique from the BK7 glass technique to the sol gel method, the resonant enhancement is shifted towards lower frequency values, closer to the band gap of the TPV cell. The enhanced heat flux values are also greater than the heat flux values produced by bare radiators.

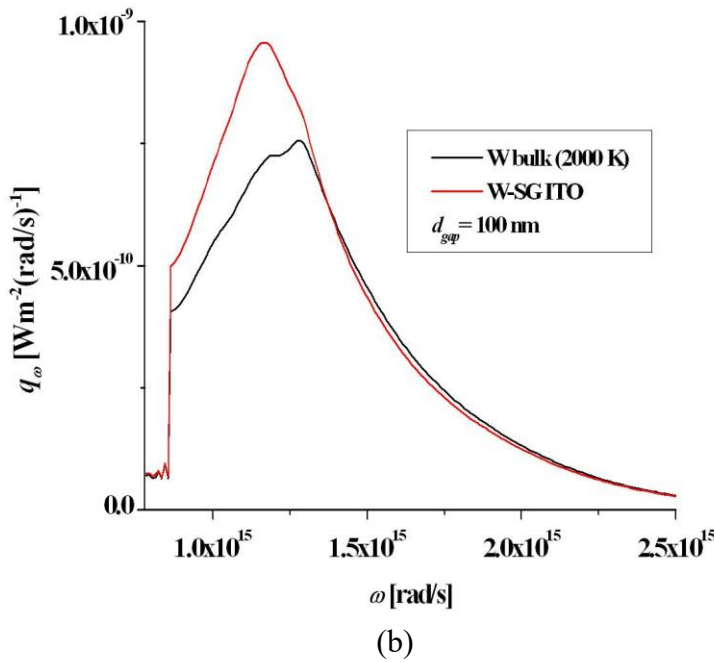
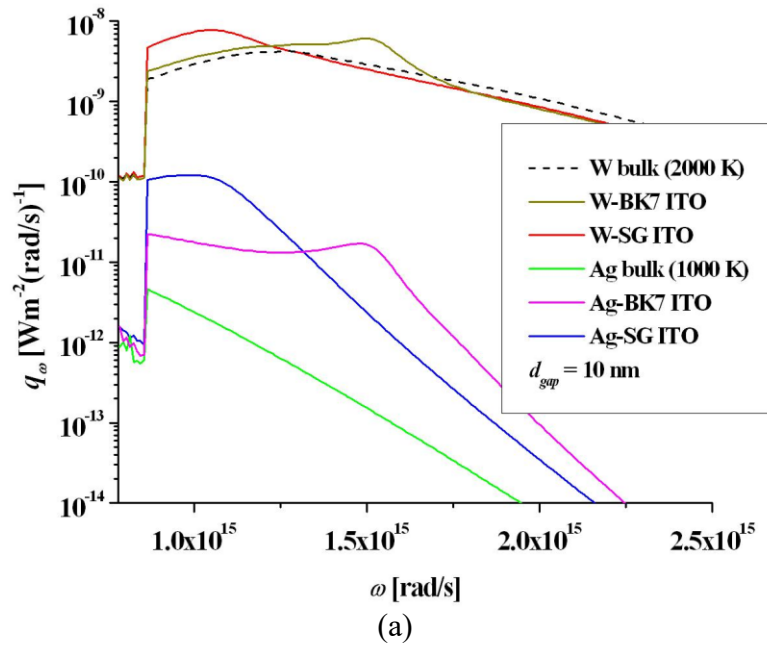


Fig. 6.13 Monochromatic radiative heat flux of various radiator configurations on the surface of the TPV cell at (a) $d_{gap} = 10$ nm and (b) $d_{gap} = 100$ nm. Do note that SG stands for sol gel.

In order to evaluate the performance even further, the conversion efficiencies of each configuration is calculated and presented in Table 6.2. Integration is done from the band-gap frequency, $\omega_g = 8.575 \times 10^{14}$ rad/s to 3.8×10^{15} rad/s. Absorption below the band gap is negligible and thus is neglected to reduce computation time.

Table 6.2 Conversion efficiencies of six nano-gap TPV systems ($d_{gap} = 10$ nm) along with their input and output power.

T_{rad}	Radiator	Input (W/m ²)	Output (W/m ²)	Conversion Efficiency (%)
1000 K	Bulk Ag	9.397×10^2	1.596×10^2	16.984
	Ag-BK7 ITO	1.197×10^4	1.999×10^3	16.703
	Ag-SG ITO	3.810×10^4	8.063×10^3	21.161
2000 K	Bulk W	3.527×10^6	9.648×10^5	27.353
	W-BK7 ITO	4.290×10^6	1.119×10^6	26.094
	W-SG ITO	4.430×10^6	1.245×10^6	28.115

Referring to Table 6.2, at $T_{rad} = 1000$ K, the bare Ag radiator produces the lowest output power with a conversion efficiency that is only slightly better than the Ag-BK7 radiator. On the other hand, both Ag-ITO radiators produce much greater output power. The Ag-SG radiator produces the most electrical power, approximately four times the value of the Ag-BK7 radiator. At $T_{rad} = 2000$ K, the bare W radiator outperforms the W-BK7 radiator in terms of efficiency but produces less output power. The W-SG radiator performs better than the other two configurations, achieving a greater conversion efficiency while producing an output power increase of about 29% over the bare W radiator. When comparing the two types of ITO radiators, it is clear that sol-gel ITO outperforms BK7 ITO in terms of conversion efficiency and power output. This is partly due to increased quantum efficiencies at frequencies closer to the band gap [33,60,88]. Moreover, heat flux values at lower frequencies are greater which in turn produce more output electrical power. This demonstrates the importance of tuning radiator properties to match the band gap of the TPV cell.

A similar trend can be observed when the gap size is increased to a more experimentally feasible size of 100 nm as shown in Fig. 6.13(b) and Table 6.3. It can be seen that the ITO-based radiator, W-SG continues to outperform the bare W radiator, yielding greater output power and conversion efficiency values. However, if the gap continues to widen beyond the near-field regime, the heat flux enhancement produced by the ITO layer should diminish causing the W-SG radiator to behave more like a bare W radiator.

Table 6.3 Conversion efficiencies of two nano-gap TPV systems ($d_{gap} = 100$ nm) along with their input and output power.

$T_{rad} = 2000$ K	Input (W/m ²)	Output (W/m ²)	Conversion Efficiency (%)
Bulk W	5.606×10^5	1.462×10^5	26.079
W-SG ITO	6.247×10^5	1.705×10^5	27.291

6.6 Concluding Remarks

A nano-gap TPV device that utilises an ITO-based radiator is proposed and analysed in this chapter. The possibility of tuning the material properties of ITO by changing the processing technique is explored. Furthermore, it has also been discovered that the heat flux spectrum of an ITO-based radiator can change dramatically based on the type of substrate material used. The thickness of the aforementioned substrate when treated as a film radiator has a significant effect on the heat flux spectrum especially at smaller thicknesses. Lastly, it has been proven that by tuning ITO properties to better match the TPV cell's band gap, greater output power and conversion efficiency values can be obtained.

When it comes to the practical feasibility of the thin films studied in this chapter, it is worth noting that a 10-nm-thick ITO film has been successfully fabricated [117]. The modelling of Ag, W and SiC films down to 1 nm on the other hand is unrealistic. However, the findings could prove useful as a reference to which experimental results could be compared to in order to observe how theoretical models such as the Drude model break down at smaller thicknesses.

Chapter 7 Application of Thin Films to Nano-Gap Thermophotovoltaics

As devices shrink in size, their properties and responses start to deviate from their bulk counterparts. The same goes with nano-gap TPV devices. The thicknesses of the radiator and the receiver have a huge bearing on the responses and performance of the device. Material models which describe bulk materials are insufficient to describe thin films ($\leq 1 \mu\text{m}$) due to the fact that bulk properties may differ greatly from thin-film properties [118], therefore it is necessary that numerical simulations involving thin films employ the use of phenomenological models extracted from thin-film experiments. The reduction in size also affects the interaction of waves in a nano-gap TPV system. Blandre et al. [119] have shown that when the thickness of the receiver is comparable to the dominant wavelength of the radiation, the spectral and spatial profiles of the emission become sensitive to the thickness.

A lot of work has been done on nano-gap TPVs, e.g. [33,54,56,109,120,121], but quite a number of them assume a constant, uniform TPV cell temperature, usually fixed at 300 K. However, in order to gain a greater understanding of nano-gap TPV operation, one has to include the thermal response of the system. Francoeur et al. [34] performed numerical simulations of a nano-gap TPV system based on the pairing of a bulk tungsten (W) radiator and a 10.4- μm -thick indium gallium antimonide (InGaSb) TPV cell. They found that as cell temperature increases, the conversion efficiency suffers due to lower open-circuit voltage, V_{oc} which comes as a result of increased dark current, J_0 . The total heat flux absorbed by the cell and the generated photocurrent, J_{ph} are less affected by changes in cell temperature.

They went on to perform simulations using various values of the convective heat transfer coefficient, h_{conv} . It was discovered that the temperature gradient generated within the cell is negligibly small ($\leq 0.5 \text{ K}$), thus they decided to use a single average temperature value to represent the temperature of the entire cell. Furthermore, at smaller gap distances between the radiator and the receiver, a greater h_{conv} is needed to maintain the cell temperature close to 300 K due to greater near-field radiative heat transfer which increases the amount of heat generated in the cell. Laroche et al. [31] discovered that for a near-field radiative heat flux of 10^6 Wm^{-2} , the maximum temperature difference achieved in a 300- μm gallium antimonide (GaSb) cell is 30 K. They deemed that to be insignificant, arguing for the use of a single temperature for the

entire cell. It has to be noted that the work done by Francoeur et al. and Laroche et al. use bulk radiators and cell thicknesses that allow the diffusive regime to dominate heat conduction. It would be interesting to know if the same trends are observed when thin films ($\leq 1 \mu\text{m}$) are used instead. At thicknesses comparable to the mean free path of phonons, heat conduction becomes semi-ballistic which may in turn affect the temperature profile in the material [122]. Phonon Monte Carlo (MC) studies done by Wong et al. [123] have shown that the temperature rise in insulated thin films of silicon caused by the absorption of near-field thermal radiation is uniform across the film. However, if a pulsed laser source with a much higher power density is used, temperature gradients start to emerge. Lau et al. [88] studied the temperature rise in insulated films of gallium arsenide as thin as $1 \mu\text{m}$. Similar conclusions were reached, namely that the heat generation caused by near-field thermal radiation absorption is not sufficient to cause a temperature gradient in thin films of GaAs.

In this chapter, the performance and responses of a thin-film nano-gap TPV device are analysed with the coupled electrical and thermal responses being of particular interest. By thin-film, it is meant that the radiator and the receiver thicknesses do not exceed $1 \mu\text{m}$ respectively. A thin-film W radiator on an alumina (Al_2O_3)/vacuum substrate is paired with a doped-Si TPV cell of variable thickness separated by a 50-nm vacuum gap. We are aware that Si is rarely used in TPV applications because of its relatively high band gap. However, the goal is not to propose the most efficient nano-gap TPV design but to capture trends that will provide further insight into the responses of thin-film nano-gap TPV devices. The properties of Si are well understood and documented with reliable models available, thus the use of Si would provide us with more quantitative confidence when analysing the responses of the TPV cell.

This chapter is broken down into multiple sections. In Section 7.1, the configuration and simulation parameters of a nano-gap TPV device are presented. The properties of the materials used in the device are then detailed in Section 7.2. In Section 7.3, the temperature-dependence of the nano-gap TPV device is analysed. Section 7.4 details how a thin-film W radiator compares to a bulk W radiator and is followed by Section 7.5 which studies the effect of cell thickness on the behaviour of the device. In Section 7.6, we compare Fourier's law with the MC simulation and apply the MC simulation to a case which involves a thin film exposed to convective cooling. This chapter ends with concluding remarks formed in Section 7.7.

The bulk of this chapter was published in the *Journal of Applied Physics* and can be found in [124].

7.1 System Configuration and Simulation Parameters

The one-dimensional nano-gap TPV device depicted in Fig. 7.1 is simulated using the procedure described in Chapter 4 which is based on the work in [34]. The near-field radiation heat transfer problem is solved using fluctuational electrodynamics where the fluctuation-dissipation theorem is employed to solve the Maxwell equations. Medium 5 is modelled as vacuum to simplify the problem.

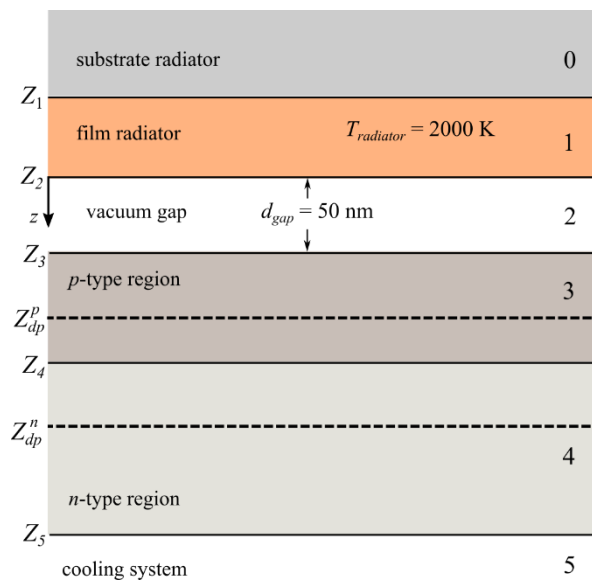


Fig. 7.1 Schematic diagram of a nano-gap TPV device.

A 2000-K W radiator on an alumina substrate is paired with a doped-Si TPV cell separated by an arbitrarily chosen 50-nm vacuum gap. Smaller gap sizes are theoretically possible but are extremely difficult to achieve experimentally. In Sections 7.3 and 7.4, the TPV cell has a thickness of 1 μm . In Section 7.5, the thickness is varied from 0.5 to 1 μm . The TPV cell is discretized into nodes which form control volumes of 1 nm in length except for the control volumes at the top and bottom boundaries which are halved. The doping concentration is arbitrarily set as 10^{23} m^{-3} for both p and n -type regions. The spectral range of the simulation goes from $7.7 \times 10^{13} \text{ rad/s}$ to $3.8 \times 10^{15} \text{ rad/s}$ with a step size of $0.5 \times 10^{13} \text{ rad/s}$ as done in [34,60].

7.2 Material Properties

7.2.1 Optical

The alumina substrate is modelled using Eq. (7.1) based on the parameters for 99.6% alumina (0.4% glass) found in [116] and also in Appendix A.

$$\varepsilon_r(\omega) = \varepsilon_\infty + \sum_{j=1}^n \frac{\Delta\varepsilon_j \omega_j^2}{\omega_j^2 - \omega^2 - i\omega\gamma_j} \quad (7.1)$$

The thin-film W used in this work is modelled after a 105-nm unannealed W sample called W04 used in the experimental work of Watjen et al. [125]. Its dielectric function is obtained using the Drude-Lorentz model along with the parameters found in [125] and in Appendix A:

$$\varepsilon_r(\omega) = \varepsilon_\infty - \frac{\Omega_p^2}{\omega^2 + i\Gamma\omega} + \sum_{j=1}^M \frac{\omega_{p,j}^2}{\omega_j^2 - \omega^2 - i\gamma_j\omega} \quad (7.2)$$

The Si TPV cell's dielectric function is described using a Drude model (Eq. (5.9)) detailed in [102] with the addition of a lattice absorption model from [103]. Equation (5.9) allows us to account for doping effects. The ionization model of dopants used in our work is taken from [104].

7.2.2. Electrical

The electrical properties of Si which include the minority carrier lifetimes, mobilities and diffusion coefficients are all modelled based on the work done by Vaillon et al. [82]. The temperature dependence of the band gap, E_g is modelled using the Varshni equation [93] where the band gap at 300 K is 1.12 eV. The intrinsic carrier concentration is written as $n_i^2 = N_C(T_{cell,avg})N_V(T_{cell,avg})e^{-E_g(T_{cell,avg})/k_B T_{cell,avg}}$ where the effective density of states, N_C and N_V are $2.8 \times 10^{19} \text{ cm}^{-3}$ and $1.04 \times 10^{19} \text{ cm}^{-3}$ at 300 K respectively [82,93]. The surface recombination velocities of the TPV cell used in this work are $S_e = 10 \text{ m/s}$ and $S_h = 1 \text{ m/s}$.

7.2.3 Thermal

The thermal conductivity of bulk Si used when implementing Fourier's law is taken from [126] with a slight modification to include the position-dependent cell temperature:

$$k_{cond}(T_{cell}(z)) = \frac{100}{0.03 + 1.56 \times 10^{-3} T_{cell}(z) + 1.65 \times 10^{-6} (T_{cell}(z))^2} \quad (7.3)$$

The phonon scattering rates of Si used in the MC simulation are based on the work done in [127].

7.3 Responses and Performance as a Function of Cell Temperature

7.3.1 Alumina Substrate

In this section, the dependence of the responses and performance of a thin-film nano-gap TPV device on cell temperature is discussed. A 105-nm thin-film W radiator on an alumina substrate is paired with a 1- μm TPV cell across a 50-nm vacuum gap. The temperature of the cell is assumed to be uniform. Referring to Fig. 7.2, the radiative heat flux on the surface of the cell increases with T_{cell} , especially above the band-gap frequency. This is due to the increased absorption coefficient of Si as a result of higher temperatures as shown in Fig. 7.3. The absorption coefficient is calculated using Eq. (7.4) [128].

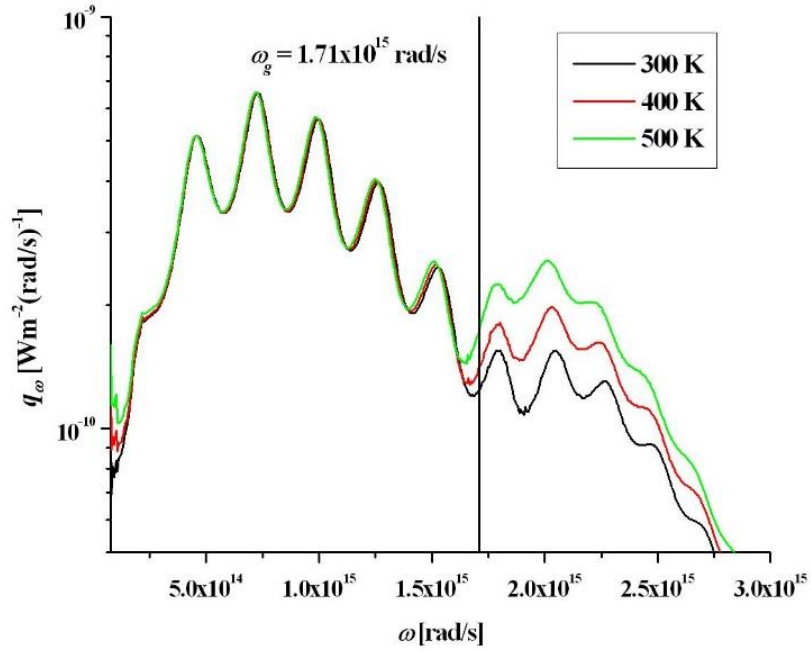


Fig. 7.2 Monochromatic radiative heat flux on the surface of the TPV cell when T_{cell} is 300 K, 400 K and 500 K.

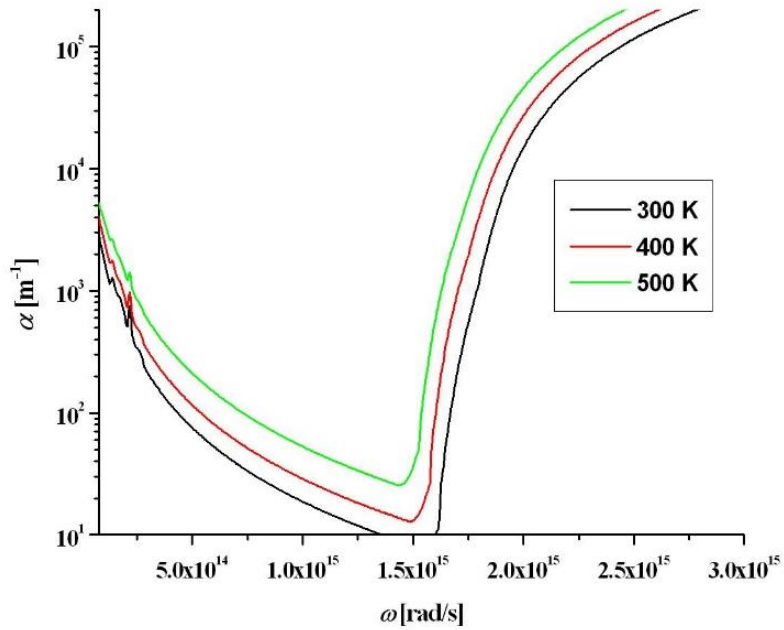


Fig. 7.3 Absorption coefficient of Si at different temperatures.

$$\alpha(\omega) = \frac{2\omega}{c_v} \left[\frac{\sqrt{(\varepsilon'_r(\omega))^2 + (\varepsilon''_r(\omega))^2} - \varepsilon'_r(\omega)}{2} \right]^{1/2} \quad (7.4)$$

As shown in Table 7.1, the increased absorption causes an increase in the total absorbed heat flux (sum of absorbed heat fluxes below and above ω_g). However, the conversion efficiency of the nano-gap TPV device experiences a decline as T_{cell} increases. This is mainly caused by the increase in dark current (recombination current) which in turn reduces the open-circuit voltage, V_{oc} .

Table 7.1 Performance of the nano-gap TPV device at different T_{cell} values.

T_{cell} (K)	Absorbed heat flux below ω_g , $P_{abs, \leq \omega_g}$ (Wm^{-2})	Absorbed heat flux above ω_g , $P_{abs, \geq \omega_g}$ (Wm^{-2})	Maximum output power, P_m (Wm^{-2})	Conversion efficiency, η_c (%)
300	5.24×10^3	7.68×10^4	3.30×10^4	40.20
390	7.39×10^3	1.03×10^5	3.48×10^4	31.49
400	7.79×10^3	1.06×10^5	3.49×10^4	30.50
410	8.16×10^3	1.10×10^5	3.48×10^4	29.49
500	1.29×10^4	1.47×10^5	3.29×10^4	20.53

The analytical expression for J_0 is presented as [129]:

$$J_0(V_f) = e \left(\frac{n_i^2 D_h}{N_D \sqrt{\tau_h}} + \frac{n_i^2 D_e}{N_A \sqrt{\tau_e}} \right) \left[\exp\left(\frac{eV_f}{k_B T_{cell}} \right) - 1 \right] \quad (7.5)$$

This expression gives us a better idea of how the dark current changes with temperature. It can be seen from Eq. (7.5) that J_0 is dependent on the intrinsic carrier concentration, n_i , minority carrier diffusion coefficient, $D_{e,h}$, and minority carrier lifetime, $\tau_{e,h}$ which are all temperature dependent. As temperature increases, the intrinsic carrier concentration increases while the carrier lifetime decreases causing an increase in dark current. Due to the fact that dark current is mainly caused by recombination, it could be put simply that the main reason for the poor efficiencies at elevated cell temperatures is the greater recombination rate within the cell. Figure 7.4 shows how rapidly J_0 increases with increasing T_{cell} causing the net current to diminish at ever lower V_f values. It has to be noted that J_0 in Fig. 7.4 is found by solving Eq. (4.47) in dark conditions. The observations thus far are consistent with the findings in [34,82].

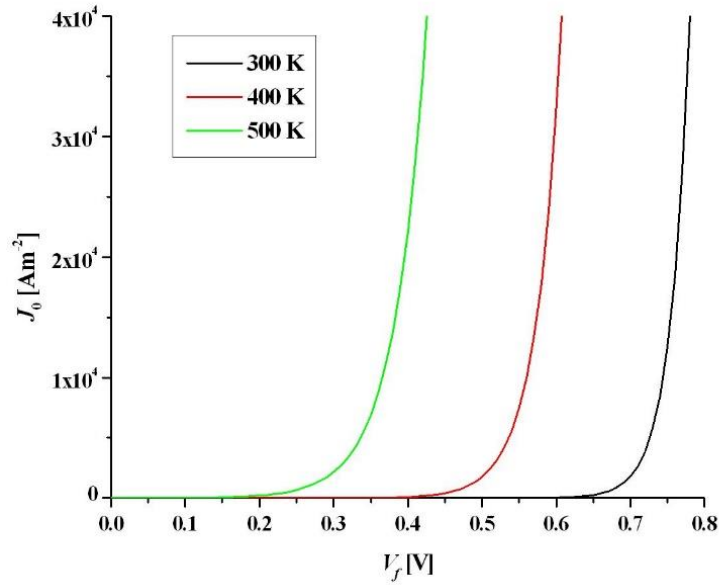


Fig. 7.4 Dark current as a function of forward bias when T_{cell} is 300 K, 400 K and 500 K.

Despite the decreasing efficiency, the maximum output power, P_m experiences enhancements as T_{cell} increases up to around 400 K above which P_m suffers along with efficiency. This observation can be explained by the increased absorption of the cell which allows for more EHPs to be generated which in turn increases J_{sc} . The rise in J_{sc} offsets the decreasing V_{oc} value as shown in Fig. 7.5 ($T_{cell} = 300$ K as compared to $T_{cell} = 400$ K) allowing for a greater P_m value. However at $T_{cell} = 500$ K, V_{oc} becomes too small which negatively affects the maximum output power. In other words, initially, the rise in the EHP generation rate due to increased absorption outstrips the rise in the recombination rate, causing P_m to increase. Above 400 K, the recombination rate begins to dominate, causing P_m to fall. This trend differs from the one obtained by Francoeur et al. [34] where they discovered that the P_m value produced by an InGaSb cell (doping-dependence of the dielectric function is not included) is maximum at 300 K. Thus, it is important to consider different materials on a case-by-case basis.

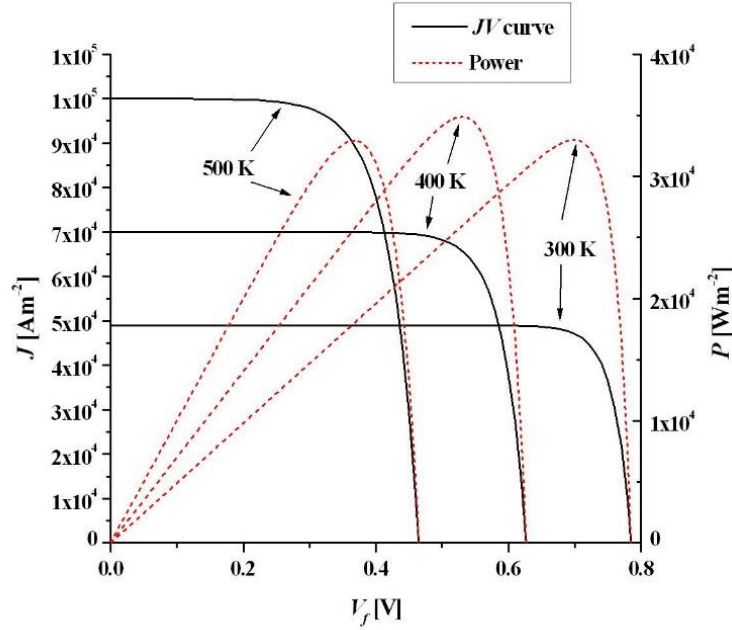


Fig. 7.5 Current-voltage curve and output power as a function of forward bias at different T_{cell} values.

It is conventional wisdom that the cell temperature should be kept at 300 K for the best performance. However, based on the observations made here, one could make a case for allowing the cell to be maintained at a higher temperature in order to increase the maximum output power. Moreover, the cooling requirement for maintaining a higher temperature is less demanding which may improve the overall system efficiency.

7.3.2 Vacuum Substrate

In this section, we simulate a nano-gap TPV device that uses a vacuum substrate using the same configuration as Section 7.3.1.

Table 7.2 shows the performance metrics of the device and it is clear that the values are very close to the ones obtained when alumina is used as the substrate. The percentage differences relative to the results of Table 7.1 do not exceed 0.6 %. This is due to the fact that alumina behaves very much like vacuum at most frequencies [116]. Thus for the remainder of the chapter, the substrate (layer 0) is modelled as vacuum in order to reduce computation time.

Table 7.2 Performance of the device using a vacuum substrate at different T_{cell} values.

T_{cell} (K)	Absorbed heat flux below ω_g , $P_{abs, \leq \omega_g}$ (Wm^{-2})	Absorbed heat flux above ω_g , $P_{abs, \geq \omega_g}$ (Wm^{-2})	Maximum output power, P_m (Wm^{-2})	Conversion efficiency, η_c (%)
300	5.24×10^3	7.65×10^4	3.29×10^4	40.18
400	7.81×10^3	1.06×10^5	3.47×10^4	30.47
500	1.30×10^4	1.47×10^5	3.27×10^4	20.49

7.4 Comparing a Thin-Film W with a Bulk W Radiator

In this section, we compare a 105-nm W thin film (W04) with a bulk W radiator within the context of a nano-gap TPV device. The radiators are paired with a 1- μm TPV cell whose temperature is assumed to be uniform and constant at 300 K. Once again the vacuum gap is fixed at 50 nm.

Based on Table 7.3, the output power using a thin-film W radiator is almost double that of a nano-gap TPV device that uses a bulk W radiator albeit with a slightly lower conversion efficiency. This observation is due to the change in the optical response of the nano-gap TPV device.

Table 7.3 Performance of nano-gap TPV devices with different radiators with $T_{cell} = 300$ K.

Radiator	P_{abs} (Wm^{-2})	P_m (Wm^{-2})	η_c (%)
Thin-film W [125]	8.18×10^4	3.29×10^4	40.18
Bulk W [89]	4.34×10^4	1.79×10^4	41.22

Figure 7.6 shows the spectral distribution of the radiative heat flux on the surface of the TPV cell from three different types of radiators. The fluctuations are caused by interference effects due to multiple reflections in the layers. It is clear that W04 improves the overall radiative heat transfer across the vacuum gap and this can be attributed to the greater emissivity of W04 as compared to bulk W [130]. The increase in emissivity is partly caused by the lower plasma frequency of an unannealed W film [130]. The effect of thickness plays a rather significant role as well. The thickness of the radiator influences the interaction between the multiple reflected waves in the layers especially within the radiator itself and also affects the strength of the coupling between surface waves which are present on the top and bottom surfaces of the

radiator. To demonstrate the effect of radiator thickness, the dielectric function of W04 is used to model a bulk radiator and the heat flux profile it produces is shown alongside the thin-film W04 in Fig. 7.6. Increasing its thickness to that of a bulk causes the heat flux profile of the W04 radiator to change where it can be seen that more heat flux is produced below the band gap and less above it which will inadvertently reduce the conversion efficiency of the nano-gap TPV device. This result highlights the benefits of using a thin-film W radiator over its bulk counterpart, thus providing another avenue to improve the electrical power output of nano-gap TPV devices.

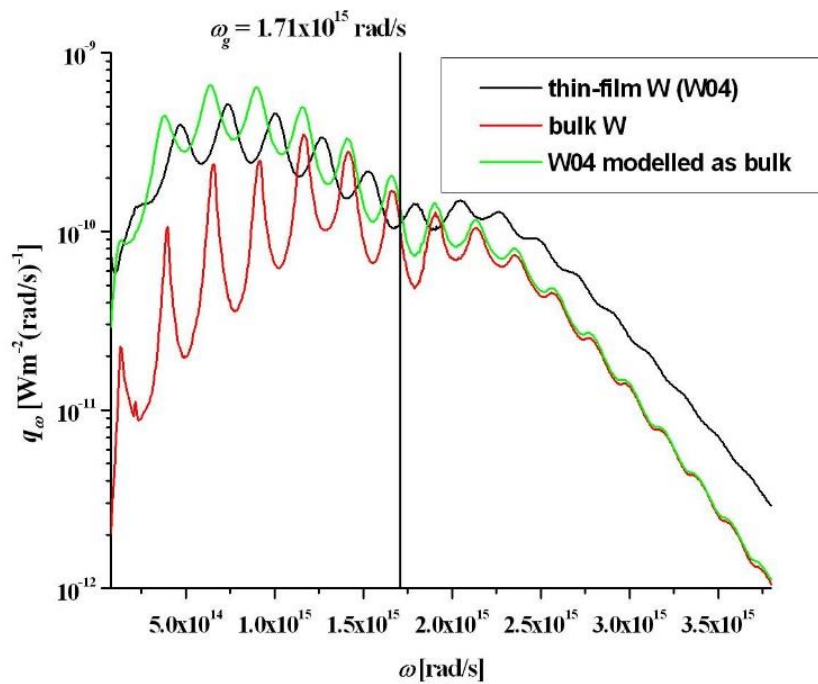


Fig. 7.6 Monochromatic radiative heat flux on the surface of the TPV cell from different radiators.

However, the conversion efficiencies in Table 7.3 do not include the cooling requirement. The amount of heat generated in the TPV cell when paired with a bulk W radiator is $1.29 \times 10^4 \text{ Wm}^{-2}$ while it is $2.69 \times 10^4 \text{ Wm}^{-2}$ when thin-film W is used. This implies that the amount of cooling power needed to maintain the cell at 300 K is greater for the case with a thin-film radiator. The h_{conv} value needed to maintain T_{cell} at 300 K is around $1.84 \times 10^3 \text{ Wm}^{-2}\text{K}^{-1}$ when a bulk W radiator is used and $3.84 \times 10^3 \text{ Wm}^{-2}\text{K}^{-1}$ for the thin-film W radiator. Further discussions regarding the effect the cooling requirement has on efficiency can be found in Section 7.5.3.

7.5 Responses and Performance as a Function of Cell Thickness

In this section, we pair a thin-film W radiator with a Si TPV cell with a thickness that varies from 0.5 μm to 1 μm . For all cases presented, the thicknesses of the p and n -type regions are equal. For example, when the cell thickness is 1 μm , the p and n -type regions are 0.5- μm thick respectively. We observe how TPV cell thickness affects the responses and performance of the nano-gap TPV device while taking into account thermal effects. Fourier's law is used to model heat transport in the thin-film TPV cells. The justification for the use of Fourier's law can be found in Section 7.6.2.

7.5.1 Optical Response and Performance

Here, we present the spectral radiative heat transfer profiles between the radiator and TPV cells of varying thicknesses. The performances of these nano-gap TPV devices are then extracted from the simulation. The cell temperature is fixed at an arbitrarily chosen temperature of 300 K to facilitate qualitative comparisons.

As shown in Fig. 7.7, the heat flux above ω_g on the surface of the TPV cell generally increases with cell thickness. The radiative heat transfer below ω_g for the different thicknesses fluctuates around relatively similar heat flux values rendering comparisons extremely difficult and are thus omitted from the figure. Based on Fig. 7.8, we can see that the heat flux absorbed by the cell, maximum output power and conversion efficiency all increase with cell thickness. We thus compare the two limiting thicknesses: 1 μm and 0.5 μm . Given a greater radiative heat transfer rate and a bigger thickness, the 1- μm cell ends up absorbing much more heat flux as shown in Table 7.4. The 1- μm cell performs better than the 0.5- μm cell in terms of maximum output power, P_m and conversion efficiency, η_c (cooling requirement not included) as a greater percentage of its absorbed heat flux is above ω_g . This is due to the more favourable spectral heat flux profile on the surface of the 1- μm cell (greater radiative heat transfer above ω_g).

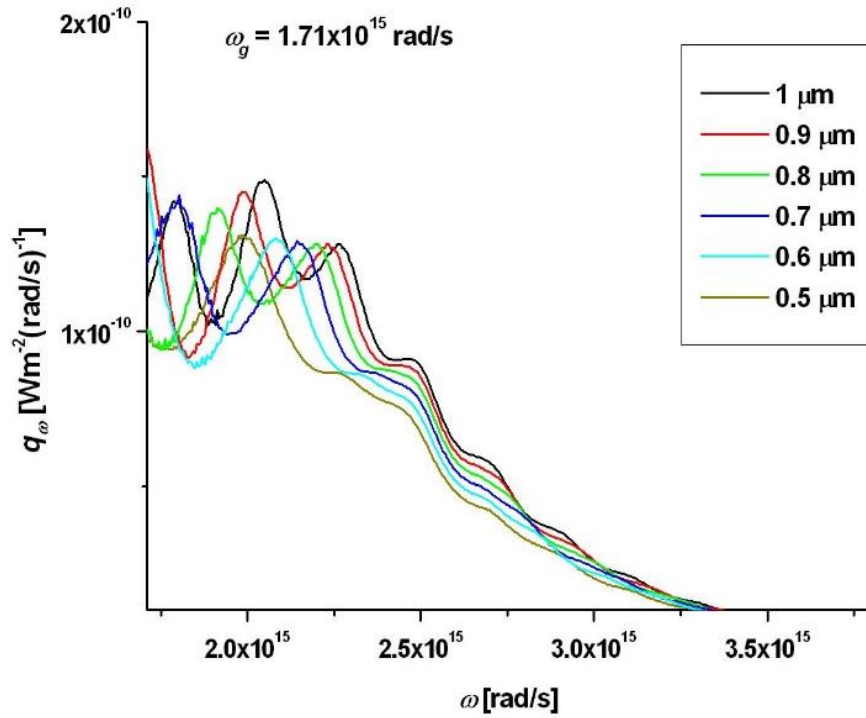


Fig. 7.7 Monochromatic radiative heat flux on the surface of the TPV cell at different cell thicknesses. $T_{cell} = 300 \text{ K}$.

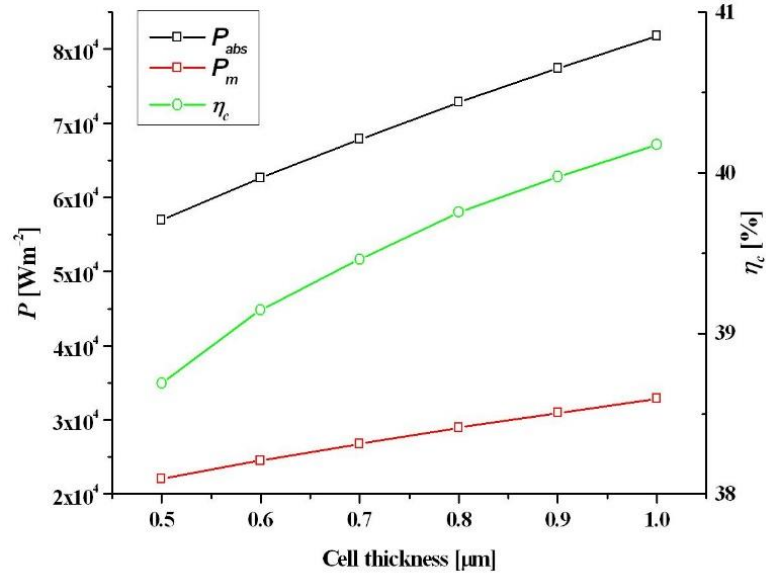


Fig. 7.8 Performance of a nano-gap TPV device as a function of cell thickness. Do note that only the symbols indicate actual data points.

Table 7.4 Performance of the nano-gap TPV device for two different TPV cell thicknesses both with $T_{cell} = 300$ K.

Cell thickness (μm)	$P_{abs,\leq \omega_g}$ (Wm^{-2})	$P_{abs,\geq \omega_g}$ (Wm^{-2})	P_m (Wm^{-2})	η_c (%)
1.0	5.24×10^3	7.65×10^4	3.29×10^4	40.2
0.5	4.55×10^3	5.24×10^4	2.20×10^4	38.7

7.5.2 Thermal Response

Here, we compare the volumetric heat generation and thermal responses of two nano-gap TPV devices with TPV cell thicknesses of $1 \mu\text{m}$ and $0.5 \mu\text{m}$ respectively. Do note that the heat source due to radiative recombination, $Q_{RR}(z)$ is not included in the calculation due to the negligible radiative recombination rate for Si. The cell temperature is only fixed at 300 K in obtaining Fig. 7.9 to Fig. 7.11. For the rest of this sub-section, the temperature is allowed to change naturally.

Based on Fig. 7.9, it is interesting to note that the volumetric heat generation in a $0.5\text{-}\mu\text{m}$ cell is greater than a $1\text{-}\mu\text{m}$ cell. In order to investigate this further, we plot the contributions to heat generation as shown in Fig. 7.10. The contribution from recombination is insignificant (about 5 magnitudes smaller) and is therefore omitted from the figure. It is clear from Fig. 7.10 that the heat sources in the thinner cell generate more volumetric heat though it has to be noted that the contribution from recombination decreases with thickness due to lower EHP concentrations. Furthermore, thermalization is the dominant mechanism by which heat is generated in the cell. Thermalization is caused by the absorption of photons with energies exceeding the band gap. Figure 7.11 shows the absorbed above-band-gap radiative heat flux profile for a selection of cell thicknesses. In general, as the cell thickness is reduced, the amount of heat flux absorbed by each node increases which explains the increase in thermalization. The enhancement in the absorbed heat flux is due to pronounced interference effects as a result of more frequent reflections within the thinner cell which also allows excitation of surface waves at the bottom interface [119]. The cell thickness also affects the position of the resonant modes. As the cell thickness is reduced, the first ridge after the peak heat flux value widens and shifts downwards, towards the bottom of the cell while the two more noticeable ridges near the bottom surface widen and shift upwards.

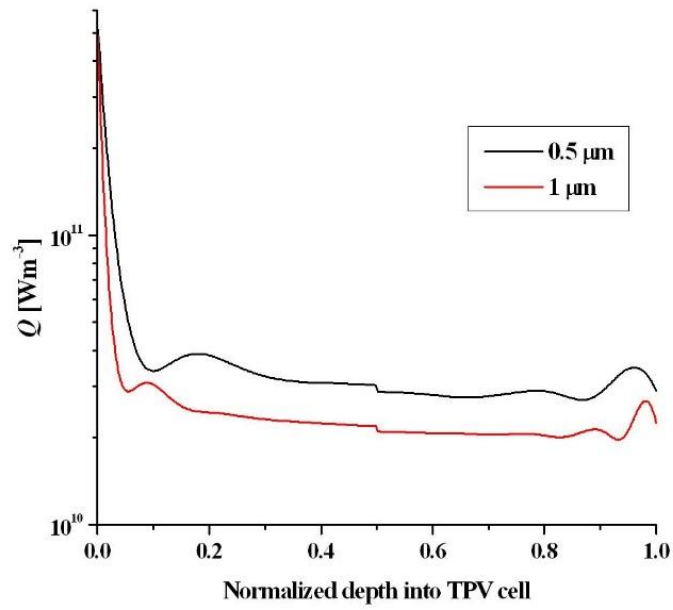


Fig. 7.9 Volumetric heat generation within the TPV cell at two different thicknesses. $T_{cell} = 300$ K.

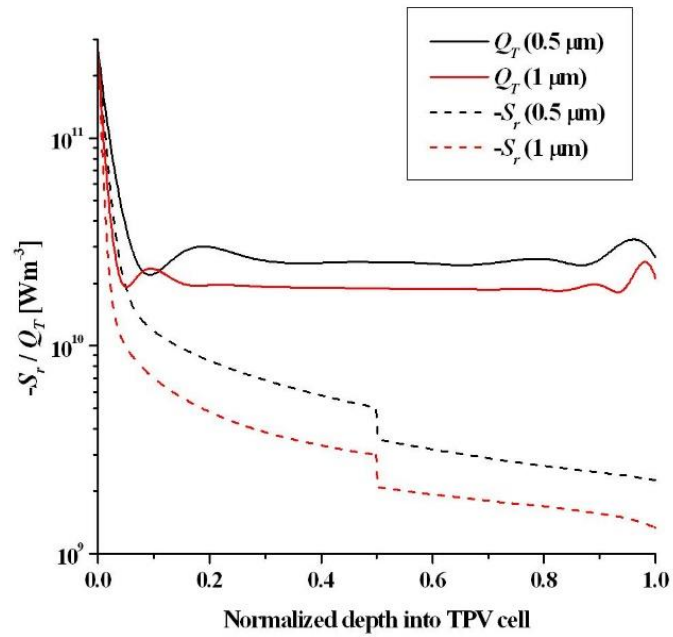


Fig. 7.10 The local radiative heat source and thermalization within the TPV cell at two different thicknesses. $T_{cell} = 300$ K.

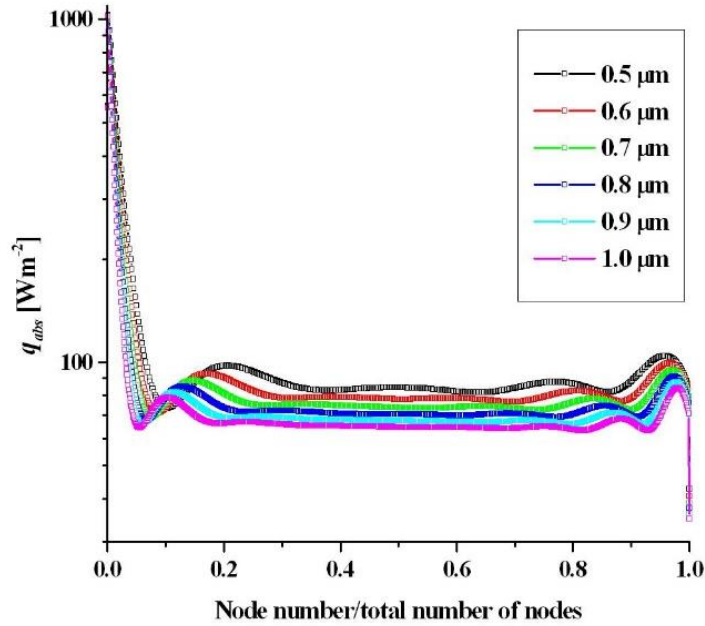


Fig. 7.11 Above-band-gap heat flux absorbed by each control volume (node) within the TPV cell. $T_{cell} = 300$ K. (Normalized node 0 and 1 represent the top and bottom surfaces respectively).

Even though the volumetric heat generation is greater in a 0.5- μm cell, the total heat energy generated is still lower than in a 1- μm cell as there is less volume for the generation of heat to take place in. For a cell temperature of 300 K, the amount of heat generation in a 0.5- μm cell is around $1.95 \times 10^4 \text{ Wm}^{-2}$ and approximately $2.69 \times 10^4 \text{ Wm}^{-2}$ in a 1- μm cell. Table 7.5 is obtained by allowing the cell temperature to change until the simulation converges. The average temperature at convergence depends very much on the h_{conv} value used. The results show that the cooling requirement for a thinner TPV cell is less demanding and is in line with the discussion of the previous paragraph. At $h_{conv} = 5 \times 10^2 \text{ Wm}^{-2}\text{K}^{-1}$ (free convection [131]), the average temperature, $T_{cell,avg}$ in a 1- μm cell is 20.3 K higher than the $T_{cell,avg}$ of a 0.5- μm cell ($T_{cell,avg}$ is taken to be the uniform temperature within the cell due to really small temperature gradients). Furthermore, in order to maintain T_{cell} at around 300 K, the required h_{conv} for the 1- μm cell is around $10^3 \text{ Wm}^{-2}\text{K}^{-1}$ greater than for the 0.5- μm cell. Based on the approximation method detailed in Section 7.6.3, the h_{conv} required to maintain a uniform cell temperature of exactly 300 K is $2791.032 \text{ Wm}^{-2}\text{K}^{-1}$ for a 0.5- μm cell and $3838.35 \text{ Wm}^{-2}\text{K}^{-1}$ for a 1- μm cell which can be achieved through forced convection [131]. It is assumed that the temperature of the cooling fluid remains at 293 K for both cases. Thus it is clear that less resources are required to cool a thinner cell which is a crucial point to consider due to its effect on the overall system efficiency.

Table 7.5 $T_{cell,avg}$ and the maximum temperature gradient at different h_{conv} values for the two different cell thicknesses.

Thickness (μm)	h_{conv} ($\text{Wm}^{-2}\text{K}^{-1}$)	$T_{cell,avg}$ (K)	ΔT (K)
1.0	5×10^2	357.2	1.54×10^{-4}
	4×10^3	299.7	1.03×10^{-4}
0.5	5×10^2	336.9	5.01×10^{-5}
	3×10^3	299.5	3.85×10^{-5}

7.5.3 Efficiency Inclusive of the Cooling Requirement

Because a reliable estimation of the power requirement for the cooling system is unavailable, we will just perform a simple qualitative analysis of the nano-gap TPV device efficiency inclusive of the cooling requirement. Based on Table 7.4, it is clear that the 1- μm TPV cell performs better with regards to output power and efficiency. However, the h_{conv} required is about 1.4 times the value for the 0.5- μm cell as described in the previous paragraph. If the electrical power necessary to cool the cell is proportional to h_{conv} , the percentage increase in the cooling power requirement from the 0.5- μm cell to the 1- μm cell is equal to the percentage increase in h_{conv} which roughly amounts to 37.5 %. The percentage increase in maximum output power on the other hand is about 49 % and for the total amount of heat flux absorbed, it is 43.5% (Table 7.4). It is clear that the increase in output power is greater than the increase in the cooling requirement. Thus, if a proportion of the output power is used to power the cooling system, the overall efficiency of a nano-gap TPV device that uses a 1- μm cell remains greater than its thinner counterpart provided that the assumption of proportionality holds.

It has been shown that h_{conv} is proportional to the average velocity of the cooling fluid [132,133]. Furthermore, it is well known that the power consumed by a pump is proportional to the flow rate of the fluid through the pump. If forced convection is achieved through the use of a cooling system that includes a pump and a cooling fluid, it is safe to assume that the power requirement of the cooling system is proportional to the desired h_{conv} value. Hence, it can be concluded that if the increase in maximum output power exceeds the increase in the cooling system power consumption (when the cell thickness is increased), then the use of a nano-gap TPV device that generates more heat is justified provided that the conversion efficiency (without the cooling requirement) is favourable to begin with.

The trends presented in this section may continue beyond the thickness of 1 μm . Thus, it is by no means certain that 1 μm is the optimal thickness for a Si TPV cell. However, we limit our scope to thin films of thicknesses 1 μm and below as mentioned in the introduction. The analyses of thicker films are left to future studies.

7.6 Heat Transport Models

In this section, we look at the two heat transport models used in this thesis: Fourier's law and the MC simulation. The two methods are compared for consistency and in Section 7.6.2, the temperature profiles in thin films exposed to extreme heat generation and cooling are discussed.

7.6.1 Consistency Test

Here, a 5- μm Si film with a 310 K temperature boundary as its top surface and a bottom surface exposed to convective cooling ($h_{conv} = 1 \times 10^7 \text{ Wm}^{-2}\text{K}^{-1}$) is simulated (the values are arbitrarily chosen). The temperature profiles produced by using Fourier's law and MC simulation are compared.

Figure 7.12 shows the temperature profiles produced by the two different heat transport models. It can be seen that the temperatures found using Fourier's law are slightly higher. This is due to the difference in thermal conductivity between the two methods. When implementing Fourier's law, the thermal conductivity of bulk Si is used while the thermal conductivity in the MC simulation is calculated statistically and varies considerably from one point to another. Bulk thermal conductivity is usually larger producing a smaller temperature gradient, hence the greater temperature profile when using Fourier's law. Despite the difference, the overall trend is consistent, giving us confidence that the simulation results are reliable.

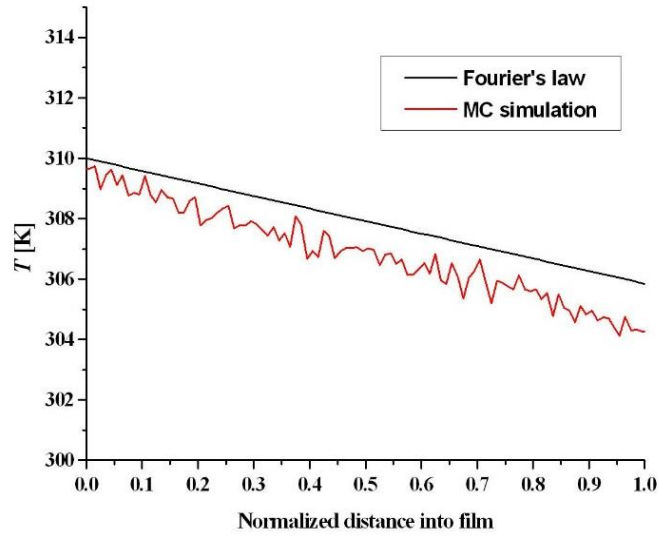


Fig. 7.12 Temperature profiles in a 5- μm Si film from two different heat transport models.

7.6.2 MC Simulation in Thin Films

As briefly described in the introduction, it has been shown that for an insulated Si film of thickness 20 nm subjected to near-field radiative heating (PV effect is not included), the temperature profile within the film remains largely uniform [123]. The same could be said of fully insulated GaAs films of thicknesses 1 μm to 5 μm [88]. In a fully insulated system, there are no occurrences of phonon destruction. Thus, in this section, we would like to determine if the introduction of convective cooling—which introduces a spatially localized phonon destruction scheme—has any effect on the temperature profile of a Si film with thicknesses of 1 μm and 0.5 μm . One estimate of the effective mean free path of phonons in Si at room temperature is around 300 nm [134], thus at small film thicknesses, the effect of semi-ballistic transport should be considered. For this reason, we employ the use of MC simulation to solve for the temperature profile in the film. The 1- μm and 0.5- μm Si thin films which are subjected to the volumetric heat generation of Section 7.5.2 are simulated with a top surface that is insulated (adiabatic) and a bottom surface exposed to convective cooling. However, we discovered that the volumetric heat generation values from Section 7.5.2 are too small to generate phonons in the MC simulation, thus, we simulate extreme conditions by increasing the heat generation term by 5 to 6 orders of magnitude. For each enhancement case, a specific h_{conv} value is used. For example, at 5×10^5 times the Q_{tot} term, a h_{conv} of $5 \times 10^8 \text{ Wm}^{-2}\text{K}^{-1}$ is used. At an enhancement of 6×10^5 , a h_{conv} of $6 \times 10^8 \text{ Wm}^{-2}\text{K}^{-1}$ is used. The same increments are

maintained as the enhancement is increased up to 10^6 . 10-nm control volumes are used in the MC simulation.

Figure 7.13 shows how the temperature gradient in a 1- μm film increases with greater internal heating and convective cooling. The profiles can be taken as linear albeit with fluctuations caused by statistical noise. The results seem to suggest that the high rate of phonon injection—especially at the region near the top surface—due to the enhanced volumetric heat generation along with the high phonon destruction rate at the convective boundary, with both exceeding the rate of phonon dispersion, end up producing greater temperature gradients in the thin film. The temperature gradient of each case is extracted by fitting a linear trendline to the profile and finding the difference between the temperature of the first point and the last. These temperature gradients are then used to determine the relationship between the temperature gradient and the enhanced cases as depicted in Fig. 7.14. The same is done for the case of a 0.5- μm Si film. A polynomial curve is fitted to the data points for each thin film to yield an equation that is used to give a rough estimate of the temperature gradient at Q_{tot} (no enhancement) with a h_{conv} of $10^3 \text{ Wm}^{-2}\text{K}^{-1}$. The equations are $y = 4 \times 10^{-17}x^3 - 3 \times 10^{-11}x^2 + 4 \times 10^{-5}x$ and $y = 2 \times 10^{-17}x^3 - 5 \times 10^{-12}x^2 + 2 \times 10^{-5}x$ for the 1- μm and 0.5- μm cases respectively. Thus at normal conditions ($x = 1$) and at a simulation time of 2×10^{-8} s, we could roughly estimate ΔT (the y variable) to be 4×10^{-5} K for the 1- μm film and 2×10^{-5} K for the 0.5- μm film. These values are really small and comparable to the steady-state values found in Section 7.5.2. At lower volumetric heat generation values and convective cooling i.e. the rates of injection and destruction are lower, we reason that the phonons generated have enough time to disperse causing the concentration of phonons to be close to uniform across the thin film. This gives us confidence to conclude that at normal conditions, the temperature profile in thin films of Si is almost flat and can be represented by a single temperature. The results here also allow us to justify the use of Fourier's law to model heat transport in thin films since it also predicts a profile that is close to uniform especially at reduced film thicknesses.

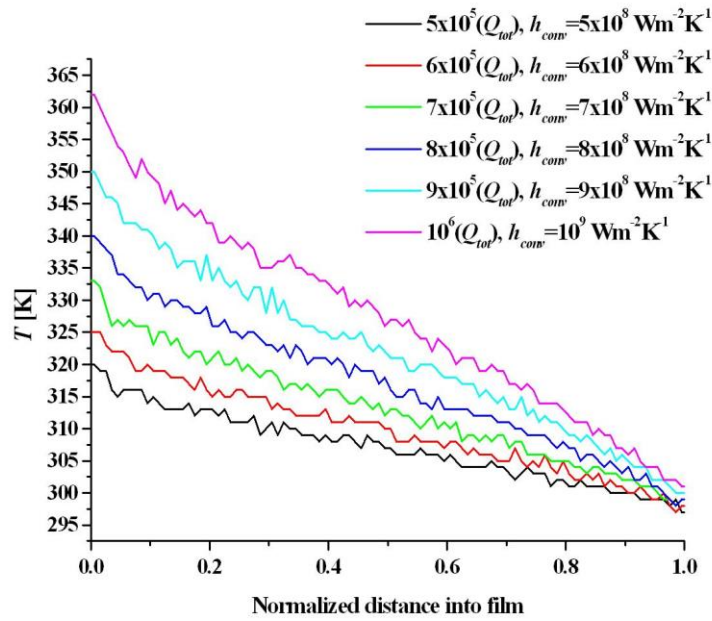


Fig. 7.13 Temperature profiles in a 1- μm Si film exposed to enhanced volumetric heat generation and convective cooling at a simulation time of 2×10^{-8} s.

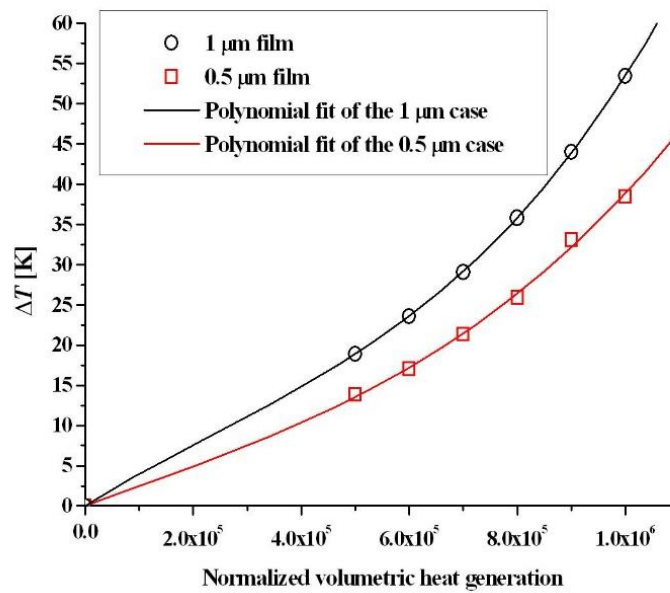


Fig. 7.14 Temperature gradients (the difference between the top and bottom surface temperatures) within Si thin films at different volumetric heat generation. The open symbols represent actual data points.

However, the Fourier's law uses bulk thermal conductivity values which do not accurately reflect the conductivity of thin films. Based on the MC simulations performed, we obtained an average thermal conductivity (over all enhancement cases) of $82.02 \text{ Wm}^{-1}\text{K}^{-1}$ and $61.7 \text{ Wm}^{-1}\text{K}^{-1}$ for the 1- μm and 0.5- μm cases respectively at a simulation time of 2×10^{-8} s. The bulk

thermal conductivity at 300 K is approximately $155 \text{ Wm}^{-1}\text{K}^{-1}$. Clearly at reduced thicknesses, the thermal conductivity decreases significantly and one wonders if this has an effect on the temperature profile obtained using Fourier's law. In order to test that, the lower thermal conductivities obtained from the MC simulation are used in our Fourier's law model using the exact same volumetric heat generation of Section 7.5.2 ($T_{cell} = 300 \text{ K}$). The results are shown in Table 7.6 along with the results obtained using a thermal conductivity of $155 \text{ Wm}^{-1}\text{K}^{-1}$. Based on Table 7.6, it is clear that there is an increase in the temperature gradient when the thermal conductivity is reduced, however the gradients are still negligibly small. Thus, the conclusion holds; in that the Fourier's law is sufficient as a heat transport model for thin films ($\leq 1 \mu\text{m}$).

Table 7.6 Temperature gradients generated using Fourier's law at different thermal conductivity values. $h_{conv} = 5 \times 10^2 \text{ Wm}^{-2}\text{K}^{-1}$.

k_{cond} ($\text{Wm}^{-1}\text{K}^{-1}$)	ΔT (K) (0.5-um film)	ΔT (K) (1-um film)
61.7	9.7×10^{-5}	-
82.02	-	1.95×10^{-4}
155	3.85×10^{-5}	1.03×10^{-4}

7.6.3 Uniform Cell Temperature Approximation

If the assumption that the temperature profile in the TPV cell is uniform holds true i.e. it can be represented by a single T_{cell} , then approximating the cell temperature becomes a simple affair. The uniformity of T_{cell} can be justified by the fact that for thin films, the heat generation is not high enough to generate a significant temperature gradient at steady-state. Under that assumption we can then equate the heat generation in the cell with the convective heat flux: $q_{gen}(T_{cell}) = q_{conv} = h_{conv}[T_{cell} - T_{\infty}]$. This equation can be used to determine the h_{conv} value required to achieve a desired temperature, T_{cell} provided that $q_{gen}(T_{cell})$ is known (Eq. (7.6)) or it can be used to calculate the new temperature, $T_{cell,new}$ using $q_{gen}(T_{cell,old})$ and a given value of h_{conv} (Eq. (7.7)).

$$h_{conv} = \frac{q_{gen}(T_{cell})}{T_{cell} - T_{\infty}} \quad (7.6)$$

$$T_{cell,new} = T_{\infty} + \frac{q_{gen}(T_{cell,old})}{h_{conv}} \quad (7.7)$$

where $q_{gen}(T_{cell}) = \sum_{j=1}^{N_{tot}} Q_{tot,j}(T_{cell}) \Delta z_j$. N_{tot} is the total number of nodes in the cell. These equations simplify the heat transport problem considerably and speed up convergence of the simulation. However, it has to be reiterated that this approximation only applies to films where temperature gradients are negligible.

7.7 Concluding Remarks

We have studied a thin-film nano-gap TPV device that utilises a thin-film W radiator paired with a thin-film Si TPV cell. It is discovered that the increase in cell temperature allows for greater maximum output power at the cost of conversion efficiency. It is also shown that a thin-film W radiator enhances radiative heat transfer across the entire spectrum as compared to bulk W providing a potential avenue for increasing the power output of nano-gap TPV devices. Next, the effect of cell thickness was analysed. The thickness of the cell was varied from 0.5 μm to 1 μm and we discovered that the thicker thin-film TPV cells produced better performances. Despite greater cooling requirements for thicker thin films, the overall efficiency does not suffer much due to improvements in the maximum output power. Lastly, we tested the consistency of two heat transport models used in this thesis: Fourier's law and the phonon MC simulation with convective cooling implemented. In the case of thin films, we reason that at normal conditions, there will not be any significant temperature gradients, allowing us to approximate the cell temperature as uniform. One could question the need to employ the MC simulation based on the conclusions presented here but as mentioned in the first paragraph of Section 7.6.2, semi-ballistic transport should be considered when modelling heat transport in thin films. Thus, the use of MC simulations for accuracy is necessary.

Chapter 8 The Presence of a Third Body in Near-Field Radiative Heat Exchange

In this chapter, we analyse theoretically the effect of a third closely-spaced body on the radiative heat exchange between a radiator and a receiver. The third body is brought close to the receiver and essentially becomes a second receiver as depicted in Fig. 8.1. This configuration has potential application in near-field TPV systems which incorporate near-field cooling as a means of cooling the TPV cell. Apart from acting as a cooling mechanism, the second receiver can also be converted into a TPV cell to generate extra electrical power from the radiation it receives from either the radiator or the first TPV cell. If such applications were to be employed, it would be necessary for us to understand how the third body affects the radiative heat exchange so as to guide the design process.

8.1 System Configuration and Simulation Parameters

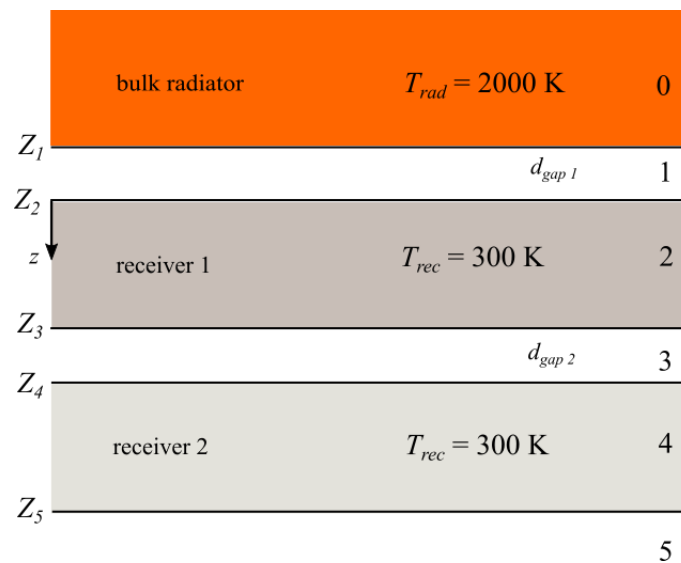


Fig. 8.1 Schematic of a radiator-receiver system in the presence of a third body (receiver 2) in close proximity.

The near-field thermal radiation model in Section 4.1 is applied in this chapter. The spectral radiative heat flux absorbed by receiver 1 (Rec1) is calculated as $q_{abs,\omega} = q_{\omega}(Z_2) - q_{\omega}(Z_3)$ where the monochromatic radiative heat flux at each point is calculated using Eq. (4.30). Do note that only the contribution from the bulk radiator is considered. The bulk radiator is maintained at 2000 K while the two receiver layers are maintained at 300 K. The vacuum gap

separating the radiator and Rec1, $d_{gap 1}$ is kept at 50 nm. The radiator and Rec1 are modelled as W [89] and $\text{In}_{0.18}\text{Ga}_{0.82}\text{Sb}$ [34,95] respectively. Two types of materials will be used to model receiver 2 (Rec2), namely, InSb [90,95] and Au [70] while all remaining layers are modelled as vacuum. The InSb Rec2 (low-band-gap semiconductor) is used to produce Figs. 8.2 to 8.4 while the Au Rec2 (metallic conductor) is used for Fig. 8.5. The spectral range of the simulation goes from 7.7×10^{13} rad/s to 3.8×10^{15} rad/s with a step size of 0.5×10^{13} rad/s as done in Chapter 7.

8.2 Results and Discussions

We first simulate a configuration where $d_{gap 1}$, $d_{gap 2}$ and Rec2 are all 50 nm in size with Rec1 having a variable thickness. Based on Fig. 8.2, we can see that when Rec1 is 50-nm thick, the presence of Rec2 alters its heat flux absorption spectrum considerably. At a thickness of 1 μm however, Rec1 becomes much less sensitive to the presence of Rec2, in fact the differences are quite negligible. If the thickness of Rec1 were to be increased even further, the differences would begin to diminish almost completely. One explanation for the results in Fig. 8.2 is the distance between the radiator and Rec2. The dominant wavelength of thermal radiation from a 2000 K source is around 1.45 μm based on Wien's law. When the separation distance between the radiator and Rec2 is close to or greater than the dominant wavelength, the presence of Rec2 ceases to have much of an impact on the near-field regime which dominates radiative heat transfer. The other explanation for the observation presented here would be the thickness of Rec1 itself. A thicker Rec1 would be able to absorb more radiative heat flux, causing its absorption spectrum to become less sensitive to changes induced by Rec2 whose influence is already weakening.

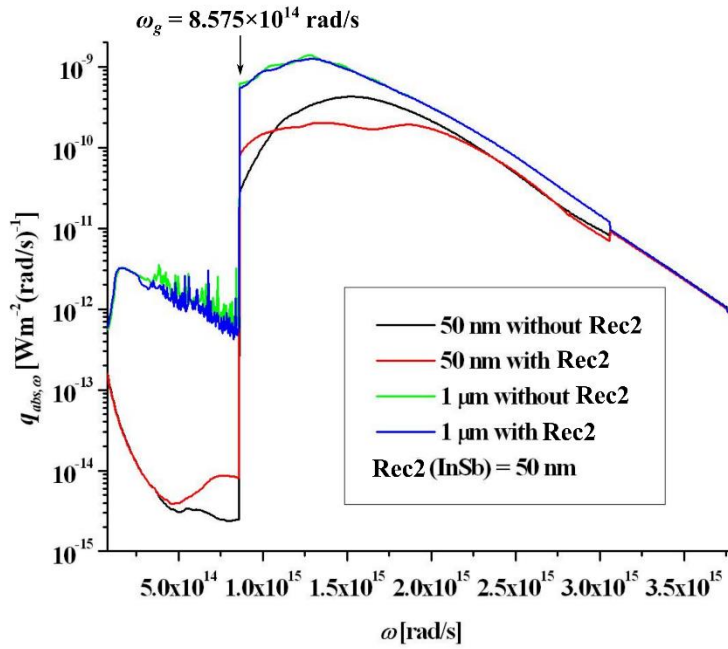
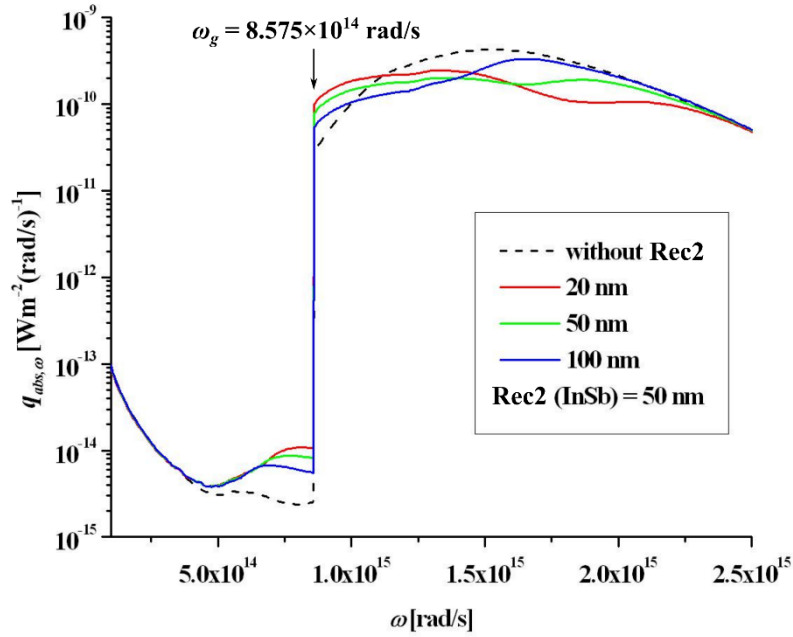
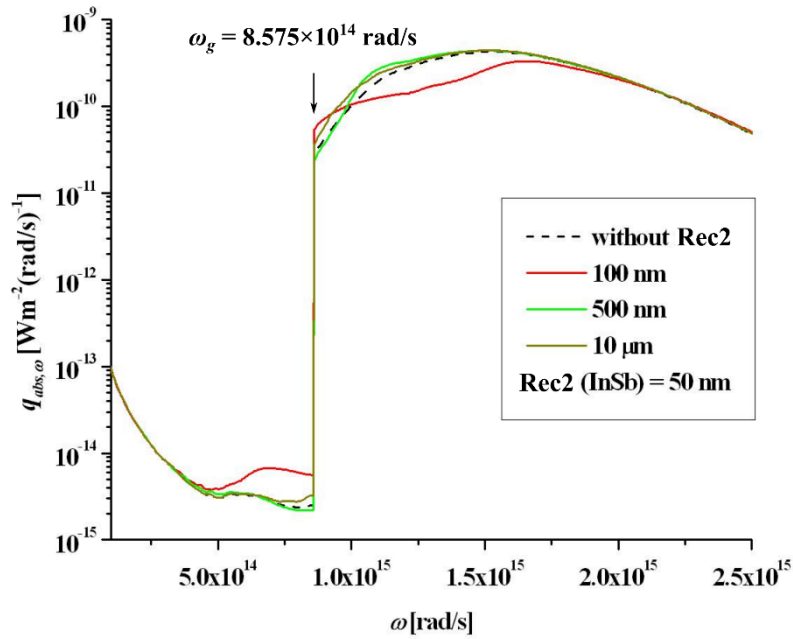


Fig. 8.2 Monochromatic radiative heat flux absorbed by Rec1 for two Rec1 thicknesses. $d_{gap 1} = d_{gap 2} = t_{Rec 2} = 50$ nm.

Figure 8.3 shows how changing $d_{gap 2}$ affects the absorption spectrum of Rec1. Do note that the sizes of $d_{gap 1}$, Rec1 and Rec2 are kept at 50 nm. It can be seen that at $d_{gap 2} = 20$ nm, the absorbed heat flux values in the spectral regions close to the band gap (8.575×10^{14} rad/s) are noticeably higher than the case without Rec2. As the gap is widened from 20 nm to 100 nm, the absorbed heat flux values in those regions experience declines while a peak forms further up the spectral profile. At a gap of 100 nm, the peak occurs at 1.652×10^{15} rad/s. At $d_{gap 2}$ values above 100 nm, the profile becomes comparable to the case without Rec2 especially at 500 nm. However, even at a gap of 10 μ m, there are still small deviations from the case without Rec2 which we attribute to propagating modes.



(a)

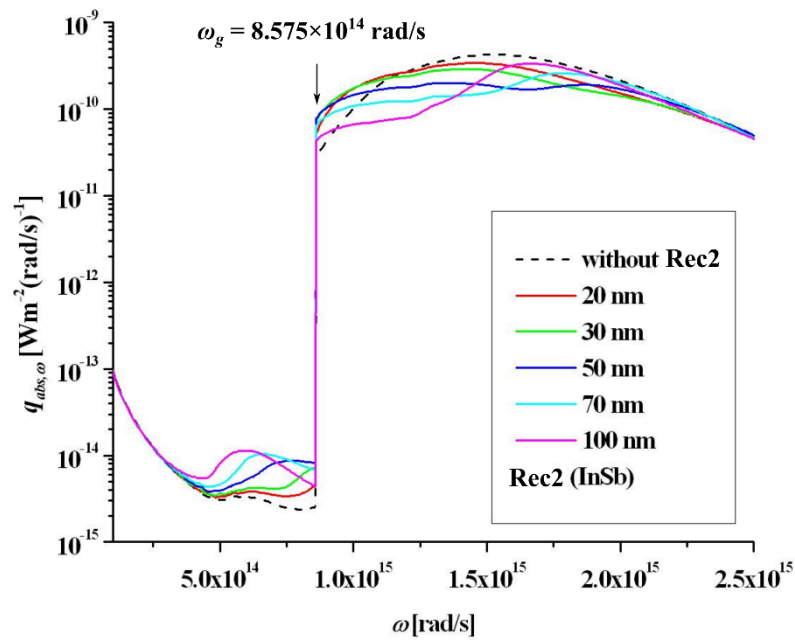


(b)

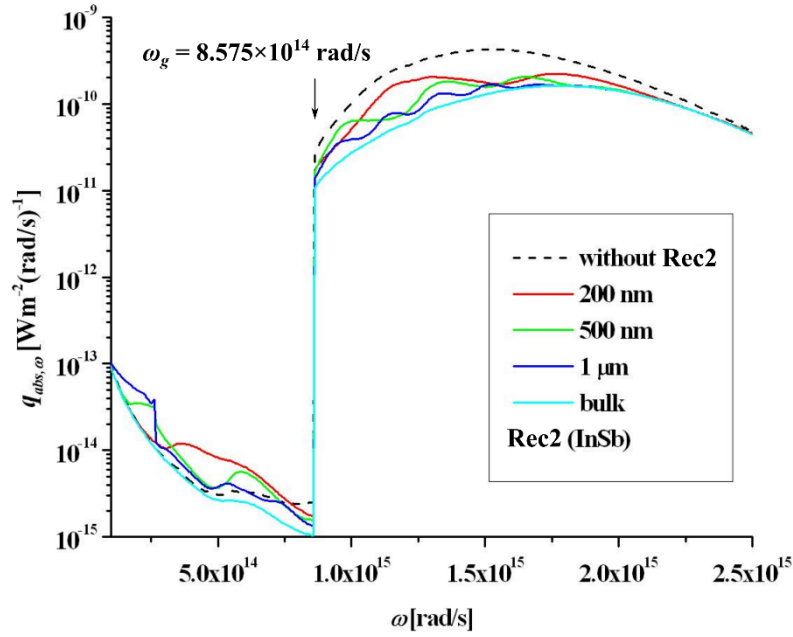
Fig. 8.3 Monochromatic radiative heat flux absorbed by Rec1 for d_{gap2} thicknesses of (a) 20 to 100 nm and (b) 100 nm to 10 μm . $d_{gap1} = t_{Rec1} = t_{Rec2} = 50$ nm.

Next, we analyse how changing the thickness of Rec2 affects the spectral absorption profile of Rec1. The sizes of d_{gap1} , Rec1 and d_{gap2} are maintained at 50 nm. Based on Fig. 8.4, at a Rec2 thickness of 20 nm, the heat flux peak decreases in magnitude as compared to the case without

Rec2. However, it is interesting to note that the absorbed heat flux values in the vicinity of the band-gap frequency are higher. As the thickness of Rec2 is increased further, one can observe that there is a wave-like trend propagating towards the left. The values in the area just below the band gap increase forming a ridge whose peak value shifts to lower frequencies as Rec2 gets thicker. In the area above the band gap however, we see decreasing values while a peak forms further up the spectrum. At a thickness of 100 nm, a peak—which is much narrower than the case without Rec2—can clearly be seen at 1.662×10^{15} rad/s. As the increase in the thickness of Rec2 extends beyond 100 nm, the “propagation” continues to the left and fluctuations start to occur until the bulk value is reached. When Rec2 is a bulk, the absorption spectrum of Rec1 is significantly lower than the case without Rec2 especially at frequencies above the band gap.



(a)



(b)

Fig. 8.4 Monochromatic radiative heat flux absorbed by Rec1 for Rec2 thicknesses of (a) 20 to 100 nm and (b) 200 nm to bulk. $d_{gap 1} = t_{Rec1} = d_{gap 2} = 50$ nm.

When Rec2 is modelled as Au, the profile differences between the different Rec2 thicknesses are negligible as shown in Fig. 8.5. However, the presence of the Au film does alter the absorption spectrum by increasing and narrowing the peak while reducing the values in the area just below the band-gap frequency. It is interesting to note that this observation greatly differs from the results obtained using an InSb Rec2. To understand this development, we calculate the SPP resonant frequency at a vacuum-gold interface using Eq. (6.1), yielding a frequency value of 9.694×10^{15} rad/s, which is way beyond our spectral range of interest. Thus it is extremely unlikely that SPP coupling would affect the radiative heat exchange. The change in the absorption profile in the presence of an Au film is most probably caused by interference effects due to reflection of waves off the top surface of Rec2. The InSb film on the other hand should support SPhPs in the same spectral regions as $In_{0.18}Ga_{0.82}Sb$ though not necessarily having the same resonant frequency. This would allow coupling of surface waves to occur, altering the absorption spectrum of Rec1 in conjunction with interference effects.

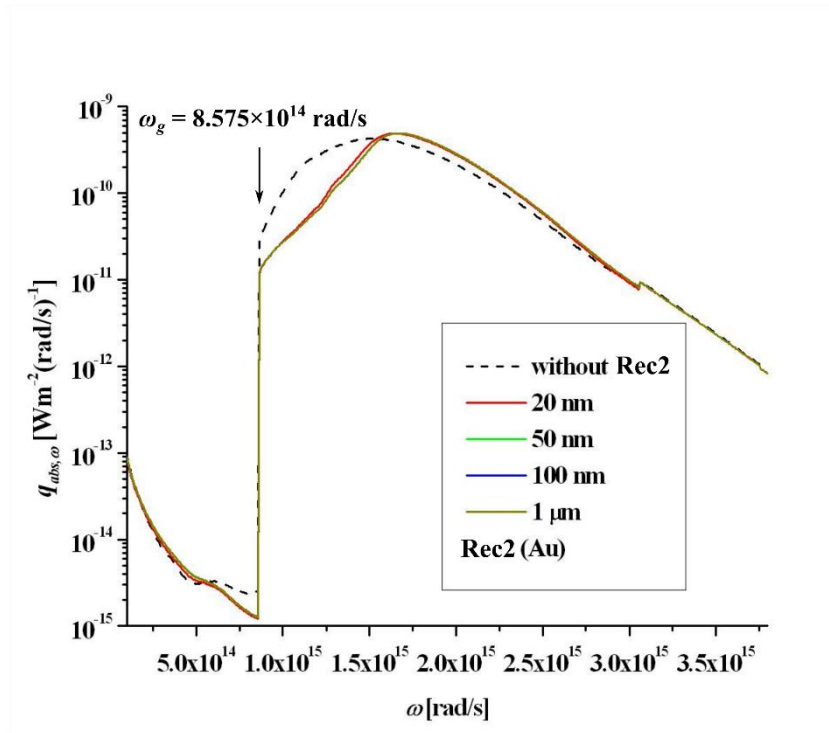


Fig. 8.5 Monochromatic radiative heat flux absorbed by Rec1 for different Rec2 (Au) thicknesses.

8.3 Concluding Remarks

It is clear based on the results presented thus far that when Rec1 is thin enough, the presence of a third body in close proximity alters the absorption spectrum of Rec1. The changes are caused by interference effects [119] or the coupling of surface waves [26]. The ability to alter the radiative heat flux spectrum may prove useful in applications like near-field TPV power generation where a third body could be used to tune the heat flux spectrum to increase efficiency while also acting as a cooling mechanism or a second TPV cell.

Chapter 9 Conclusions and Future Work

In this chapter, a summary of the main results presented in this thesis is given and recommendations for future studies are suggested.

9.1 Summary and Remarks

A one-dimensional opto-electro-thermal model of a nano-gap TPV system based on the work in [34] is presented in Chapter 4. A general analytical expression for the radiative heat flux at the surface of the receiver is also detailed. As part of the thermal portion of the model, an ensemble phonon Monte Carlo algorithm based on [85,86] is presented to simulate the heat transport in thin films. A new localized phonon destruction scheme is introduced to the MC simulation to simulate the effect of convective cooling. This multi-physics model through the use of numerical simulation allows us to predict the responses and performance of nano-gap TPV devices defined by a large set of user-defined parameters which include the system configuration, media temperatures, materials, doping concentrations, cooling parameters and so on.

In Chapter 5, we studied how four critical parameters (i.e. radiator material, cell material, cell thickness and doping concentration) affected the responses and performance of nano-gap TPV devices. In studying the effect of radiator material, four different materials: GaAs, W, SiC and Au were paired with a GaAs TPV cell. It was discovered that the most desirable radiator material would be one that possesses a high GE value and also supports surface polaritons of the same kind and spectrum as the TPV cell material (receiver). Next, three TPV cell materials: InGaSb, GaAs and Si were applied to a nano-gap TPV device utilising a W radiator. The effect cell material has on the near-field radiative transfer, photocurrent generated and the IQE was discussed. The cell material which had the highest absorption coefficient experienced the greatest radiative heat transfer. The photocurrent profile of each material was very much influenced by the material's IQE which is mostly determined by its electrical properties and to a certain extent, its thickness. It was discovered that a high-performance cell should exhibit low surface recombination velocities, and high minority carrier diffusion coefficient and lifetime values. The influence of cell thickness was studied by varying the thicknesses of the n and p -type regions. The thickness of the TPV cell affects the spatial absorption profile within

the cell. An absorption profile that facilitates the collection of EHPs would lead to greater IQE values. Next, insulated films of GaAs of differing thicknesses (1 μm , 3 μm and 5 μm), subjected to heat generation were simulated and it was discovered that the rise in temperature for all thicknesses was relatively uniform across the film leading to the conclusion that if the film is sufficiently thin, the temperature rise within the cell can be represented by a single value.

The doping-dependence of a nano-gap TPV device was studied through the simulation of a p -on- n Si TPV cell. The acceptor concentration, N_a was varied from 10^{23} m^{-3} to 10^{25} m^{-3} while the donor concentration, N_d was varied from 10^{21} m^{-3} to 10^{24} m^{-3} . It was discovered that the highest conversion efficiency value is achieved when $N_a = 10^{23} \text{ m}^{-3}$ (lowest N_a simulated) and $N_d = 10^{22} \text{ m}^{-3}$ while the greatest output power is generated when $N_a = 10^{25} \text{ m}^{-3}$ (highest N_a simulated) and $N_d = 10^{23} \text{ m}^{-3}$. The optical response of the device depends very much on the doping concentration of the TPV cell. High doping levels would greatly increase free carrier absorption which causes greater radiative heat transfer between the radiator and the receiver especially at frequencies below the band gap. At high N_a (p -type layer) values, the optical response is less sensitive to the change in N_d (n -type layer). It was also discovered that the lowest donor concentration in the absorber region may not necessarily produce the best results despite the greater diffusion length. When the absorber thickness, t_{abs} is smaller than the effective diffusion length, $L_{eff,h}$, the positive effects of a decreasing D_h outweigh its negatives until N_d is increased beyond an optimum value. This explains why P_m is greatest when $N_d = 10^{23} \text{ m}^{-3}$. A decreasing diffusion coefficient is also partly the reason behind the increasing P_m as N_a is increased. Increasing the doping concentration also reduces the generation of dark current provided that the minority carrier lifetime is not too low.

In Chapter 6, an ITO-based radiator was proposed for nano-gap TPV applications. Two types of ITO processing techniques were discussed and it was shown how the different techniques produced ITO layers with significantly different SPP resonant frequencies, owing to the change in the real part of the dielectric function. It was also discovered that the spectral heat flux profile of an ITO-based radiator can change dramatically based on the type of substrate material used. It is demonstrated that a substrate material possessing a dielectric function with low ϵ'_r (large negative values) and ϵ''_r values (low absorption) contributes the least amount of heat flux and maximizes the contribution of the ITO layer at the resonant frequency producing a narrower spectral heat flux profile. If the goal is just to maximize heat flux values at all frequencies, a

substrate material with high dielectric function values should be chosen. Furthermore, the thickness of the film radiator adjacent to the ITO layer has a significant effect on the heat flux spectrum especially at smaller thicknesses. In regards to Ag and W, as thickness decreases below the bulk value, the heat transfer between the radiator and the TPV cell increases until a certain thickness below which overall heat transfer starts to decline. That optimal thickness varies depending on the material. For Ag, the optimal thickness is around 5 nm while it is around 20 nm for W. If the material is SiC, the heat transfer declines as its thickness decreases to the point where it behaves very much like vacuum. Furthermore, it was shown that by tuning ITO properties to better match the band gap of the TPV cell, greater output power and conversion efficiency values can be obtained. This chapter focused on the effects of ITO-based radiators on the nano-gap TPV system without including the thermal effects of the TPV cell where the cell temperature is assumed to be 300 K. A more accurate analysis would include the temperature increase in the cell which would subsequently affect its optical and electrical responses.

In Chapter 7, we studied a thin-film nano-gap TPV device by simulating its optical, electrical and thermal responses using coupled numerical simulations. We observed how the responses and subsequent performance of the nano-gap TPV device changed with the temperature of the Si cell where it was discovered that the increase in temperature allows for greater maximum output power at the cost of conversion efficiency. The greater temperature allowed for increased optical absorption which in turn produced more photocurrent. However, beyond a certain threshold temperature, all performance metrics suffered. Since Si is a large band-gap material, it would be interesting as future work to determine if smaller band gap cells exhibit the same temperature-dependent trends as Si. Two types of radiators were also compared, namely thin film and bulk W. It was shown that the thin-film W radiator increased radiative heat transfer across the entire spectrum. The improvements above the band-gap frequency are particularly useful. However, due to the broadband nature of the increase, efficiency suffered. Next, the effect of cell thickness was analysed. The thickness of the cell was varied from 0.5 μm to 1 μm and we discovered that the thicker thin-film TPV cells produced better performances. Despite greater cooling requirements for thicker thin films, it is predicted that the overall efficiency does not suffer much due to improvements in the maximum output power. As a possible future endeavour, a method for quantifying the cooling requirement can be developed to determine the system's overall efficiency. It was also discovered that the cell thickness affected the heat flux absorption profile across the cell. Interference effects caused

the occurrence of ridges in the profile whose position and width depended on the cell thickness. To build upon this finding, one could seek to optimize the TPV cell thickness and layout to produce the optimum spatial distribution of radiative heat flux in the cell that would produce the most short-circuit current. Furthermore, as the thickness decreased, the amount of heat flux absorbed by each control volume increased. However, thicker films still ended up absorbing more radiative heat flux due to them having greater volume. Lastly, we tested the consistency of two heat transport models: Fourier's law and the phonon MC simulation with convective cooling implemented. We found that the two methods produced relatively similar results when simulating a 5- μm Si film. Next, thin films of thicknesses 1 μm and 0.5 μm were simulated. It was shown that at normal heat generation and convective cooling conditions, the temperature gradient is almost non-existent.

In Chapter 8, we observed how the presence of a third body in close proximity to the receiver affected the radiative heat transfer between the radiator and the receiver. Specifically, we calculated the spectral radiative heat flux absorbed by the receiver and showed how the profile changes when dimensions such as the vacuum gap size and layer thicknesses are altered. By changing those dimensions, new peaks are formed in the absorption spectrum while at the same time reducing the values in other spectral regions. When the third body supports surface waves in the same spectral regions as the receiver, we observed significant changes in the absorption profile of the receiver as the thickness of the third body is increased. However, all these changes are only noticeable when the receiver thickness is thin enough. These observations may prove useful in applications such as near-field cooling in near-field TPV systems where a cooling plate is brought into close proximity to the TPV cell in order to cool it. The cooling plate could be used to tune the near-field radiative heat transfer in order to increase efficiency while fulfilling its job as a cooling mechanism. Future research efforts could focus on the optimal configuration or dimensions to produce the best performance in terms of power output and system efficiency.

The analyses done in this thesis use conversion efficiency and output power as separate metrics for measuring performance. It might be more meaningful to combine the two into a single metric since conversion efficiency alone does not provide a holistic view of how well the system performs. As another suggestion, being able to determine the overall system efficiency which includes the power to heat the radiator would also make it easier to gauge performance.

9.2 Further Recommendations

The nano-gap TPV model presented in this thesis is one-dimensional, thus it is only suitable for devices with lateral dimensions (x and y -axes) which are much bigger than the dimensions in the normal direction (z -axis). It would be useful to develop a three-dimensional (3D) model of a nano-gap TPV system that allows for the simulation of arbitrary geometries or surface features to gain more insight into this kind of nano-power generators. Edalatpour and Francoeur [135] have come up with a near-field radiative heat transfer model for 3D arbitrary geometries but have yet to extend it to near-field TPV systems.

Near-field cooling is an attractive avenue in this field. To extend upon that idea, a dual TPV cell design could be considered as a means of cooling the first TPV cell while generating more electrical power. This could be done by coupling a conventional near-field TPV device to a low band-gap cell, separated by a nanometric gap. In this scenario, the first TPV cell, once heated up, acts as a radiator, emitting heat towards the second TPV cell. The first TPV cell is cooled while extra electrical power is generated by the second TPV cell which itself is cooled through free convection.

The next challenge in the field of near-field TPV is to build a working nano-gap TPV system to test the feasibility of this technology and also to enable researchers to test the predictions made through theoretical analyses. Micron-gap TPV devices have been fabricated and tested [50]. The same could be done in the near future to achieve a nanometric vacuum gap in the tens of nanometres given that nanotechnology is ever-growing in today's world. However, issues like surface roughness and thermal expansion would definitely remain as the main problems that need to be addressed.

Appendix A

The dielectric function of gold, Au and silver, Ag are modelled using the Drude model [70]:

$$\varepsilon_r(\omega) = \varepsilon_\infty - \frac{\omega_p^2}{\omega(\omega + i\gamma)} \quad (\text{A.1})$$

Table A.1 Parameters used to model the dielectric function of Au and Ag.

Materials	ε_∞	ω_p [rad/s]	γ [s ⁻¹]
Au [70]	1.0	1.371×10^{16}	4.05×10^{13}
Ag [115]	1.0	1.3689×10^{16}	2.7347×10^{13}

Table A.2 Parameters used to model the dielectric function of alumina [116].

Resonant frequency, ω_0 (cm ⁻¹)	Oscillator strength, $\Delta\varepsilon$	Damping coefficient, γ (cm ⁻¹)
385	0.25	4.1
405	0.63	16.6
435	2.73	4.0
495	0.05	10.9
573	2.60	14.2
633	0.11	7.0
769	0.07	143.6

Table A.3 Parameters used to model the dielectric function of W04 [125].

Parameters	Values
ε_∞	6.81
Ω_p (cm ⁻¹)	20000
Γ (cm ⁻¹)	8880
ω_1 (cm ⁻¹)	3730
$\omega_{p,1}$ (cm ⁻¹)	7590
γ_1 (cm ⁻¹)	4690
ω_2 (cm ⁻¹)	7780
$\omega_{p,2}$ (cm ⁻¹)	16700

γ_2 (cm ⁻¹)	8360
ω_3 (cm ⁻¹)	15000
$\omega_{p,3}$ (cm ⁻¹)	42900
γ_3 (cm ⁻¹)	10800
ω_4 (cm ⁻¹)	663
$\omega_{p,4}$ (cm ⁻¹)	1480
γ_4 (cm ⁻¹)	199

References

1. Basu, S., Z. Zhang, and C. Fu 2009, 'Review of near - field thermal radiation and its application to energy conversion', *International Journal of Energy Research*, vol. 33, no. 13, pp. 1203-1232.
2. Basu, S. 2016, *Near-Field Radiative Heat Transfer across Nanometer Vacuum Gaps: Fundamentals and Applications*, William Andrew.
3. Novotny, L. 2007, 'The history of near-field optics', *Progress in optics*, vol. 50, p. 137.
4. Polder, D. and M. Van Hove 1971, 'Theory of radiative heat transfer between closely spaced bodies', *Physical Review B*, vol. 4, no. 10, p. 3303.
5. Furs, A. and L. Barkovsky 2006, 'A new type of surface polaritons at the interface of the magnetic gyrotropic media', *Journal of Physics A: Mathematical and Theoretical*, vol. 40, no. 2, p. 309.
6. Yang, Y.-H., et al. 2012, 'Magnetic surface polariton in a planar biaxial metamaterial with dual negative magnetic permeabilities', *Plasmonics*, vol. 7, no. 1, pp. 87-92.
7. Hadjicosti, K., et al. 2014, 'Surface polaritons born by inter-element coupling in magnetic metamaterials', in *Advanced Electromagnetic Materials in Microwaves and Optics (METAMATERIALS), 2014 8th International Congress on*, IEEE, pp. 133-135.
8. Kittel, A., et al. 2005, 'Near-field heat transfer in a scanning thermal microscope', *Physical review letters*, vol. 95, no. 22, p. 224301.
9. Wischnath, U.F., et al. 2008, 'The near-field scanning thermal microscope', *Review of scientific instruments*, vol. 79, no. 7, p. 073708.
10. Liu, Z.-W., Q.-H. Wei, and X. Zhang 2005, 'Surface plasmon interference nanolithography', *Nano Letters*, vol. 5, no. 5, pp. 957-961.
11. Wang, L., et al. 2006, 'Nanolithography using high transmission nanoscale bowtie apertures', *Nano letters*, vol. 6, no. 3, pp. 361-364.
12. Guha, B., et al. 2012, 'Near-field radiative cooling of nanostructures', *Nano letters*, vol. 12, no. 9, pp. 4546-4550.
13. Mattarolo, G. 2007, *Development and modelling of a thermophotovoltaic system*, vol. 8. Kassel University Press GmbH.
14. Broman, L. 1995, 'Thermophotovoltaics bibliography', *Progress in Photovoltaics: Research and Applications*, vol. 3, no. 1, pp. 65-74.
15. Coutts, T.J. 2001, 'An overview of thermophotovoltaic generation of electricity', *Solar energy materials and solar cells*, vol. 66, no. 1, pp. 443-452.
16. Whale, M.D. 1997, 'A fluctuational electrodynamic analysis of microscale radiative transfer and the design of microscale thermophotovoltaic devices', PhD thesis, Massachusetts Institute of Technology.
17. Whale, M. and E.G. Cravalho 2002, 'Modeling and performance of microscale thermophotovoltaic energy conversion devices', *Energy Conversion, IEEE Transactions on*, vol. 17, no. 1, pp. 130-142.
18. Cravalho, E.G., C.L. Tien, and R. Caren 1967, 'Effect of small spacings on radiative transfer between two dielectrics', *Journal of Heat Transfer*, vol. 89, no. 4, pp. 351-358.
19. Boehm, R. and C. Tien 1970, 'Small spacing analysis of radiative transfer between parallel metallic surfaces', *Journal of Heat Transfer*, vol. 92, no. 3, pp. 405-411.
20. Rytov, S., Y. Kravtsov, and V. Tatarskii 1987, *Principles of Statistical Radiophysics, 1987*, Springer-Verlag, New York.
21. Mulet, J.-P., et al. 2002, 'Enhanced radiative heat transfer at nanometric distances', *Microscale Thermophysical Engineering*, vol. 6, no. 3, pp. 209-222.

22. Narayanaswamy, A. and G. Chen 2005, 'Direct computation of thermal emission from nanostructures', *Annual review of heat transfer*, vol. 14, no. 14.
23. Lee, B., K. Park, and Z. Zhang 2007, 'Energy pathways in nanoscale thermal radiation', *Applied Physics Letters*, vol. 91, no. 15, pp. 153101-153101-3.
24. Lee, B. and Z. Zhang 2008, 'Lateral shifts in near-field thermal radiation with surface phonon polaritons', *Nanoscale and Microscale Thermophysical Engineering*, vol. 12, no. 3, pp. 238-250.
25. Francoeur, M. and M.P. Mengüç 2008, 'Role of fluctuational electrodynamics in near-field radiative heat transfer', *Journal of Quantitative Spectroscopy and Radiative Transfer*, vol. 109, no. 2, pp. 280-293.
26. Francoeur, M., M.P. Mengüç, and R. Vaillon 2009, 'Solution of near-field thermal radiation in one-dimensional layered media using dyadic Green's functions and the scattering matrix method', *Journal of Quantitative Spectroscopy and Radiative Transfer*, vol. 110, no. 18, pp. 2002-2018.
27. Auslender, M. and S. Hava 1996, 'Scattering-matrix propagation algorithm in full-vectorial optics of multilayer grating structures', *Optics letters*, vol. 21, no. 21, pp. 1765-1767.
28. Park, K. and Z. Zhang 2013, 'Fundamentals and applications of near-field radiative energy transfer', *Frontiers in Heat and Mass Transfer (FHMT)*, vol. 4, no. 1.
29. Wang, J.-S. and J. Peng 2016, 'A microscopic theory for ultra-near-field radiation', *arXiv preprint arXiv:1607.02840*.
30. Narayanaswamy, A. and G. Chen 2003, 'Surface modes for near field thermophotovoltaics', *Applied Physics Letters*, vol. 82, no. 20, pp. 3544-3546.
31. Laroche, M., R. Carminati, and J.-J. Greffet 2006, 'Near-field thermophotovoltaic energy conversion', *Journal of Applied Physics*, vol. 100, no. 6, p. 063704.
32. Rytov, S., Y.A. Kravtsov, and V. Tatarskii 1989, *Principles of Statistical Radiophysics*, vol. 3, Springer, Berlin.
33. Park, K., et al. 2008, 'Performance analysis of near-field thermophotovoltaic devices considering absorption distribution', *Journal of Quantitative Spectroscopy and Radiative Transfer*, vol. 109, no. 2, pp. 305-316.
34. Francoeur, M., R. Vaillon, and M.P. Mengüç 2011, 'Thermal impacts on the performance of nanoscale-gap thermophotovoltaic power generators', *Energy Conversion, IEEE Transactions on*, vol. 26, no. 2, pp. 686-698.
35. Domoto, G., R. Boehm, and C.L. Tien 1970, 'Experimental investigation of radiative transfer between metallic surfaces at cryogenic temperatures', *Journal of Heat Transfer*, vol. 92, no. 3, pp. 412-416.
36. Hargreaves, C. 1969, 'Anomalous radiative transfer between closely-spaced bodies', *Physics Letters A*, vol. 30, no. 9, pp. 491-492.
37. Hargreaves, C.M. 1973, *Radiative transfer between closely spaced bodies*, NV Philips' Gloeilampenfabrieken.
38. Xu, J.B., et al. 1994, 'Heat transfer between two metallic surfaces at small distances', *Journal of Applied Physics*, vol. 76, no. 11, pp. 7209-7216.
39. Hu, L., et al. 2008, 'Near-field thermal radiation between two closely spaced glass plates exceeding Planck's blackbody radiation law', *Applied Physics Letters*, vol. 92, no. 13, p. 133106.
40. Narayanaswamy, A., S. Shen, and G. Chen 2008, 'Near-field radiative heat transfer between a sphere and a substrate', *Physical Review B*, vol. 78, no. 11, p. 115303.
41. Ottens, R., et al. 2011, 'Near-field radiative heat transfer between macroscopic planar surfaces', *Physical Review Letters*, vol. 107, no. 1, p. 014301.

42. Kralik, T., et al. 2012, 'Strong near-field enhancement of radiative heat transfer between metallic surfaces', *Physical review letters*, vol. 109, no. 22, p. 224302.
43. Ijro, T. and N. Yamada 2015, 'Near-field radiative heat transfer between two parallel SiO₂ plates with and without microcavities', *Applied Physics Letters*, vol. 106, no. 2, p. 023103.
44. Ito, K., et al. 2015, 'Parallel-plate submicron gap formed by micromachined low-density pillars for near-field radiative heat transfer', *Applied Physics Letters*, vol. 106, no. 8, p. 083504.
45. Watjen, J.I., B. Zhao, and Z.M. Zhang 2016, 'Near-field radiative heat transfer between doped-Si parallel plates separated by a spacing down to 200 nm', *Applied Physics Letters*, vol. 109, no. 20, p. 203112.
46. St-Gelais, R., et al. 2016, 'Near-field radiative heat transfer between parallel structures in the deep subwavelength regime', *Nature nanotechnology*.
47. Song, B., et al. 2015, 'Enhancement of near-field radiative heat transfer using polar dielectric thin films', *Nature nanotechnology*, vol. 10, no. 3, pp. 253-258.
48. Kloppstech, K., et al. 2015, 'Giant near-field mediated heat flux at the nanometer scale', *arXiv preprint arXiv:1510.06311*.
49. Cui, L., et al. 2017, 'Study of radiative heat transfer in Ångström-and nanometre-sized gaps', *Nature Communications*, vol. 8.
50. DiMatteo, R., et al. 2004, 'Micron - gap Thermophotovoltaics (MTPV)', in *AIP Conference Proceedings*, AIP, pp. 42-51.
51. Hanamura, K. and K. Mori 2007, 'Nano - gap tpv generation of electricity through evanescent wave in near - field above emitter surface', in *AIP Conference Proceedings*, AIP, pp. 291-296.
52. Chang, J.-Y., Y. Yang, and L. Wang 2015, 'Extraordinary Photon Transport by Near-Field Coupling of a Nanostructured Metamaterial with a Graphene-Covered Plate', *arXiv preprint arXiv:1509.05399*.
53. Fernández-Hurtado, V., et al. 2017, 'Enhancing Near-Field Radiative Heat Transfer with Si-based Metasurfaces', *arXiv preprint arXiv:1701.02986*.
54. Chang, J.-Y., Y. Yang, and L. Wang 2015, 'Tungsten nanowire based hyperbolic metamaterial emitters for near-field thermophotovoltaic applications', *International Journal of Heat and Mass Transfer*, vol. 87, pp. 237-247.
55. Jin, S., et al. 2016, 'Hyperbolic metamaterial-based near-field thermophotovoltaic system for hundreds of nanometer vacuum gap', *Optics express*, vol. 24, no. 6, pp. A635-A649.
56. Yang, Y., et al. 2017, 'Performance Analysis of a Near-Field Thermophotovoltaic Device with a Metallodielectric Selective Emitter and Electrical Contacts for the Photovoltaic Cell', *Journal of Heat Transfer*, vol. 139, no. 5, p. 052701.
57. Narayanaswamy, A. and G. Chen 2004, 'Thermal emission control with one-dimensional metallodielectric photonic crystals', *Physical Review B*, vol. 70, no. 12, p. 125101.
58. Chen, G. 2005, *Nanoscale energy transport and conversion: a parallel treatment of electrons, molecules, phonons, and photons*, Oxford University Press.
59. Modest, M.F. 2013, *Radiative heat transfer*, Academic press.
60. Francoeur, M. 2010, 'Near-field radiative transfer: Thermal radiation, thermophotovoltaic power generation and optical characterization', PhD thesis, University of Kentucky.
61. Joulain, K., et al. 2005, 'Surface electromagnetic waves thermally excited: Radiative heat transfer, coherence properties and Casimir forces revisited in the near field', *Surface Science Reports*, vol. 57, no. 3, pp. 59-112.

62. Raether, H. 1988, *Surface plasmons on smooth surfaces*, Springer.
63. Maier, S.A. 2007, *Plasmonics: fundamentals and applications*, Springer Science & Business Media.
64. Zhang, Y. 2007, *Nano/microscale heat transfer*, McGraw-Hill, New York.
65. Yeh, P. 1988, *Optical waves in layered media*, vol. 95. Wiley New York.
66. Peterson, A.F., et al. 1998, *Computational methods for electromagnetics*, vol. 2. IEEE press New York.
67. Rytov, S., Y.A. Kravtsov, and V. Tatarskii 1983, *Principles of statistical radiophysics. 3. Elements of random fields*, Springer-Verlag Berlin Heidelberg, New York.
68. Tai, C.-T. 1994, *Dyadic Green functions in electromagnetic theory*, Institute of Electrical & Electronics Engineers (IEEE).
69. Tsang, L., et al. 2004, *Scattering of electromagnetic waves, numerical simulations*, vol. 25. John Wiley & Sons.
70. Mulet, J.-P. 2003, 'Modélisation du rayonnement thermique par une approche électromagnétique. Rôle des ondes de surface dans le transfert d'énergie aux courtes échelles et dans les forces de Casimir', PhD thesis, Université Paris Sud-Paris XI.
71. Eringen, A.C. 2002, *Nonlocal continuum field theories*, Springer Science & Business Media.
72. Luque, A. and S. Hegedus 2011, *Handbook of photovoltaic science and engineering*, John Wiley & Sons.
73. Goetzberger, A., J. Knobloch, and B. Voss 1998, *Crystalline silicon solar cells*, Wiley Online Library.
74. Shockley, W. and W. Read Jr 1952, 'Statistics of the recombinations of holes and electrons', *Physical review*, vol. 87, no. 5, p. 835.
75. Green, M.A. 1982, 'Solar cells: operating principles, technology, and system applications'.
76. Van Zeghbroeck, B. 2004, *Principles of semiconductor devices*, Colorado University.
77. Eades, W.D. and R.M. Swanson 1985, 'Calculation of surface generation and recombination velocities at the Si - SiO₂ interface', *Journal of applied Physics*, vol. 58, no. 11, pp. 4267-4276.
78. El Amrani, A., et al. 2015, 'Efficient passivation of solar cells by silicon nitride', *Vacuum*, vol. 120, pp. 95-99.
79. Boriskina, S.V., et al. 2015, 'Enhancement and Tunability of Near-Field Radiative Heat Transfer Mediated by Surface Plasmon Polaritons in Thin Plasmonic Films', in *Photonics*, Multidisciplinary Digital Publishing Institute, pp. 659-683.
80. Francoeur, M., M.P. Mengüç, and R. Vaillon 2010, 'Spectral tuning of near-field radiative heat flux between two thin silicon carbide films', *Journal of Physics D: Applied Physics*, vol. 43, no. 7, p. 075501.
81. Patankar, S. 1980, *Numerical heat transfer and fluid flow*, CRC Press.
82. Vaillon, R., et al. 2006, 'Modeling of coupled spectral radiation, thermal and carrier transport in a silicon photovoltaic cell', *International journal of heat and mass transfer*, vol. 49, no. 23, pp. 4454-4468.
83. Streetman, B.G. and S. Banerjee 2000, *Solid state electronic devices*, vol. 4. Prentice Hall New Jersey.
84. M.A. G. 1998, *Solar Cells*, Prentice-Hall, The University of New South Wales, Kensington.
85. Bong, V.N.-S. and B.T. Wong 2014, 'Solution of the boltzmann transport equation for phonon transport via the speed-up transient monte carlo method using reference temperature', *Numerical Heat Transfer, Part B: Fundamentals*, vol. 66, no. 3, pp. 281-306.

86. Wong, B.T., M. Francoeur, and M.P. Mengüç 2011, 'A Monte Carlo simulation for phonon transport within silicon structures at nanoscales with heat generation', *International Journal of Heat and Mass Transfer*, vol. 54, no. 9, pp. 1825-1838.
87. Basu, S. and Z. Zhang 2009, 'Maximum energy transfer in near-field thermal radiation at nanometer distances', *Journal of Applied Physics*, vol. 105, no. 9, p. 093535.
88. Lau, J.Z.-J., V.N.-S. Bong, and B.T. Wong 2016, 'Parametric investigation of nano-gap thermophotovoltaic energy conversion', *Journal of Quantitative Spectroscopy and Radiative Transfer*, vol. 171, pp. 39-49.
89. Palik, E.D. 1998, *Handbook of optical constants of solids*, vol. 3. Academic press.
90. Adachi, S. 1987, 'Model dielectric constants of GaP, GaAs, GaSb, InP, InAs, and InSb', *Physical review B*, vol. 35, no. 14, p. 7454.
91. Green, M.A. and M.J. Keevers 1995, 'Optical properties of intrinsic silicon at 300 K', *Progress in Photovoltaics: Research and Applications*, vol. 3, no. 3, pp. 189-192.
92. Leroy, C., et al. 1999, 'Charge transport in non-irradiated and irradiated silicon detectors', *Nuclear Instruments and Methods in Physics Research Section A: Accelerators, Spectrometers, Detectors and Associated Equipment*, vol. 434, no. 1, pp. 90-102.
93. Hull, R. 1999, *Properties of crystalline silicon*, IET.
94. Sotoodeh, M., A. Khalid, and A. Rezazadeh 2000, 'Empirical low-field mobility model for III-V compounds applicable in device simulation codes', *Journal of applied physics*, vol. 87, no. 6, pp. 2890-2900.
95. González-Cuevas, J.A., et al. 2006, 'Modeling of the temperature-dependent spectral response of In1- χ Ga χ Sb infrared photodetectors', *Optical Engineering*, vol. 45, no. 4, pp. 044001-044001-8.
96. Novotny, L. and B. Hecht 2012, *Principles of nano-optics*, Cambridge university press.
97. Wong, B.T., et al. 2013, 'Coupling of near-field thermal radiative heating and phonon Monte Carlo simulation: Assessment of temperature gradient in n-doped silicon thin film', *Journal of Quantitative Spectroscopy and Radiative Transfer*.
98. Legrand, R., et al. 2016, 'Direct measurement of coherent subterahertz acoustic phonons mean free path in GaAs', *Physical Review B*, vol. 93, no. 18, p. 184304.
99. Durán, J.C., G. Venier, and R. Weht 1991, 'Optimization of the junction depth and doping of solar cell emitters', *Solar cells*, vol. 31, no. 6, pp. 497-503.
100. Karazhanov, S.Z. 2000, 'Temperature and doping level dependence of solar cell performance including excitons', *Solar energy materials and solar cells*, vol. 63, no. 2, pp. 149-163.
101. Ouyang, Z., et al. 2011, 'Influence of the absorber doping for p-type polycrystalline silicon thin-film solar cells on glass prepared by electron beam evaporation and solid-phase crystallization', *Journal of Applied Physics*, vol. 109, no. 5, p. 054510.
102. Fu, C. and Z. Zhang 2006, 'Nanoscale radiation heat transfer for silicon at different doping levels', *International Journal of Heat and Mass Transfer*, vol. 49, no. 9, pp. 1703-1718.
103. Collins, R. and H. Fan 1954, 'Infrared lattice absorption bands in germanium, silicon, and diamond', *Physical Review*, vol. 93, no. 4, p. 674.
104. Kuźmicz, W. 1986, 'Ionization of impurities in silicon', *Solid-state Electronics*, vol. 29, no. 12, pp. 1223-1227.
105. Rhodes, C., et al. 2008, 'Dependence of plasmon polaritons on the thickness of indium tin oxide thin films', *Journal of Applied Physics*, vol. 103, no. 9, p. 093108.
106. West, P.R., et al. 2010, 'Searching for better plasmonic materials', *Laser & Photonics Reviews*, vol. 4, no. 6, pp. 795-808.

107. Solieman, A. and M.A. Aegerter 2006, 'Modeling of optical and electrical properties of In 2 O 3: Sn coatings made by various techniques', *Thin Solid Films*, vol. 502, no. 1, pp. 205-211.
108. Smith, G.B., et al. 2006, 'Tuning plasma frequency for improved solar control glazing using mesoporous nanostructures', in *Photonics Europe*, International Society for Optics and Photonics, pp. 61970T-61970T-9.
109. Ilic, O., et al. 2012, 'Overcoming the black body limit in plasmonic and graphene near-field thermophotovoltaic systems', *Optics express*, vol. 20, no. 103, pp. A366-A384.
110. Chang, J.-Y., S. Basu, and L. Wang 2015, 'Indium tin oxide nanowires as hyperbolic metamaterials for near-field radiative heat transfer', *Journal of Applied Physics*, vol. 117, no. 5, p. 054309.
111. Lau, J.Z.-J. and B.T. Wong 2017, 'Indium Tin Oxide-Based Selective Emitter for Nano-Gap Thermophotovoltaic Applications', *Journal of Nano Research*, vol. 49, pp. 127-148.
112. Bordo, V.G. and H.-G. Rubahn 2008, *Optics and spectroscopy at surfaces and interfaces*, John Wiley & Sons.
113. Francoeur, M., M.P. Mengüç, and R. Vaillon 2010, 'Local density of electromagnetic states within a nanometric gap formed between two thin films supporting surface phonon polaritons', *Journal of Applied Physics*, vol. 107, no. 3, p. 034313.
114. Biehs, S.-A., D. Reddig, and M. Holthaus 2007, 'Thermal radiation and near-field energy density of thin metallic films', *The European Physical Journal B-Condensed Matter and Complex Systems*, vol. 55, no. 3, pp. 237-251.
115. Ordal, M.A., et al. 1985, 'Optical properties of fourteen metals in the infrared and far infrared: Al, Co, Cu, Au, Fe, Pb, Mo, Ni, Pd, Pt, Ag, Ti, V, and W', *Applied optics*, vol. 24, no. 24, pp. 4493-4499.
116. Rajab, K.Z., et al. 2008, 'Broadband dielectric characterization of aluminum oxide (Al₂O₃)', *Journal of Microelectronics and Electronic Packaging*, vol. 5, no. 1, pp. 2-7.
117. Leng, X., A. Bollinger, and I. Božović 2016, 'Purely electronic mechanism of electrolyte gating of indium tin oxide thin films', *Scientific reports*, vol. 6.
118. Davazoglou, D., et al. 1995, 'Structure and optical properties of tungsten thin films deposited by pyrolysis of W (CO) 6 at various temperatures', *Journal of applied physics*, vol. 77, no. 11, pp. 6070-6072.
119. Blandre, E., et al. 2015, 'Spatial and spectral distributions of thermal radiation emitted by a semi-infinite body and absorbed by a flat film', *AIP Advances*, vol. 5, no. 5, p. 057106.
120. Mirmoosa, M., M. Omelyanovich, and C. Simovski 2016, 'Microgap thermophotovoltaic systems with low emission temperature and high electric output', *Journal of Optics*, vol. 18, no. 11, p. 115104.
121. Chen, K., P. Santhanam, and S. Fan 2015, 'Suppressing sub-bandgap phonon-polariton heat transfer in near-field thermophotovoltaic devices for waste heat recovery', *Applied Physics Letters*, vol. 107, no. 9, p. 091106.
122. Wong, B.T. and M.P. Mengüç 2010, 'A unified Monte Carlo treatment of the transport of electromagnetic energy, electrons, and phonons in absorbing and scattering media', *Journal of Quantitative Spectroscopy and Radiative Transfer*, vol. 111, no. 3, pp. 399-419.
123. Wong, B.T., et al. 2014, 'Coupling of near-field thermal radiative heating and phonon Monte Carlo simulation: Assessment of temperature gradient in n-doped silicon thin film', *Journal of Quantitative Spectroscopy and Radiative Transfer*, vol. 143, pp. 46-55.

124. Lau, J.Z.-J. and B.T. Wong 2017, 'Thermal energy conversion using near-field thermophotovoltaic device composed of a thin-film tungsten radiator and a thin-film silicon cell', *Journal of Applied Physics*, vol. 122, no. 8, p. 084302.
125. Watjen, J., et al. 2013, 'Spectral radiative properties of tungsten thin films in the infrared', *International Journal of Heat and Mass Transfer*, vol. 61, pp. 106-113.
126. Glassbrenner, C. and G.A. Slack 1964, 'Thermal conductivity of silicon and germanium from 3 K to the melting point', *Physical Review*, vol. 134, no. 4A, p. A1058.
127. Holland, M. 1963, 'Analysis of lattice thermal conductivity', *Physical Review*, vol. 132, no. 6, p. 2461.
128. Bohren, C.F. and D.R. Huffman 2008, *Absorption and scattering of light by small particles*, John Wiley & Sons.
129. Ashcroft, N. and N. Mermin 1976, *Solid State Physics*, Saunders College, Philadelphia.
130. Watjen, J.I. 2016, 'Study of radiative properties of thin films and near-field radiation for thermophotovoltaic applications', PhD thesis, Georgia Institute of Technology.
131. Incropera, F.P., et al. 2007, *Fundamentals of heat and mass transfer*, Wiley.
132. Petukhov, B., T. Irvine, and J. Hartnett 1970, 'Advances in heat transfer, Vol. 6', *Academic, New York*, vol. 6, pp. 503-504.
133. Teo, H., P. Lee, and M.N.A. Hawlader 2012, 'An active cooling system for photovoltaic modules', *Applied Energy*, vol. 90, no. 1, pp. 309-315.
134. Ju, Y. and K. Goodson 1999, 'Phonon scattering in silicon films with thickness of order 100 nm', *Applied Physics Letters*, vol. 74, no. 20, pp. 3005-3007.
135. Edalatpour, S. and M. Francoeur 2014, 'The Thermal Discrete Dipole Approximation (T-DDA) for near-field radiative heat transfer simulations in three-dimensional arbitrary geometries', *Journal of Quantitative Spectroscopy and Radiative Transfer*, vol. 133, pp. 364-373.

Vita

Personal Information

Name: Japheth Lau Zi Jun

Date of birth: 9 February 1989

Nationality: Malaysian

Education

B.Eng (Mechanical) - Swinburne University of Technology Sarawak Campus, 2008-2011

Awards

Best Graduate Mechanical Engineering Student Award, Cahya Mata Sarawak Bhd, 2012

Work Experience

- Management Trainee, Cahya Mata Sarawak Bhd, Malaysia, 2012-2013
- Mechanical Engineer (Internship), X-Fab Sarawak Sdn Bhd, Malaysia, 2010

Journal Publications

- Lau, J.Z.-J., V.N.-S. Bong, and B.T. Wong 2016, 'Parametric investigation of nano-gap thermophotovoltaic energy conversion', *Journal of Quantitative Spectroscopy and Radiative Transfer*, vol. 171, pp. 39-49.
- Lau, J.Z.-J. and B.T. Wong 2017, 'Indium Tin Oxide-Based Selective Emitter for Nano-Gap Thermophotovoltaic Applications', *Journal of Nano Research*, vol. 49, pp. 127-148.
- Lau, J.Z.-J. and B.T. Wong 2017, 'Thermal energy conversion using near-field thermophotovoltaic device composed of a thin-film tungsten radiator and a thin-film silicon cell', *Journal of Applied Physics*, vol. 122, no. 8, p. 084302.